

**An Improved Positron Emission Tomography (PET)  
Reconstruction of 2D Activity Distribution using Higher  
Order Scattered Data**

by

Hongwei Sun

A Thesis submitted to the Faculty of Graduate Studies of

The University of Manitoba

in partial fulfillment of the requirements for the degree of

MASTER OF SCIENCE

Department of Physics and Astronomy

University of Manitoba

Winnipeg, Manitoba, Canada

Copyright © 2016 by Hongwei Sun

## **Abstract**

Positron Emission Tomography (PET) images reconstructed without adequate scatter corrections introduce noise and degrade image contrast. In commercial imaging systems, misalignment between computed tomography (CT) and PET images can introduce biases in the activity distribution. Recently, several reconstruction algorithms have been proposed, which made direct use of single scattered photons in the activity reconstruction. However, the realistic dataset contains single and higher order scattered photons, and current scatter reconstruction methods do not distinguish them. In this study, a novel reconstruction algorithm that is capable of processing higher order scattered photons was developed. A restricted attenuation correction method was created to avoid overcorrecting for scattered photons. The simulation outcomes have shown that the proposed methods can, under ideal energy resolution, reconstruct images that are qualitatively and quantitatively better than those obtained using existing algorithms, and that the methods show promise for use under more realistic clinical conditions.

## Preface

The original idea of using scattered coincidences in PET imaging was simultaneously proposed by Dr. Pistorius's group at the University of Manitoba and a research group from Siemens Healthcare. Dr. Pistorius and Dr. Hongyan Sun first proposed a 2-dimensional non-time-of-flight algorithm that was capable of using single scattered data to reconstruct activity distributions. Mohammadreza Teimoorisichani further expanded it to a 3-dimensional non-time-of-flight algorithm. The investigation of concurrently reconstructing activity and attenuation maps was explored by Geng Zhang. Previous results presented by our group demonstrated the effectiveness of these methods and motivated me to extend the use of scattered coincidences, which led to the advent of this work.

First of all, I studied the feasibility of using the list-mode maximum likelihood expectation maximization (MLEM) approach to generate the activity map. Dr. Hongyan Sun first derived an MLEM formula for the activity distribution reconstruction based on the model of single scattered coincidences. This algorithm has limits when dealing with realistic datasets that contain higher order scattered coincidences. Therefore, I expanded this algorithm to a new version based on the model of dual-scattered coincidences, which was able to process all types of scattered events. To avoid overcorrecting for scattered coincidences, I then developed a restricted attenuation correction approach that integrates with the proposed reconstruction algorithm. Lastly, I simulated the PET system and designed analytical phantoms using Monte Carlo simulators to evaluate the performance of these proposed methods.

## **Acknowledgement**

Stepping into a new and fascinating field of science, and acquiring new knowledge and personal growth, is what I have humbly experienced in the past two years. Many people have helped me with my journey in Winnipeg, Canada, and I would like to take this opportunity to express my sincerest gratitude to all of them.

Firstly, I would like to express my greatest thanks to my mentor, Dr. Stephen Pistorius for his continuous support and mentorship. During our weekly meetings, his immense knowledge, and insightful advice never ceased to expand my vision of scientific research. He always enabled me to expand on my research and fostered my critical thinking abilities, all the while providing sufficient patience, efficient analysis, and supportive recommendations. Without his inspiration and guidance, this dissertation would not be possible. It has been a great pleasure working with him, and I sincerely appreciate him for providing me the opportunity to join his research lab.

I would also like to thank Dr. Andrew Goertzen for his mentorship and constructive feedback on my research during the monthly meetings, as well as Dr. Yang Wang for his time serving on my examining committee.

I am also grateful to the faculty and staff of the entire Division of Medical Physics for their generous assistance whenever it was needed. Special thanks goes out to Alana Dahlin, Susan Beshta, and Wanda Klassen for their help with my graduate and administrative responsibilities.

I would like to express my appreciation to all my fellow students in the program: Geng Zhang, Mohammadreza Teimoorisichani and Dr. Hongyan Sun, who helped me tremendously when I first joined the group. They provided me with relevant research materials and valuable suggestions. I am also extremely grateful to the precious friendship with Kaiming Guo, Parandoush Abbasian, Princess Anusionwu, Pawel Siciarz, Troy Teo, Azeez Omptayo, Suliman Barhoum, Jesse Bellec and Robert Bergen.

I would also like to extend special gratitude to my friend, Dr. Ivan Stevic for his selfless sharing and helpful suggestions. Additionally, I want to thank all my soccer teammates in HY, Monopoly Property, Wenbo and Jihua for their generous supports. My sincere thanks also go to my friends Xiaofei Wang and Xueting Zhang for their kind help, which made my life in Winnipeg much happier and easier.

Most importantly, I would like to take this opportunity to express my deepest thanks and love to my dearest parents, Chengquan Sun and Ke Li; as well as the rest of my family for caring and supporting me through my life. They showed me the true meaning of life and without their love, I could not have accomplished my dreams. Thank you!

Lastly, I gratefully acknowledge the sources of funding from CancerCare Manitoba Foundation and the University of Manitoba.

*TO MY BELOVED GRANDPA,  
MING-QUAN LI*

# Table of Contents

<b>ABSTRACT</b> .....	<b>I</b>
<b>PREFACE</b> .....	<b>II</b>
<b>ACKNOWLEDGEMENT</b> .....	<b>III</b>
<b>TABLE OF CONTENTS</b> .....	<b>VI</b>
<b>LIST OF TABLES</b> .....	<b>VIII</b>
<b>LIST OF FIGURES</b> .....	<b>IX</b>
<b>LIST OF SYMBOLS</b> .....	<b>XII</b>
<b>1. INTRODUCTION</b> .....	<b>1</b>
1.1 POSITRON EMISSION TOMOGRAPHY.....	1
<i>1.1.1 Positron Emission and Annihilation</i> .....	1
<i>1.1.2 Photon Interactions with Matter</i> .....	5
1.1.2.1 Photoelectric Effect .....	6
1.1.2.2 Compton (Incoherent) Scattering .....	7
1.1.2.3 Other Types of Interaction of Photons with Matter .....	13
1.1.2.4 Total Attenuation Coefficient.....	14
1.2 SIGNAL MEASUREMENT AND HARDWARE STRUCTURE OF PET .....	17
<i>1.2.1 Coincidence Detection</i> .....	17
<i>1.2.2 Types of Coincidence Events</i> .....	19
<i>1.2.3 PET Detectors</i> .....	21
<i>1.2.4 Scanner Geometry</i> .....	26
1.3 IMAGE RECONSTRUCTION TECHNIQUES OF PET.....	27
<i>1.3.1 Analytical Reconstruction Methods</i> .....	28
<i>1.3.2 Iterative Reconstruction Methods</i> .....	30
1.4 DATA CORRECTIONS IN PET .....	33
<i>1.4.1 Scatter Correction</i> .....	34
<i>1.4.2 Attenuation Correction</i> .....	36
1.5 MOTIVATION AND OBJECTIVES OF THE STUDY.....	39

<b>2. METHODOLOGY .....</b>	<b>40</b>
2.1 ACTIVITY DISTRIBUTION RECONSTRUCTION .....	42
2.1.1 <i>Reconstruction Theory using Dual-scattered Coincidences</i> .....	42
2.1.2 <i>Multiple Scattered Coincidences Reconstruction</i> .....	48
2.1.3 <i>Generalised Dual-scattered MLEM Reconstruction Algorithm</i> .....	54
2.2 RESTRICTED ATTENUATION CORRECTION .....	56
2.2.1 <i>The Ratio of the Restricted to the Total Klein-Nishina Cross-Section</i> .....	58
2.2.2 <i>Calculation of the Total Klein-Nishina Cross-Section</i> .....	59
2.2.3 <i>Model of Dual-Scattered Coincidences Trajectories</i> .....	61
2.3 SIMULATIONS USING THE GATE PLATFORM.....	67
2.3.1 <i>Data and PET System Simulations with GATE</i> .....	68
2.3.2 <i>Phantom Design in GATE</i> .....	68
2.4 STATISTICAL ANALYSIS FOR DIFFERENT RECONSTRUCTIONS .....	69
2.4.1 <i>Activity Distribution Reconstruction using Multiple Scattered Coincidences</i> .....	70
2.4.2 <i>Reconstruction of Activity Distribution without Attenuation Correction</i> .....	71
2.4.3 <i>Activity Distribution Reconstruction using Restricted Attenuation Correction</i> .....	72
2.4.4 <i>Reconstruction of Activity Distribution with Non-Ideal Energy Resolution</i> .....	72
<b>3. RESULT .....</b>	<b>74</b>
3.1 RECONSTRUCTION OF ACTIVITY USING ONLY MULTIPLE SCATTERED COINCIDENCES .....	74
3.2 IMAGES RECONSTRUCTED WITHOUT ATTENUATION CORRECTION .....	76
3.3 IMAGES RECONSTRUCTED WITH RESTRICTED ATTENUATION CORRECTION.....	80
3.3.1 <i>Estimation of Total Compton Cross-Section</i> .....	80
3.3.2 <i>Ratio of the Restricted Compton Cross-Section to the Total Compton Cross-Section</i>	81
3.3.3 <i>Calculation of Restricted Attenuation Correction</i> .....	82
3.4 IMAGES RECONSTRUCTED WITH NON-IDEAL ENERGY RESOLUTION .....	87
<b>4. DISCUSSION AND CONCLUSION.....</b>	<b>92</b>
<b>APPENDIX .....</b>	<b>97</b>
<b>REFERENCE .....</b>	<b>102</b>

## List of Tables

Table 1-1. The properties of several radionuclides used in PET imaging.....	3
Table 1-2. Comparison of the contributions of different interactions to the mass attenuation coefficients in water. ....	16
Table 1-3. The main properties for commonly used scintillation crystals in the PET system. ....	23
Table 2-1. The expression of each parameter in equation (2-29). ....	59
Table 2-2. The coefficients of the curve of the total Compton cross-sections per unit mass.....	61
Table 2-3. The expression of each symbol in equation (2-38). ....	66
Table 2-4. Applicable types of data of different algorithms. ....	71
Table 3-1. Statistical results for valid reconstruction rate of each algorithm. ....	76

## List of Figures

Figure 1-1. The state of positronium excites an annihilation event where an electron-positron pair emits a pair of gamma rays.....	4
Figure 1-2. The kinematics of a photoelectric event.....	6
Figure 1-3. The kinematics of a Compton scattering event.....	8
Figure 1-4. The detectors arranged in a ring configuration.....	18
Figure 1-5. Four types of coincidences in PET.....	20
Figure 1-6. The schematic diagram of a PMT in a PET scintillation detector.....	24
Figure 1-7. A typical configuration of a PET scintillation block detector.....	25
Figure 1-8. The ring geometry of a PET scanner.....	26
Figure 1-9. The schematic draw of how septa work.....	27
Figure 1-10. A projection in the PET field-of-view.....	29
Figure 1-11. The flow chart of a typical iterative process.....	31
Figure 1-12. A phantom image reconstructed without attenuation correction.....	37
Figure 1-13. A true coincidence is detected at detector A and B in which a LOR is determined.....	38
Figure 2-1. The diagram of a dual Compton scattering event in the patient.....	42
Figure 2-2. The TCAs sizes and shapes vs. the total scattering angles for the same detector pair.....	44
Figure 2-3. The schematic figures of confining the real annihilation position of a dual-scattered coincidence pair using TCAs.....	45

Figure 2-4. The trending graph of equation (2-14). .....	53
Figure 2-5. The smaller area using the outline of the imaging content. ....	56
Figure 2-6. The number of photons with different energies measured by detectors. ....	57
Figure 2-7. The curve fitting of the total Compton cross-section per unit mass. ....	60
Figure 2-8. The schematic drawing of calculating the trajectory that a dual-scattered coincidence pair travels through. ....	63
Figure 2-9. The flow chart of implementing the GDS-MLEM algorithm. ....	67
Figure 2-10. A simplified Deluxe Jaszczak water-filled phantom. ....	69
Figure 3-1. Activity reconstructions of the water-filled cylinder phantom using multiple scattered coincidences only. ....	75
Figure 3-2. Reconstructions of activity distributions using different algorithms without attenuation corrections and the outline of the phantom. ....	77
Figure 3-3. The CRC vs. RSD curves of each algorithm in hot and cold regions. ....	79
Figure 3-4. Total Compton cross-section prediction. ....	81
Figure 3-5. The ratio of the restricted cross-section to the total cross-section depended on the initial photon energy and restricted photon energy. ....	82
Figure 3-6. The ratio of the restricted attenuation correction to the traditional attenuation correction where the traditional attenuation correction was assumed to be 1. ....	83
Figure 3-7. Reconstructions of activity distributions using two algorithms with the constraints of phantom's outline. ....	84
Figure 3-8. The CRC vs. RSD curves of for hot and cold regions using LOR-MLEM and GDS-MLEM algorithms where proper attenuations corrections and phantom's outline were used. ....	86

Figure 3-9. Reconstructions of activity distributions using non-ideal energy resolutions.  
..... 88

Figure 3-10. The CRC-RSD curves for hot and cold regions using different algorithms  
with non-ideal energy resolutions..... 89

## List of Symbols

$E_\gamma$	Energy of the incident photon
$\vec{P}_\gamma$	Momentum of the incident photon
$E'_\gamma$	Energy of the scattered photon
$\vec{P}'_\gamma$	Momentum of the scattered photon
$E_b$	Binding energy of a shell electron
$K_e$	Energy of the electron after ejection
$T_\beta$	Energy of the electron after collision
$\vec{P}'_\beta$	Momentum of the electron after collision
$a\tau$	The cross-section of the photoelectric effect per atom
$Z$	Atom number
$h$	Planck's constant
$\nu$	Frequency of a photon
$c$	Speed of light in vacuum
$m_e$	The rest mass of an electron
$E_{min}$	The minimum energy of a photon after one Compton scattering event
$\frac{d_e\sigma_0}{d\Omega_\theta}$	Differential cross-section per electron for a photon scattered at angle $\theta$ per unit solid angle
$\frac{d_e\sigma^{KN}}{d(h\nu')}$	Differential cross-section of a photon with incident energy $E_\gamma = h\nu$ to be scattered into an energy interval between $h\nu'$ and $h\nu' + d(h\nu')$
$r_0$	Classical electron radius
$e\sigma^{KN}$	Total cross-section per electron
$a\sigma^{KN}$	Total cross-section per atom
$\mu$	Linear attenuation coefficient
$\rho$	Density of the material
$\mu/\rho$	Mass attenuation coefficient
$I_0$	Initial photon flux
$I(h)$	Photon flux at depth $h$ in matter
$N_A$	Avogadro's constant
$\lambda(x, y)$	Tracer activity distribution
$p(s, \theta)$	Projections of $\lambda(x, y)$ along the line determined by variable $s$ and $\theta$
$BP(x, y)$	Reconstructed activity distribution

$P(v, \theta)$	1-dimensional Fourier transform of $p(s, \theta)$ with respect to variable $s$
$F(\alpha, \beta)$	2-dimensional Fourier transform of $\lambda(x, y)$
$h(s)$	Filter of back-projection
$N$	Number of projections
$M$	Number of pixels
$p_j$	Measured value in $j^{th}$ projection element
$\lambda_i$	Activity in the $i^{th}$ pixel in the image
$A_{i,j}$	System matrix that describes the probability of a true coincidence annihilated at the $i^{th}$ pixel being detected by the $j^{th}$ detector pair
$\lambda_i^k$	Activity in the $i^{th}$ pixel updated at $k^{th}$ iteration
$\mathcal{F}_N(x)$	The sum of scattering angles after $N$ Compton scattering events
$\langle P_{AB}(\theta_1, \theta_2) \rangle$	The mean number of coincidences where the two photons individually undergo a Compton scattering event (scattering angle $\theta_1$ and $\theta_2$ , respectively) and are detected in $A$ and $B$
$\rho_e(x)$	Electron density at point $x$ in the object
$Att_{AB,IJ}$	Attenuation factor when the two photons individually undergo a Compton scattering event at point $I$ and $J$ , respectively, and are detected in $A$ and $B$
$f_i^k$	Activity distribution of pixel $i$ in the $k^{th}$ iteration with list-mode data
$E_t$	Restricted energy threshold
$R_{KN}$	The ratio of the restricted Compton cross-section to the total Compton cross-section
$\bar{L}$	The distance between the two detected positions of the scattered photons
$Att_{\alpha,m}$	Attenuation factor defined by variable $\alpha$ and $m$
$w$	Weighting function
$I(i, j)$	Image matrix in the reconstruction
$R(i, j)$	Ratio matrix in the reconstruction
$H$	The average activity value of the hot disk
$B$	The mean activity value in the annulus around the disk
$S$	Default value of the hot-to-background ratio
$C$	The average activity value of the cold disk
$CRC$	The contrast recovery coefficient
$RSD$	Relative standard deviation
$RS_E$	The energy resolution for photons with an energy $E$

# **1. Introduction**

## **1.1 Positron Emission Tomography**

Positron emission tomography (PET) is a nuclear medicine imaging technique that has the distinguishing feature of employing positron-emitting radionuclides for diagnostic purposes. It is designed to permit precise evaluation of perfusion and metabolism in various tissues and enables proper identification of the functional disturbances underlying the body. Unlike other medical imaging modalities, such as Computed Tomography (CT), Magnetic resonance imaging (MRI), and Ultrasound (US), which provide anatomical information, the ability to provide functional information makes PET scans unique, and fast growing. In the early 1970s, the design of a PET system consisting of two 2-dimensional detector arrays was reported. Development of the commercial tomography for clinical use first appeared in the late 1970s. Currently, PET and other imaging techniques such as MRI and CT are typically used together for the evaluation of treatment. A recent report shows that the use of PET in patient care alters patient management in 25%-40% of cases [1]. In the following sections, the basic physics of PET, system hardware structure, image reconstruction techniques, and data corrections will be discussed.

### **1.1.1 Positron Emission and Annihilation**

In 1928, Paul AM Dirac first proposed the concept of positrons by postulating a subatomic particle which was equivalent in mass to an electron but carried a positive charge. Carl Anderson verified this assumption in 1932 by observing positrons using cloud chambers. The use of positron emitters in medical imaging was first suggested by Wrenn [2] and

Sweet [3], and the first prototype PET scanner was built by Brownell and Sweet [4]. The methods of PET are based on the spontaneous positron emission by the ultra-short-lived radionuclides. These radionuclides are produced in a cyclotron and then used to label various compounds of biological interests such as glucose, ammonia, and water. The labeled compound is then introduced into the human body, typically by intravenous injection, and distributed in tissues in a way depending on its biochemical and pharmacokinetic properties. For example, fluorodeoxyglucose (FDG) labeled with  $^{18}\text{F}$  is a widely used radiopharmaceutical in PET imaging today. The development of PET as an imaging technique was sped up with the introduction of  $^{18}\text{F}$ -FDG PET scans by Phelps *et al.* at UCLA in 1977 [5, 6]. Once FDG is administered, abnormal tissues take up more FDG because they have a higher rate of glucose metabolism than normal cells, enabling cancerous cells to be detected in the PET image.

The positrons come from the process of positron decay. Essentially, the parent atom is proton-rich and may achieve stability by converting a proton into a positron ( ${}^0_1\beta^+$ ) and a neutron. This process results in the daughter nucleus has one atomic number less than the parent nucleus. Therefore, the general equation for positron decay from an atom can be denoted as:



where  $Q$  is the energy,  $A$  is the atomic mass,  $Z$  is the atomic number,  $X$  is the parent nucleus,  $Y$  is the daughter nucleus, and  $\nu$  is a neutrino.

In addition to  $^{18}\text{F}$ , a variety of atomic nuclei can also decay through the positron-emitting process. Examples of other commonly used positron emitters are listed in table 1-1, together with their energies and ranges in water.

Radionuclide	$E_{max}$ (MeV)	Maximum Positron Range in Water (mm)	Mean Positron Range in Water (mm)
$^{11}\text{C}$	0.96	4.1	1.1
$^{13}\text{N}$	1.20	5.1	1.5
$^{15}\text{O}$	1.74	7.3	2.5
$^{18}\text{F}$	0.63	2.4	0.6
$^{68}\text{Ga}$	1.90	8.2	2.9

Table 1-1. The properties of several radionuclides used in PET imaging [9].  $E_{max}$  is the maximum energy of the emitted positron. The maximum and mean positron ranges in water are also listed.

After emission from the nucleus, the positron, with initial energy, travels a certain distance in matter, losing its kinetic energy constantly by interacting with the surrounding matter. The range of positrons in a particular material is usually determined by empirical measurements, which take its energy and properties of the material into account. After the positron has lost its energy, it comes to rest and will eventually interact with a nearby electron. A non-nuclear, hydrogen-like element called a “positronium” is then formed by the combination of the positron and electron. The positronium is not stable with a mean

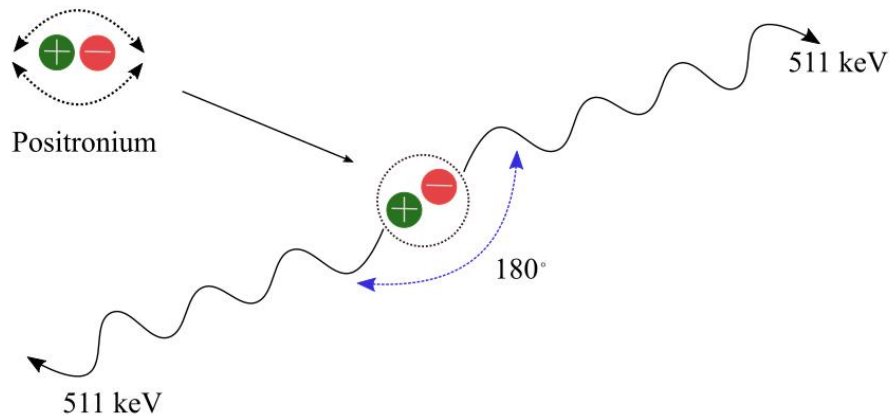


Figure 1-1. The state of positronium excites an annihilation event where an electron-positron pair emits a pair of gamma rays. Each of the photons has an energy of 511 keV. The two photons travel in an opposite direction.

life of around  $10^{-7}$  seconds. The electron-positron pair will then annihilate, producing two “back-to-back” 511 keV photons. In this annihilation process, the law of conservation of energy is obeyed, with the 1.022 MeV rest mass energy of the positron-electron pair being equally shared between the two generated photons. Additionally, the law of conservation of momentum requires the two photons to be emitted at 180 degrees to each other if the momentum of the positron and electron are zero when the annihilation occurs. Figure 1-1 illustrates the positron annihilation process. The simultaneous emission of two 511 keV photons in opposite directions ( $180^\circ$ ) is essential for PET imaging, as the current image reconstruction algorithms are created based on this unique emission.

However, in practice, the angle separating the emitted photons may not be exactly 180 degrees and in a small percentage of cases (<1% probability), three or even four photons can be emitted [7]. Since PET imaging aims to localize the position of the decaying nucleus, instead of where the positron ultimately annihilates, the short distance that the positron

travels will contribute to the uncertainty of that localization. The positron range is due to the non-zero kinetic energy of the positron after emission and increases with the initial energy of the positron. For a high energy positron emitter, such as  $^{68}\text{Ga}$ , the net energy released during positron decay is shared between the daughter nucleus, the positron, and the neutrino. Therefore, positrons are emitted with a range of energies, from zero up to a maximum energy ( $E_{max}$ ). The mean energy of the emitted positrons is approximately  $0.33E_{max}$  [8], and for  $^{68}\text{Ga}$  the maximum and mean positron range in water are 8.2 mm and 2.9 mm, respectively. Table 1.1 shows the ranges in water for some common positron emitters. Due to non-zero momentum while the positron and electron annihilate, many photon pairs (as high as 65% in water) are not emitted at 180 degrees with respect to each other. This non-collinear phenomenon contributes a 0.5-degree uncertainty in the localization of the nuclear decay event [9]. The non-collinear effect, together with the finite range of the positron are major factors in the lower limit of the spatial resolution of PET imaging.

### 1.1.2 Photon Interactions with Matter

In PET systems, some photons created by positron-electron annihilation may not reach the surrounding detectors. These photons can interact with the body tissue in different ways, depending on their energies. In this section, five different interactions with matter will be introduced. These are (i) photoelectric effect, (ii) Compton (incoherent) scattering, (iii) pair production, (vi) Rayleigh (coherent) scattering and (v) Photonuclear interaction. For PET scans where each photon has an initial energy of 511 keV, the first two processes dominate the interactions within the body. Thus, the emphasis in this section will be mainly on the photoelectric effect and Compton scattering. Details of other effects can be found in the

literature [9 10].

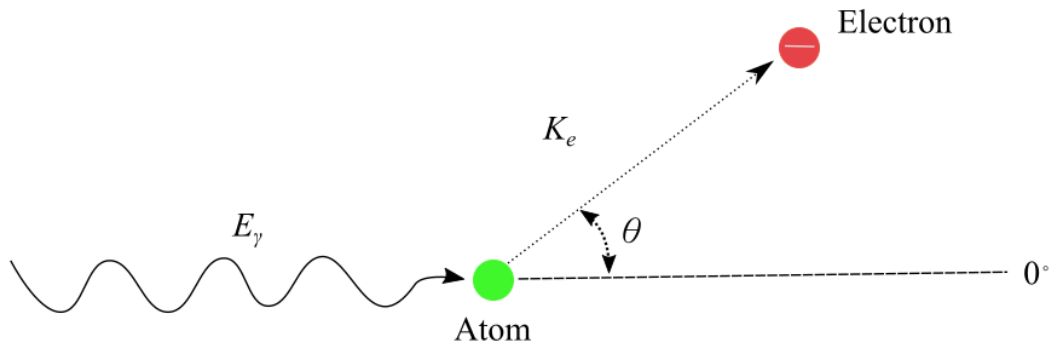


Figure 1-2. The kinematics of a photoelectric event. An incident photon with an energy  $E_\gamma$  from the left hits an atom. If the photon energy  $E_\gamma$  is greater than the binding energy  $E_b$  of a shell electron, the photon vanishes. The electron can be ejected with kinetic energy  $K_e$  and a scattering angle  $\theta$ .

### 1.1.2.1 Photoelectric Effect

In 1899, Philipp Lenard demonstrated that the light could cause a metal to emit electrons. The experiment showed that the electric current induced by the ejected electrons is proportional to the intensity of the light if the light intensity exceeds a certain threshold. This phenomenon is called the photoelectric effect. In practice, the photoelectric effect is the interaction between an incident photon and an orbital electron in an atom. Figure 1-2 shows the kinematics of the photoelectric effect. The incident photon must have an energy of  $E_\gamma = h\nu$  that is higher than that of the binding energy ( $E_b$ ) of the orbital electron. The photon loses all of its energy and ejects the electron. Part of its energy is used to overcome the binding energy of the electron while the rest of energy is transferred to the electron in

the form of kinetic energy ( $K_e$ ). Therefore, the kinetic energy of the electron after ejection is given by:

$$K_e = E_\gamma - E_b \quad (1-2)$$

In general, the photoelectric effect is of greatest importance at photon energies less than approximately 100 keV. The theoretical derivation of the interaction cross-section for the photoelectric effect is complicated due to the difficulties arising from the binding energy. However, the cross-section of the photoelectric effect per atom, integrated over all angles, can be empirically written as [10]:

$${}_a\tau \cong k \frac{(Z)^n}{(h\nu)^m} \quad (1-3)$$

where  $k$  is a constant,  $n \cong 4$  at  $h\nu = 0.1$  MeV and gradually increases to 4.6 at 3 MeV.  $m \cong 3$  at  $h\nu = 0.1$  MeV and slowly reduces to approximately 1 at 5 MeV. The photoelectric cross-section  $\tau$  decreases as the photon energy increases above 0.1 MeV.

#### 1.1.2.2 Compton (Incoherent) Scattering

Compton scattering or incoherent scattering is the interaction between a photon and a loosely bound orbital electron. The electron is so weakly bound to the atom that it is usually presumed to be free and at rest. This is not an unreasonable assumption because, in tissue, Compton scattering dominates at photon energies from about 100 keV to approximately 10 MeV. Therefore the binding energy of the electron to the atom is small (e.g., the binding energy of the electron to hydrogen is 13.60 eV) compared with the energy of the incoming photon in this range. Figure 1-3 describes the kinematics of Compton scattering. An incoming photon with the initial energy of  $E_\gamma$  and momentum of  $\vec{P}_\gamma$  strikes an unbound

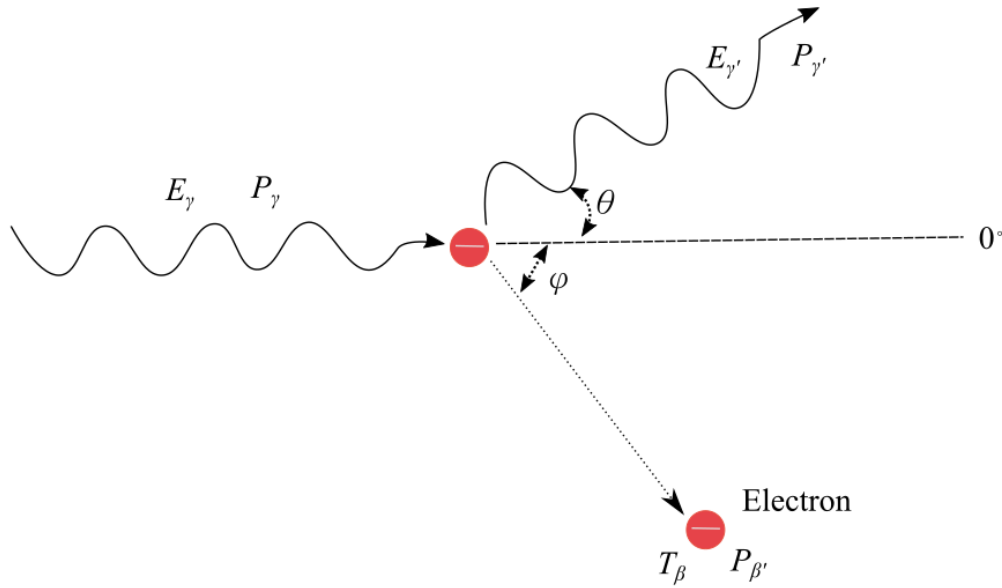


Figure 1-3. The kinematics of a Compton scattering event. An incident photon, with an initial energy  $E_\gamma$  and the momentum  $\vec{P}_\gamma$ , strikes an electron at rest. The photon is scattered at an angle

$\theta$  with a lower energy  $E'_\gamma$  and lower momentum  $\vec{P}'_\gamma$ .

stationary electron, scattering the electron at angle  $\varphi$  and transferring part of its energy to this electron.  $T_\beta$  and  $\vec{P}'_\beta$  describe the energy and momentum of the electron after collision, respectively. The photon is scattered at angle  $\theta$  (Compton scattering angle) with a lower energy  $E'_\gamma$  and the corresponding momentum  $\vec{P}'_\gamma$ .

**Compton equation.** Following the law of conservation of energy, the energy of the electron after collision is:

$$T_\beta = E_\gamma - E'_\gamma \quad (1-4)$$

Based on the law of the conservation of momentum along the original photon direction ( $0^\circ$ ) and the perpendicular to the direction of incidence ( $90^\circ$ ), it yields:

$$P_\gamma = P'_\gamma \cos \theta + P'_\beta \cos \varphi$$

$$P'_\gamma \sin \theta = P'_\beta \sin \varphi$$
(1-5)

Generally, the energy ( $E$ ) and momentum ( $P$ ) of a photon can be written as:

$$E = h\nu$$

$$P = |\vec{P}| = \frac{h\nu}{c}$$
(1-6)

where  $c$  is the speed of light in vacuum and  $h$  is Planck's constant.

By invoking the law of invariance, the relationship between the energy ( $T_\beta$ ) and the momentum ( $P'_\beta$ ) of the electron after collision can be described as:

$$P'_\beta c = \sqrt{T_\beta(T_\beta + 2m_e c^2)}$$
(1-7)

where  $m_e$  is the rest mass of an electron.

By combining the equation from (1-4) to (1-7), the correlation between  $E_\gamma$ ,  $E'_\gamma$  and  $\theta$  is given by:

$$\frac{E'_\gamma}{E_\gamma} = \frac{1}{1 + \frac{E_\gamma}{m_e c^2} (1 - \cos \theta)}$$
(1-8)

In PET imaging, each photon has an initial energy of 511 keV, which is equal to the rest energy of an electron (i.e.  $E_\gamma = m_e c^2$ ). Thus, equation (1-8) can be further simplified to:

$$\frac{E_{\gamma}'}{E_{\gamma}} = \frac{1}{2 - \cos \theta} \quad (1-9)$$

Equation (1-9) is of significance in this work because it gives a unique and concise correlation between the scattering angle and the energy of the scattered photon. This correlation enables the scattering angle to be determined using the detected photon energy, and also makes it possible to confine the annihilation position using scattered photons.

By using equation (1-9), the smallest energy for a photon undergoing a single scatter event can be obtained. When the scattering angle is equal to  $\pi$  ( $\cos \theta = -1$ ), the photon experiences a backscatter event and achieves the minimum remaining energy, which is 1/3 of the initial energy. i.e.

$$\frac{E_{min}}{E_{\gamma}} = \frac{1}{2 - (-1)} = \frac{1}{3} \quad (1-10)$$

Therefore, the minimum energy of a photon after one Compton scattering event is 170 keV.

***Klein-Nishina cross-section.*** In a single scatter event, the photon can be scattered at any angle from 0 to  $\pi$ . However, Compton scattering is not equally probable at all scatter angles. The earliest mathematical derivation of the probability of Compton scattering was proposed by J. J. Thomson [12]. It describes the differential cross-section per electron for a photon scattered at angle  $\theta$  per unit solid angle as:

$$\frac{d_e \sigma_0}{d\Omega_{\theta}} = \frac{r_0^2}{2} (1 + \cos^2 \theta) \quad (1-11)$$

where  $r_0 = e^2/m_e c^2$  is called the “classical electron radius”. By integrating equation (1-11) over all possible scattering angles (i.e.  $0 \leq \theta \leq \pi$ ), the total cross-section per electron

can be calculated (Note that the solid angle is given in terms of  $\theta$  by  $d\Omega_\theta = 2\pi \sin \theta d\theta$ ).

$$\begin{aligned} e\sigma_0 &= \int_{\theta=0}^{\theta=\pi} \frac{d_e\sigma_0}{d\Omega_\theta} d\Omega_\theta = \pi r_0^2 \int_{\theta=0}^{\theta=\pi} (1 + \cos^2 \theta) \sin \theta d\theta \\ &= \frac{8\pi r_0^2}{3} = 6.65 \times 10^{-25} \text{ cm}^2/\text{electron} \end{aligned} \quad (1-12)$$

This number represents the probability of Compton scattering when a photon passes through a material containing only one electron per  $\text{cm}^2$ , i.e. 665 scattering events in  $10^{27}$  photons. However, this model does not account for relativistic effects, which results in a higher evaluation of the probability when dealing with photons with energies above 10 keV. This issue was solved by Klein and Nishina [13, 14], when they applied Dirac's relativistic theory of the electron to the Compton scattering, obtaining an improved cross-section given by:

$$\frac{d_e\sigma^{KN}}{d\Omega_\theta} = \frac{r_0^2}{2} \left( \frac{E_\gamma'}{E_\gamma} \right)^2 \left[ \frac{E_\gamma}{E_\gamma'} + \frac{E_\gamma'}{E_\gamma} - \sin^2 \theta \right] \quad (1-13)$$

in which  $E_\gamma$  is the energy of the incident photon,  $E_\gamma'$  is the energy of the scattered photon (given by equation (1-8)), and  $\theta$  is defined as the scattering angle. It has been proved that the Thomson differential cross-section (equation (1-11)) is a special case of the Klein-Nishina equation (equation (1-13)) for low energy photons ( $E_\gamma \cong E_\gamma'$ ).

By replacing the scattering angle  $\theta$  with its energy-dependent form equation (1-8), the Klein-Nishina equation can be written in terms of the energy of the scattered photon. Therefore, the differential cross-section of a photon with incident energy  $E_\gamma = h\nu$  to be scattered into an energy interval between  $h\nu'$  and  $h\nu' + d(h\nu')$  is given by:

$$\frac{d_e \sigma^{KN}}{d(h\nu')} = \pi r_0^2 \frac{E_0}{(h\nu)^2} \left[ \frac{\nu}{\nu'} + \frac{\nu'}{\nu} + \left( \frac{E_0}{h} \right)^2 \left( \frac{1}{\nu'} - \frac{1}{\nu} \right)^2 - 2 \frac{E_0}{h} \left( \frac{1}{\nu'} - \frac{1}{\nu} \right) \right] \quad (1-14)$$

where  $E_0 = m_e c^2$ ,  $h$  is Plank's constant and  $\frac{1}{1+2\frac{h\nu}{E_0}} \leq \frac{\nu'}{\nu} \leq 1$ .

To obtain the total Klein-Nishina cross-section per electron ( ${}_e\sigma$ ), the calculation can be made by either integrating equation (1-13), over all solid angles or equation (1-14), over all energies. Here, equation (1-13) is used, which gives the result:

$$\begin{aligned} {}_e\sigma^{KN} &= 2\pi \int_{\theta=0}^{\theta=\pi} \frac{d_e \sigma}{d\Omega_\theta} \sin \theta d\theta \\ &= 2\pi r_0^2 \left\{ \frac{1+\alpha}{\alpha^2} \left[ \frac{2(1+\alpha)}{1+2\alpha} - \frac{\ln 1+2\alpha}{\alpha} \right] + \frac{\ln(1+2\alpha)}{2\alpha} - \frac{1+3\alpha}{(1+2\alpha)^2} \right\} \end{aligned} \quad (1-15)$$

where  $\alpha = h\nu/m_e c^2$ . This equation has been verified by various experiments, giving general agreement within experimental error (1.4%-8%) [10]. It is reasonable to state that the Klein-Nishina formula accurately describes the Compton scattering process if electrons of an atom are considered to be unbound and stationary. When the binding energy of electrons to the atom is comparable to the energy of the incident photon, an extra theory must be proposed to describe the possible intermediate states of the system.

It also needs to be mentioned that the total Klein-Nishina cross-section per electron is independent of the atomic number ( $Z$ ), thus the Klein-Nishina cross-section per atom of any material is given by:

$${}_a\sigma^{KN} = Z \cdot {}_e\sigma^{KN} \quad (1-16)$$

### 1.1.2.3 Other Types of Interaction of Photons with Matter

Pair production is another main mechanism for photons to interact with matter. It was first observed by Anderson using cloud chambers in the upper atmosphere. Unlike the photoelectric effect or Compton scattering, which mainly dominate at photons with low or intermediate energies, respectively; pair production is concerned with photons whose energies are relatively high. The Coulomb field is usually mandatory for pair production to take place near the atomic nucleus. In this interaction, the incident photon disappears, resulting in the rise of a positron and an electron. Thus, the energy threshold is obtained as twice the energy equivalent to the rest mass of an electron, i.e.  $2m_e c^2 = 1.022 \text{ MeV}$ . Above this energy limit of  $1.022 \text{ MeV}$ , the probability increases as the energy of the incident photon increases. The leftover energy, after the production of the positron-electron pair, is shared by the particles in the form of kinetic energy. In addition, pair production can also occur in the field of an atomic electron with lower probability. This type of event is typically referred to as “Triplet production”, as the incident photon divides its energy between the produced positron-electron pair and the host electron (recoil electron). In this case, the minimum energy threshold of the incident photon is  $4m_e c^2 = 2.044 \text{ MeV}$ , because the law of conservation of momentum must be preserved, even though the energy required to give rise to the positron-electron pair remains  $2m_e c^2$ . In a PET system, the majority of photons have an initial energy of 511 keV with only a small fraction of photons gaining excess energy from non-collinear annihilation. Therefore, pair production is rarely considered in PET imaging. The total cross-section of pair production per atom is roughly proportional to the atomic number squared ( $Z^2$ ). Further details regarding the cross-section can be found in [10, 15].

Rayleigh scattering, or as it is sometimes called, coherent scattering, is an elastic interaction between photons and atoms in which the incident photon is usually redirected through a small angle and essentially loses none of its energy. Specifically, the incident photon is absorbed by a tightly bound atomic electron, giving an electron with sufficient energy to rise to a higher-energy state. A second photon that has an identical energy to that of the incident photon is then emitted, with the electron reverting to its original state. The atom moves to conserve momentum in this process. The cross-section of Rayleigh scattering is difficult to describe analytically [16, 17, 18]. Rayleigh scattering has been shown to be of importance at low energies (below 1 MeV) and small scattering angles. However, the influence of Rayleigh scattering is small compared with Compton scattering (e.g. the ratio of the probability of Rayleigh scattering to the Compton scattering for 511 keV photons in water is about 0.22%). Hence, it too is typically ignored in PET imaging research.

Photonuclear interactions are another type of interaction for energetic photons whose energy exceed a few MeV. In this process, an incident photon enters and excites a nucleus, followed by the emission of a proton ( $\gamma, p$ ) or neutron ( $\gamma, n$ ). Due to the high probability of pair production in this energy range, the relative contribution of photonuclear interactions is less than 5%, and thus is commonly neglected in PET imaging.

#### **1.1.2.4 Total Attenuation Coefficient**

When a beam of photons passes through matter, it can be attenuated through a combination of the interactions mentioned previously. As the small influence from photonuclear interactions is typically ignored in most cases, the contributions to the total linear attenuation coefficient ( $\mu$ ) are primarily due to interactions of the photoelectric effect,

Compton scattering, pair production and Rayleigh scattering. It also should be noted that the contribution of Rayleigh scattering is usually only observed in a narrow beam geometry, since this kind of interaction deflects photons through relatively small angles. Therefore, the total linear attenuation coefficient ( $\mu$ ) is normally written as:

$$\mu = \mu_{\tau} + \mu_{\sigma} + \mu_{\kappa} \quad (1-17)$$

in which  $\mu_{\tau}$ ,  $\mu_{\sigma}$  and  $\mu_{\kappa}$  correspond to the linear attenuation coefficients of the photoelectric effect, Compton scattering, and pair production, respectively. These processes are independent of each other.

In general, the total mass attenuation coefficient ( $\mu/\rho$ ), in units of  $cm^2/g$ , is used to substitute the total linear attenuation coefficient when calculating the attenuation correction factor. It can be expressed as:

$$\frac{\mu}{\rho} = \frac{\mu_{\tau}}{\rho} + \frac{\mu_{\sigma}}{\rho} + \frac{\mu_{\kappa}}{\rho} \quad (1-18)$$

where  $\rho$  is the density of the material. For 511 keV photons in water, the total mass attenuation coefficient is  $9.598 \times 10^{-2} cm^2/g$ .

When a beam of photons travels through compounds or mixtures of elements, the Bragg rule should be applied to the total mass attenuation coefficient, which yields:

$$\left(\frac{\mu}{\rho}\right)_{mix} = \left(\frac{\mu}{\rho}\right)_A f_A + \left(\frac{\mu}{\rho}\right)_B f_B + \left(\frac{\mu}{\rho}\right)_C f_C + \dots \quad (1-19)$$

in which  $f_A$ ,  $f_B$ ,  $f_C$ ,  $\dots$ , are the weight fraction of each single element ( $A$ ,  $B$ ,  $C$ ,  $\dots$ ).

If a beam of photons, with initial flux  $I_0$ , enters a known matter (either a single material or mixtures of different elements), the photon flux at depth  $h$  can be written as:

$$I(h) = I_0 \exp\left(-\int_{x=0}^{x=h} \mu(x) dx\right) \quad (1-20)$$

where  $\mu(x)$  represents the linear attenuation coefficient at point  $x$ .

In PET imaging, water is commonly used to simulate the soft tissue within patients, since it has similar properties. Table 1-2 gives the total mass attenuation coefficient ( $\mu/\rho$ ) for photons (at energies of 511 keV) travelling through water, as well as the mass attenuation coefficient for each type of interaction, including the photoelectric effect ( $\mu_{PE}/\rho$ ), Compton scattering ( $\mu_{CS}/\rho$ ), pair production ( $\mu_{PP}/\rho$ ), and Rayleigh scattering ( $\mu_{RS}/\rho$ ). By comparison, it shows that Compton scattering is the most probable interaction and all other interactions can be ignored due to their negligible contributions to the total mass attenuation coefficient  $\mu/\rho$ . Similarly, regarding other organs and tissues, Compton scattering dominates the interaction in the human body. Therefore, the total mass attenuation coefficient in an imaged object can be approximated by:

	$\mu_{PE}/\rho$ ( $cm^2/g$ )	$\mu_{CS}/\rho$ ( $cm^2/g$ )	$\mu_{PP}/\rho$ ( $cm^2/g$ )	$\mu_{RS}/\rho$ ( $cm^2/g$ )	$\mu/\rho$ ( $cm^2/g$ )
<b>Water</b>	0.0000179	0.0958	0	0.000216	0.0961

Table 1-2. Comparison of the contributions of different interactions to the mass attenuation coefficients in water. The Compton scattering effect, by contrast, contributes 3-4 orders of magnitude larger than other types of interactions.

In practice,  $\mu_{CS}/\rho$  can be substituted by the total Klein-Nishina cross-section per unit mass ( $\sigma_C^{KN}/\rho$ ). Hence, the total mass coefficient in PET imaging can be generally simplified to:

$$\frac{\mu}{\rho} = \frac{\mu_{CS}}{\rho} = \frac{\sigma_C^{KN}}{\rho} = \frac{N_A Z}{A} {}_e\sigma^{KN} \quad (1-22)$$

in which  $N_A = 6.022 \times 10^{23} \text{ mole}^{-1}$  is also known as Avogadro's constant,  $Z$  is the number of electrons per atom and  $A$  indicates the number of grams per mole of the material. The expression of  ${}_e\sigma^{KN}$  is given by equation (1-15).

## 1.2 Signal Measurement and Hardware Structure of PET

The processes of positron decay and positron-electron annihilation have been discussed in the last section, followed by the introduction of different interactions between the photons and materials. The reconstruction of PET images relies on the information from photons and the read-out system. Therefore, the detection of photons and the basic geometry of the PET system will be discussed in this section.

### 1.2.1 Coincidence Detection

After a positron-electron annihilation event, two 511 keV photons are generated, which hit the detectors of a PET scanner in an opposite direction. The path that links the two detectors' positions is called the line-of-response (LOR). The detected photon pair is referred to as a coincidence if both of them are detected within a specific time interval which is usually known as the timing window (typically 6-12 nanoseconds). Note that the photon pair will not be counted if the first detected photon is not accompanied by the second photon within

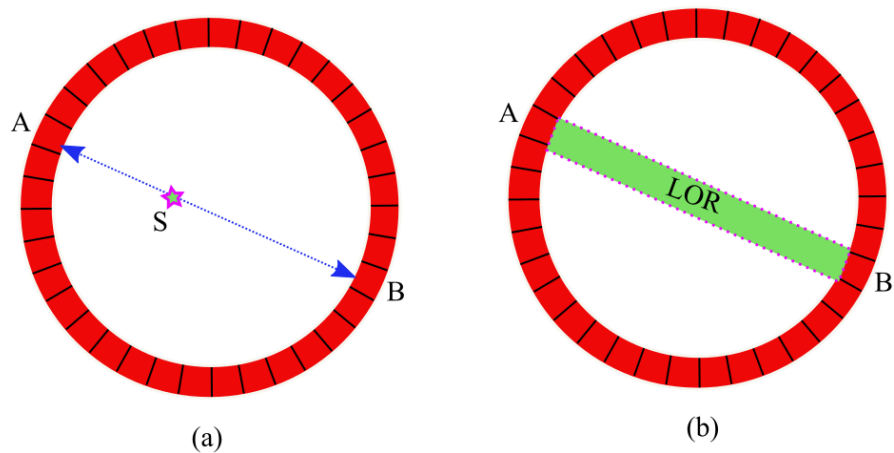


Figure 1-4. The detectors are arranged in a ring configuration. (a) A pair of photons is generated in an opposite direction from a positron-electron annihilation event at point S; (b) Two photons are detected by detectors A and B in a timing window where a LOR is assigned for this particular coincidence.

this timing window. PET imaging uses these coincidences to determine the point of annihilation within the body. Since the location of annihilation, as mentioned in section 1.1.1, is very close to the location of positron emission, it is, therefore, a reliable indicator as to where the positron emitter is in the body. Figure 1-4 shows how an LOR is determined in PET scans. A PET scanner containing a ring of detectors is presented on the left. The detectors are distributed in rotational symmetry to the center of the scanner. A positron-electron annihilation event occurs at point S, with two photons back-to-back emitted. The photons pair hit the detector A and B, respectively. If these two photons can be detected in a timing window, they will form a true coincidence. The LOR, connecting the detector A and detector B is shown in figure 1-4 (b).

### 1.2.2 Types of Coincidence Events

In reality, four different kinds of coincidence events exist in PET imaging. Traditionally, only true coincidences are considered to contribute to image reconstruction while other types of data are regarded as contaminations. However, the limitation of the detector's energy resolution and several interactions of the 511 keV gamma rays prevent the exclusion of three other types of coincidences. Figure 1-5 explicitly illustrates these four types of coincidences.

***True coincidence.*** A pair of unscattered photons from the same positron-electron annihilation is detected by two separate detectors within the timing window. This type of data is, for most traditional algorithms, the only reconstruction resource for radionuclide activity distribution.

***Scattered coincidence.*** After the emission by positron-electron annihilation, one or both of the photons interact with the object before being detected. Since Compton scattering dominates at 511 keV (see section 1.1.2.4), most of the scattering events are Compton scattering interactions. Therefore, this process changes the direction of the photon and consumes part of its energy. The information of the coincidence is lost because the line that connects the two detectors (green dotted line in the top-right picture of figure 1-5) no longer passes through the actual annihilation position. When the image is reconstructed using a traditional algorithm, the presence of scatter coincidences compromises the quantitative accuracy of the image. To overcome this, conventional reconstruction algorithms typically estimate a scatter contribution (sinogram) that is used to subtract the scatter coincidences from the projection data. More generally, scatter coincidences with lower energies can be

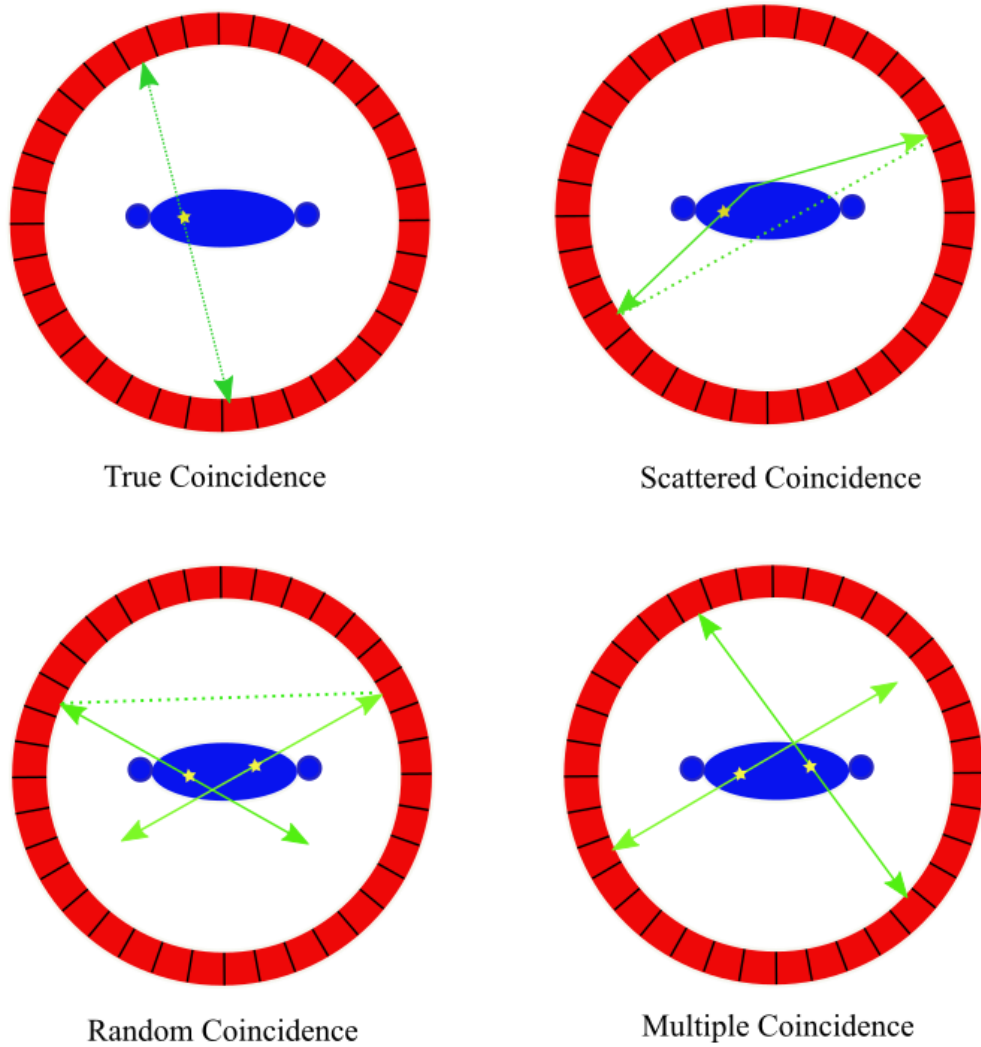


Figure 1-5. Four types of coincidences in PET: true coincidence, scattered coincidence, random coincidence and multiple coincidence.

partially excluded by employing an appropriate energy window (e.g. 350-650 keV).

**Random coincidence.** Two photons, originating from different positron annihilations, reach the detectors in the timing window and are thereby recorded. If not corrected for, the random coincidences affect the image reconstruction of PET by providing inaccurate contrast and compromising quantification, since the LOR defined by a random coincidence

cannot relate to the actual annihilation position (green dotted line in the bottom-left picture of figure 1-5). Several methods have been proposed to correct for the random coincidences, but the image noise will increase as the result of those techniques. Unlike true coincidence rates which increase with the increase of administered activity, the random coincidence rate is proportional to the square of the activity. Therefore, the appropriate selection of injected activity is essential for improving the image quality.

**Multiple coincidences.** Three or even more photons are detected within a single timing window. Some readers accept them and assume that the random coincidences corrections will also deal with the multiple coincidences. In general, this type of coincidence is discarded in traditional PET systems.

### 1.2.3 PET Detectors

**Detector basis:** PET imaging is based on the detection of 511 keV photons, so it requires the detector to be relatively sensitive to the photons in this energy range. The selected detectors need to accurately measure the energy of each photon and to have a fast response to allow each coincidence to be detected within the timing window. In general, gas chambers, semiconductor detectors, and scintillation detectors are three main categories of radiation detectors. However, the scintillation detectors are of most interest for modern clinical PET systems, since they have higher stopping efficiency and good energy resolution for 511 keV photons, compared with the other two types of detectors.

**Scintillation process and crystals.** When 511 keV gamma rays hit the scintillation detectors, they undergo the same kind of interaction inside the detectors as they do in the human body. However, the probabilities of these interactions may differ as a result of the

different atomic number of the material. The Photoelectric effect and Compton scattering are two major interactions. Rayleigh scattering and pair production are still negligible, even if in principle they will occur more frequently in the detector. During the interaction the photons transfer part of the photon's energy to the electrons in the scintillation crystal, allowing the electrons in the ground state (valence band) to jump to a higher state (conduction band). However, excited electrons are not stable in the conduction band, and they will go down to the ground state again, with the emission of scintillation photons. Normally the energy gap ( $E_g$ ) between the valence and conduction band is in the ultraviolet range so adequate impurities are added into pure scintillation crystals, which are capable of adjusting  $E_g$  between these two bands and eventually results in the emission of visible lights. When choosing a specific scintillation crystal for use, four main properties of a scintillator are most of concern. They are:

- (i) The stopping efficiency for 511 keV photons: The photon travels a certain distance before it deposits its entire energy into the crystal. This distance is known as the attenuation length and is also used to represent the stopping efficiency. Generally, the shorter the attenuation length, the greater the stopping efficiency.
- (ii) Decay constant: Modern PET system favors scintillators with short decay time since they can process individual events faster.
- (iii) Light output: High light output is desirable because it helps to achieve good spatial and energy resolution.
- (iv) Energy resolution: It is determined by both scintillator light output and the intrinsic energy resolution of the scintillator.

Commonly used scintillator materials in current PET scanners are: (1) sodium iodide (NaI), (2) bismuth germinate (BGO), (3) lutetium oxyorthosilicate (LSO), (4) yttrium oxyorthosilicate (YSO), (5) gadolinium oxyorthosilicate (GSO) and (6) barium fluoride (BaF<sub>2</sub>). Their properties are listed in table 1-3.

Radionuclide	NaI	BGO	LSO	YSO	GSO	BaF <sub>2</sub>
Attenuation Length (cm)	2.9	1.1	1.2	2.6	1.4	2.2
Decay Time (ns)	230	300	40	70	60	0.6
Light Output (photons/keV)	38	6	29	46	10	2
Intrinsic Energy Resolution $\Delta E/E$ (%)	5.8	3.1	9.1	7.5	4.6	4.3
Energy Resolution $\Delta E/E$ (%)	6.6	10.2	10	12.5	8.5	11.4

Table 1-3. Main properties for commonly used scintillation crystals in PET systems [9].

**Photo-detectors.** A photo-detector is required to read the information measured by PET detectors. It allows the conversion of the signal from scintillation light to electrical current and is usually divided into two categories: (1) photo-multiplier tubes (PMTs) and (2) semiconductor-based photodiodes.

The photo-multiplier tube is still the most common detector to measure the scintillation light. It consists of a sequence of dynodes and a thin photocathode layer at the entrance

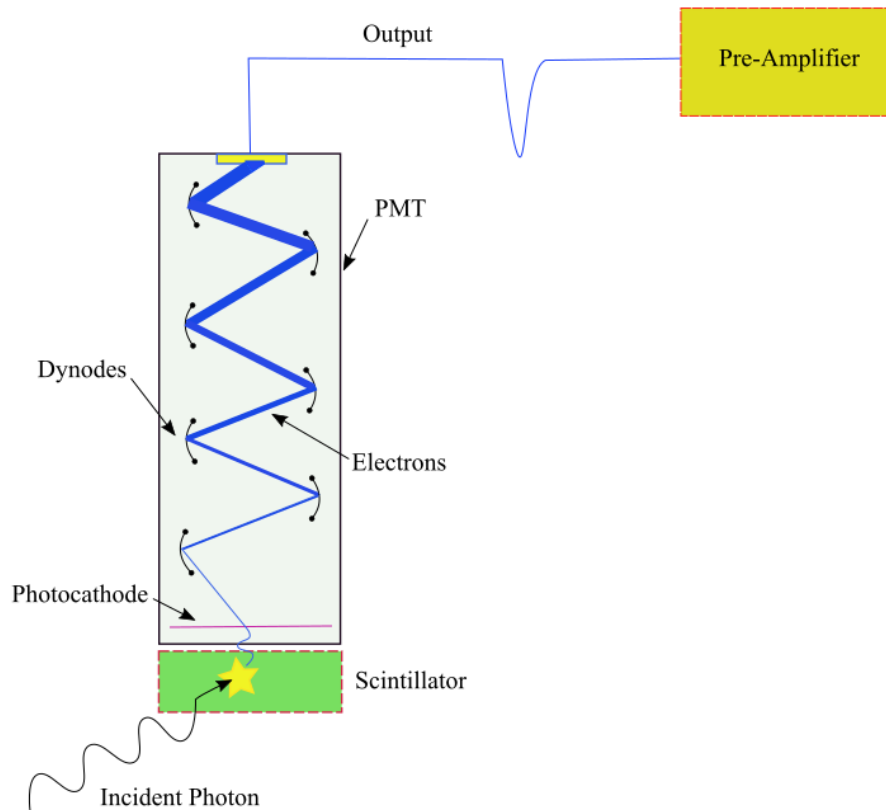


Figure 1-6. The schematic diagram of a PMT in a PET scintillation detector. The primary electrons are first emitted by the photocathode. The number of electrons then increases exponentially while interacting with several levels of dynodes. These electrons are then captured at the anode, where they are converted to an electrical signal for computational interpretation.

As shown in Figure 1-6, when a scintillation photon hits the photocathode, it deposits its energy and triggers the release of a photoelectron. The nearby dynode has a positive potential with respect to the photocathode. Due to the potential difference, the emitted electron can escape from the surface of the photocathode, and is further accelerated. This acceleration increases the energy of the electron, which results in the emission of multiple secondary electrons. The process of acceleration and

emission is then repeated on the next dynode structures each with an increased potential until a gain of more than a million electrons are achieved at the final anode, where the electrons are detected. This gain obtained from the PMT is the main reason for its use in scintillation detectors, since it gives an excellent signal-to-noise ratio (SNR) for low light levels. The disadvantage of a PMT is the low efficiency of the emission, resulting from the nature that a single scintillation photon can excite only one photoelectron escape from the cathode, and the limits of light collection efficiency.

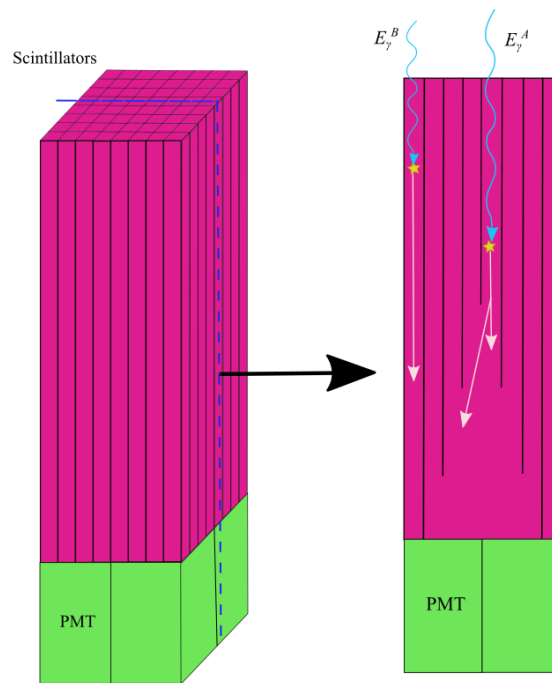


Figure 1-7. A typical configuration of a PET scintillation block detector. 64 scintillators are connected to 4 PMTs. The crystal detector is cut to various depths which allows four PMTs to address the localization. For example, photon A is detected in the central shallow cut detector and its localization is not determined by a single PMT, since the output light photons (while line) hit several PMTs. Photon B, by contrast, is detected at the edge of the detector where the output light can merely be recorded by one PMT.

Photodiodes, developed usually in the form of PIN diodes, are normally used for semiconductors. Here, PIN refers to the three zones of the diode: P-type, Intrinsic, and N-type. Compared with PMTs, photodiodes have drawbacks such as low SNR and are sensitive to small temperature change. In recent years, the Avalanche Photo Diode (APD) has been developed which partially overcomes these drawbacks.

**Block detectors:** The most common design of detectors in PET scanners is the so-called “block detector”. It consists of a rectangular parallelepiped of scintillator material, sectioned by partial saw cuts into discrete detector elements. Four PMTs are usually attached to the back of the scintillator block, e.g. 8×8 crystal detectors coupled with 4 PMTs is shown in Figure 1-7.

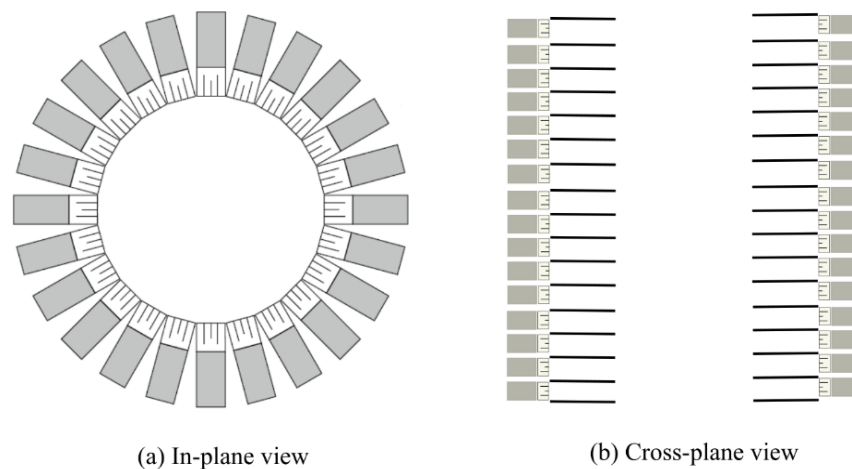


Figure 1-8. The ring geometry of a PET scanner. (a) is the in-plane view of a PET scanner while (b) is a cross-plane view. The crystal rings are separated by septa, shown as heavy black lines on the right one.

### 1.2.4 Scanner Geometry

**Scanner geometry.** Many PET scanners are constructed using a ring or several rings of

block detectors. In each ring, pairs of highly sensitive detectors are housed together, working for the detection of coincidences. Figure 1-8 shows the schematic drawing of a ring geometry, from both in-plane and cross-plane views.

**Septa.** Septa are placed between the rings of detectors. In general, the septa are made of a high-Z material such as tungsten, which can block the photons that do not travel in the plane of the detectors. The employment of septa can switch the PET scanners between 2-dimensional and 3-dimensional mode. Figure 1-9 is the illustration of how they work.

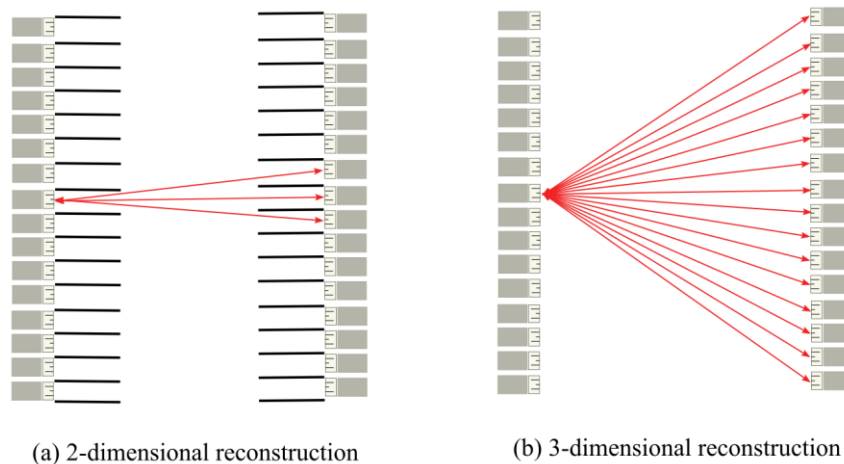


Figure 1-9. The schematic draw of how septa work. (a) 2D reconstruction scenario due to the block effect of septa. (b) Photons can travel in plane which allows 3D PET reconstruction.

### 1.3 Image Reconstruction Techniques of PET

In general, analytical reconstruction and iterative reconstruction are two common PET reconstruction categories. By comparison, the first method is a linear analytical algorithm. During the reconstruction, the analytical model is faster and allows easier control of spatial resolution and noise correlations. The iterative algorithm, in the last ten years, plays an

increasingly significant role in clinical PET. Unlike analytical method which assumes a continuous data sampling, the iterative algorithm depends on a discrete representation of both data and the image reconstructed, and therefore improves the image quality by using more accurate modeling of the data acquisition. In this section, two categories of algorithm will be explicitly introduced.

### 1.3.1 Analytical Reconstruction Methods

If a pair of unscattered photons is detected by two different detectors, the straight line connecting the center of the two detectors is known as the LOR. In 2D PET, the standard parameterization of data uses  $p(s, \theta)$  to represent the number of detected LORs for a particular pair of variable  $(s, \theta)$  where radial variable  $s$  describes the distance between the origin ( $O$ ) to the LOR and  $\theta$  is the slope of the LOR, varying from  $0^\circ$  to  $180^\circ$ . Figure 1-10 is the representation of a variable pair. The detected LORs  $p(s, \theta)$  can be considered as the projections of the activity distribution. If  $\lambda(x, y)$  is used to describe the tracer activity distribution, then the integral of the activity distribution along a certain LOR represents the number of coincidences detected by the corresponding pair of detectors. Mathematically, the transformation from  $\lambda(x, y)$  to  $p(s, \theta)$  is known as Radon transform, and can be expressed as:

$$p(s, \theta) = \iint_{-\infty}^{+\infty} \lambda(x, y) \cdot \delta(x \cos \theta + y \sin \theta - s) dx dy \quad (1-23)$$

Since the activity distribution is the image that needs to be reconstructed, and the projections are the data collected, thus the reconstruction of PET is a reverse process of above expression, which is usually known as the back-projection process. By using

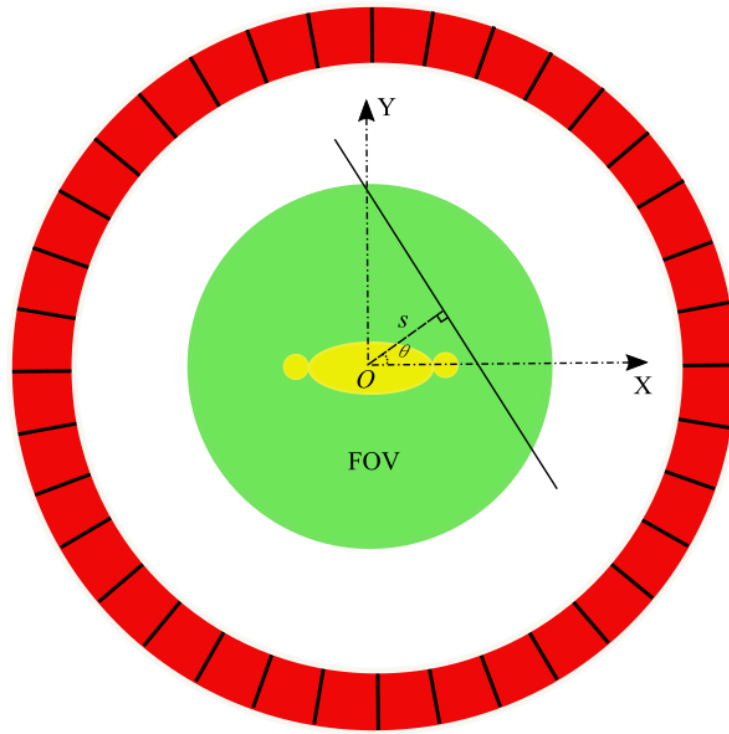


Figure 1-10. A projection in the PET field-of-view (FOV). The distance from the origin point ( $O$ ) to the projection line is  $s$ . The angle  $\theta$  represents the direction of the projection.

detected projections  $p(s, \theta)$ , the reconstructed activity distribution  $BP(x, y)$  through back-projection can be given as:

$$BP(x, y) = \int_0^{\pi} p(s, \theta) d\theta. \quad (1-24)$$

However, simply employing equation (1-24) to reconstruct the activity image will result in blurring of the generated image. Adequate frequency domain filters are needed to improve the image quality. The most common analytical algorithm with filters is called filtered back-projection (FBP). The cornerstone of this technique is the central section theorem (also known as the projection slice theorem). It indicates the relationship between the 1-

dimensional Fourier transform of the projection function  $p(s, \theta)$  with respect to radial variable  $s$  and the 2-dimensional Fourier transform of activity distribution  $\lambda(x, y)$  by:

$$P(v, \theta) \equiv \int_{-\infty}^{+\infty} p(s, \theta) e^{-i2\pi sv} ds = F(v \cos \theta, v \sin \theta) \quad (1-25)$$

where

$$F(\alpha, \beta) = \int_{-\infty}^{+\infty} \int_{-\infty}^{+\infty} \lambda(x, y) e^{-i2\pi(\alpha x + \beta y)} dx dy \quad (1-26)$$

With equation (1-25) and (1-26), the procedure of using FBP in PET reconstruction can be summarized as follows:

- (i) Choose projection data in a particular angle  $p(s, \xi)$
- (ii) Calculate  $P(v, \xi)$ , the 1-dimensional Fourier transform of  $p(s, \xi)$
- (iii) Calculate the filtered projection,  $P(v, \theta) \times h(s)$
- (iv) Calculate the inverse Fourier transform of the filtered projection
- (v) Back project the activity distribution for angle  $\xi$
- (vi) Repeat step (i)-(v) until all angles are considered

The performance of the FBP depends on the selection of the filter. Further details regarding filters such as ramp filter, Shepp-Logan filter, and Hann filter can be found in [19].

### 1.3.2 Iterative Reconstruction Methods

The concept of iterative reconstruction is to estimate an image (activity distribution) to be closest to the actual image. This process can be described mathematically as estimating an activity distribution  $\lambda$  that satisfies the equation  $p = A\lambda$ , where  $A$  is the system matrix

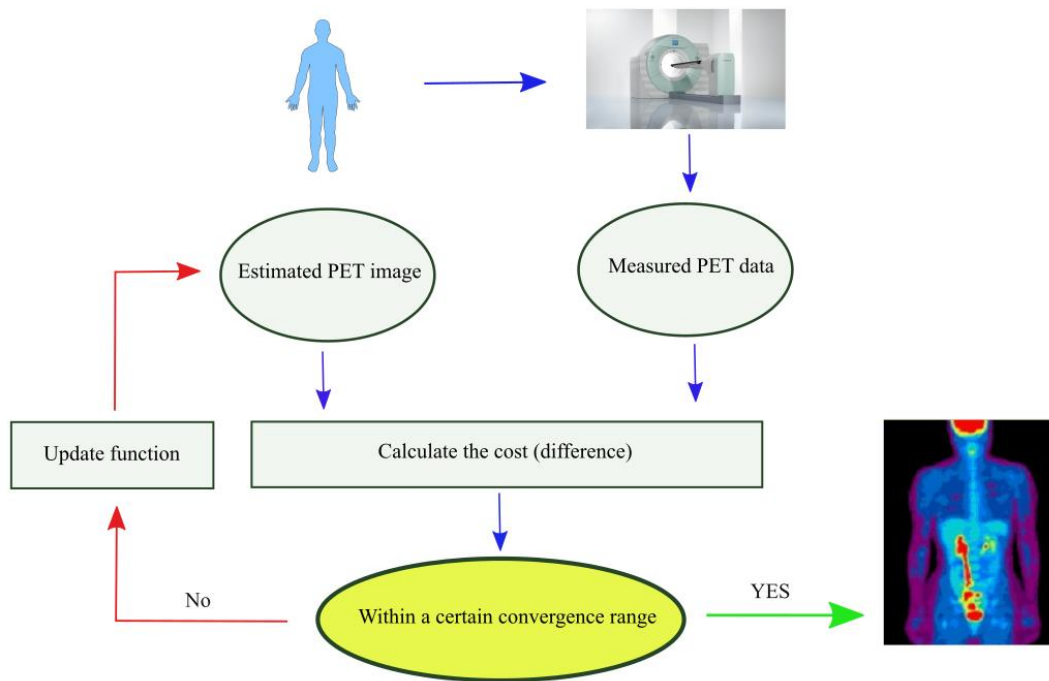


Figure 1-11. The flow chart of a typical iterative process.

for a particular PET system, and  $p$  is the acquired projections. The iteration reconstruction starts with a process called forward projection. The estimated projections ( $p^*$ ) is first calculated using the estimated image  $\lambda$ . If the estimated projections  $p^*$  is different than the acquired projections  $p$ , the gap between them is then used to update the estimated image. The process of updating is an important part of an iterative method. It typically consists of two steps: a cost function and an update function. The cost function gives the cost estimation from the estimated projections  $p^*$  to the recorded projections  $p$ , the update function uses the cost to update  $\lambda$ , then calculating a new estimated image  $\lambda^*$ . This process is repeated until  $\lambda$  and  $\lambda^*$  reach convergence or fall within a fixed convergence range. Figure 1-11 is the flow chart of a typical iterative process.

A commonly used iterative reconstruction method is the maximum likelihood expectation

maximization (MLEM) algorithm where the reconstruction process is governed by the equation below:

$$p_j = A_{i,j}\lambda_i \quad (1-27)$$

in which  $p_j$  is the recorded value in the  $j^{th}$  projection element,  $\lambda_i$  is the activity in the  $i^{th}$  pixel in the image.  $A_{i,j}$  is the system matrix that accounts for effects such as attenuation, scattering and blurring, describing the probability of a true coincidence annihilated at the  $i^{th}$  pixel being detected by the  $j^{th}$  detector pair. Equation (1-27) is considered as the Radon transform of the activity distribution  $\lambda_i$ , weighted by the geometry factor  $A_{i,j}$ . It needs to mention that the size of  $A_{i,j}$  can be quite different depending on the geometry of PET systems and patient sizes. Once the system matrix is established through either simulation or calculation, the MLEM algorithm defines the iteration equation as follows:

$$\lambda_i^{k+1} = \frac{\lambda_i^k}{\sum_{j=1}^N A_{ij}} \sum_{j=1}^N \frac{p_j A_{ij}}{\sum_{i'=1}^M A_{i'j} \lambda_{i'}^k} \quad (1-28)$$

Where  $N$  and  $M$  are the total number of projections and pixels in images,  $\lambda_i^k$  and  $\lambda_i^{k+1}$  denote the value of pixel number  $i$  at  $k^{th}$  and  $(k + 1)^{th}$  iteration, respectively. The iteration process is only completed when the difference between  $\lambda_i^{k+1}$  and  $\lambda_i^k$  lies in a pre-determined limit, or after a certain number of iterations. In contrast, unlike FBP which has only one backward projection calculation, the MLEM spends a significant amount of time repeating the forward projections, which increases the computational burden. However, since the MLEM can reconstruct images with better SNR and fewer artifacts, much effort

has been put into the development of acceleration techniques. The ordered-subset expectation maximization (OSEM) is one of the methods available. This technique can achieve convergence more quickly by dividing the projections data into subsets and applying the MLEM algorithm to each of them.

To use equation (1-28) in an MLEM algorithm, the data is required to be saved in the form of sinograms. Most reconstruction techniques use this mode of data, with each sinogram formed by counting the number of similar LORs. Another mode of data acquisition is “list-mode”, which allows each coincidence to be recorded separately. Compared to sinograms, list-mode has the advantage of avoiding incomplete data acquisition. This way of recording, to some degree, changes the notation of MLEM. Thus, equation (1-28) can be re-written as:

$$\lambda_i^{k+1} = \frac{\lambda_i^k}{\sum_{j=1}^{N'} A_{ij}} \sum_{j=1}^{N'} \frac{1}{\sum_{i'=1}^M A_{i'j} \lambda_{i'}^k} A_{ij} \quad (1-29)$$

where  $N'$  represents the total number of saved LORs. This work was developed using equation (1-29).

## 1.4 Data Corrections in PET

To obtain a high-quality image, a large number of corrections need to be applied before the reconstruction. In general, these correction techniques account for errors such as random coincidences, scattered coincidences, photon attenuation, dead time and partial volume effects. Considering the scope of this work, only corrections for scattered coincidences and photon attenuation are introduced in this section. The remaining correction techniques are

available in [20]

### 1.4.1 Scatter Correction

After the emission from positron-electron annihilation, one or both of the 511 keV photons are likely to experience the Compton Scatter events in the human body or PET detector. Generally, the inclusion of scattered gamma ray results in significant degradation in both image quality and quantitative accuracy. An energy window (typically from 350 keV to 650 keV) is set to block the scattered photons, but a small proportion of them are usually accepted, which is referred to as scatter fraction (SF). The scatter fraction usually ranges from about 15% to 25% in 2D mode or septa extended cases. When dealing with obese patients in a 3D PET system where the SF can be as high as 40-60%, this issue is more serious [23-25]. Therefore, several correction methods such as empirical scatter corrections, multiple energy window techniques, convolution and deconvolution approaches and simulation-based scatter corrections, are proposed to handle this problem.

Empirical scatter corrections are the simplest approach among all methods. They make use of the unique differences between scattered events and true coincidences, and then fit an analytical function to the scatter tails outside the object in projection space. The basis of this technique is that any coincidence recorded outside the object must come from a scattering event. By using a smoothly varying function, the scattered distribution can be estimated. Empirical scatter corrections have the merit of simple implementation and efficient computation but have the disadvantage that for most of the heterogeneous tissues, the scatter distribution cannot be well approximated by a smooth analytical function [9].

Multiple energy window techniques are widely employed and investigated for single

photon emission computed tomography (SPECT). These approaches are based on two observations. (1) Compared to coincidences recorded near the photopeak in the single photon energy spectrum, a higher proportion of Compton scattered events is recorded in the region below this photopeak; (2) A critical energy limit can be found above which only true coincidences can be recorded. By employing several energy windows set below and above the photopeak window, data within each energy windows can be used together to estimate the scatter contribution [9].

Unlike previous techniques which obtain the scatter distribution through auxiliary measurement, many convolution and deconvolution approaches model the scatter distribution with an integral transformation of the true activity distribution with a scatter response function. However, the true activity distribution is usually substituted by the recorded projection data in the photopeak window, since it cannot be truly measured. The scatter response is often assumed to be position-related and is therefore measured using a line source positioned at regular intervals across the scanner's FOV. By subtracting the scatter estimate from the saved projections, the data after scatter correction can be eventually determined [9].

Simulation-based scatter correction is so far the most accurate and practical approach to correct for scattering events in PET due to the precise understanding of physics principles that govern photon interactions with matter. It starts with the initial estimates of the attenuation map in the scattering medium and the scatter-free map of activity distribution. Once these two maps are determined, the scatter contribution can be estimated in an either analytical or numerical way. In an analytical approach, only one of the two photons is assumed to undergo a Compton scatter event, and thus the single scatter coincidence rate

at each LOR can be calculated. Except for dealing with obese patients, this approach has been shown to give a good estimate of the scatter distribution for most cases. The numerical method is usually operated using Monte Carlo simulation. This is the most robust approach to estimate scatter contribution since it not only allows separated simulation of the scattered and unscattered photons but also enables the simulation of scattered photons distribution for any scanner geometries with various emissions and different attenuation distributions. In this method, every photon is “tracked” once it is generated. Specifically, two 511 keV photons are produced at the point of origin defined by the initial estimate of the radiotracer distribution map. Each of these photons is then emitted at a random angle. When photons travel through the scattering medium (defined by the estimate attenuation map), they interact with the matter under the control of a “kernel” which accounts for the type and likelihood of different interactions being determined by photon interaction cross-sections [9]. After sufficient computation, an accurate and reliable scatter correction can be obtained.

#### **1.4.2 Attenuation Correction**

A coincidence is the simultaneous detection of both photons generated by a positron-electron annihilation event. When this pair of photons passes through the object, one or both of them can be absorbed or scattered out of the FOV. Therefore, the coincidence cannot be recorded. For photons with 511 keV in PET imaging, over 9/10 photons can be attenuated along a certain LOR before they are detected [21]. Moreover, the attenuation effect is not uniform for all coincidences. The longer the intersection between the LOR and the object is, the greater the attenuation effect will be. Figure 1-12 shows the artifacts due to attenuation effect. As shown in Figure 1-12 (b), a 35 cm circle phantom filled with water was simulated. Figure 1-12 (a) was reconstructed using MLEM reconstruction without

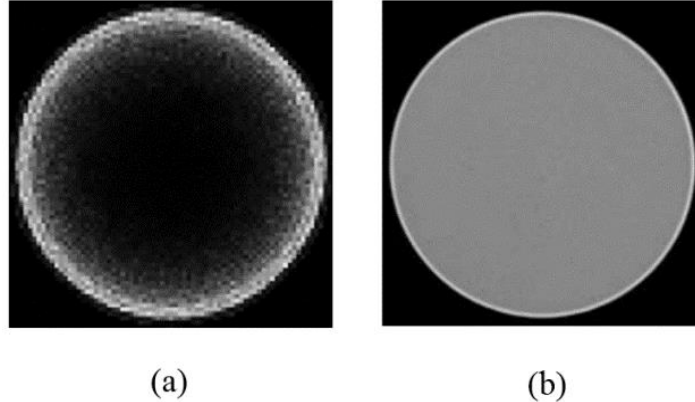


Figure 1-12. A phantom image reconstructed without attenuation correction. (a) The reconstructed image without attenuation correction. (b) The true radionuclide activity distribution.

attenuation correction. A much higher intensity can be observed at the edge of the phantom compared to the intensity of the inner region. Such inaccurate reconstruction cannot fulfill the task of PET imaging, especially when deeply seated lesions need to be reconstructed. Therefore, a robust attenuation correction is required for artifact-free images.

Once a pair of photons is produced by an annihilation event, the probability of their detection depends on the combined path of both photons. Since the entire path does not change for all sources lying on the same LOR and the calculation of attenuation is based on the sum of the paths from the two photons, the probability of attenuation is, therefore, independent of the source position. Figure 1-13 illustrates this process.

In general, the attenuation correction methods can be divided into two categories: measured attenuation correction and calculated attenuation correction.

By using measured attenuation correction, the probability of attenuation for each LOR is

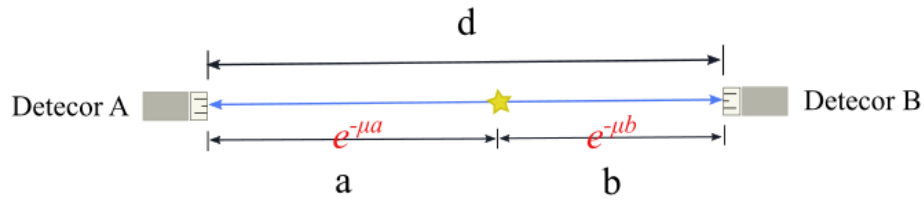


Figure 1-13. A true coincidence is detected at detector A and B in which a LOR is determined (blue line). As long as the position of the annihilation position (yellow star) lies on the LOR, the calculation of the attenuation does not change.

determined by the ratio of the count rate from a transmission source (obtained by placing a source outside the object) to the unattenuated count rate (gained from the same source when the object is removed). As a relatively accurate method accounting for attenuation, the direct measurement can be performed using different sources such as a set of ring sources and a rotating rod source. This type of measurement is routinely performed in the PET scan since it enables a direct measurement of attenuation without considering the outline of the subject, the variance in attenuation coefficients and detector configurations. However, this method may suffer statistical errors if the number of counts for each LOR cannot be accurately determined [9].

Unlike direct measurement which significantly increases the time to perform a PET scan, the calculated method assumes a regular geometric body outline and constant tissue density of the object. This assumption allows the attenuation factor of each LOR to be determined based on the constant attenuation along a chord through the object. However, this study may only be valid for regularly shaped objects such as brains. When imaging other regions of the body, this approach can either underestimate or overestimate the attenuation by 20%

or 12%, respectively [22].

## **1.5 Motivation and Objectives of the Study**

In commercial PET/CT systems, patient movement, either during the PET acquisition or between the PET and the CT acquisitions can generate artifacts that may be subtle, yet lead to erroneous interpretation of the study [26]. Misalignment between CT and PET images because of patient motion can cause photopenic artifacts, particularly when an iterative reconstruction algorithm is applied [26-27]. The underlying cause of these artifacts is the result of incorrect scatter corrections [27]. This problem may be solved, if the reconstruction algorithm can be designed to make direct use of the scattered photons, instead of simply correcting for them by subtracting an estimate of the scatter contribution from the true coincidences [27-28]. These approaches expand the range of usable photons, reducing patient dose, shortening the acquisition duration, and thus improving patient tolerance and decreasing the significance of patient motion.

The goal of this project is to use all scattered photons, including single, dual and multiple scattered coincidences, to enhance PET imaging systems. The author hypothesizes that (1) a new algorithm, which is independent of the number of Compton scattering interactions and less sensitive to the high energy resolution requirements of earlier approaches, can be developed. (2) An attenuation correction method using a restricted Klein-Nishina cross-section can also be established to correspond with the new algorithm.

## 2. Methodology

As discussed in section 1.1.2.4, Compton scattering is the most dominant interaction for photons at 511 keV in tissue. A recent report shows that more than 99.7% of interactions in water are Compton scattering events [29]. Traditionally, scattered photons are regarded as contaminations, since the LORs given by scattered coincidences are unlikely to identify the true annihilation position. Therefore, images reconstructed without adequate scatter corrections will compromise quantitative accuracy and degrade image contrast [30]. Consequently, a number of methods for estimating and correcting for scattered coincidences in PET have been proposed [31-37]. Most of these techniques estimate a scatter sinogram that is used to subtract the scatter from the projection data [38] in pre-correction methods [39] or as a constant additive term incorporated in a reconstruction algorithm [40-42]. Inaccurate estimation of the scatter sinogram introduces biases in the activity distribution. The subtraction-based correction methods destroy the Poisson nature of the data that results in the reduction of system sensitivity and the increase of image noise [43].

Instead of subtracting scattered photons from the raw data, Conti [45] and Sun [44] independently proposed reconstruction methods for processing true and single scattered coincidences with and without time-of-flight (TOF) information, respectively. These methods opened the door for making use of scattered photons to reconstruct images and have successfully demonstrated that single scattered coincidences have the potential to localize the distribution of radiotracer emitters and improve the image quality. However,

true and single scattered coincidences cannot be uniquely identified in a clinical PET system, since realistic datasets contain single, dual and multiple scattered photons, and there is no way to distinguish them. For typical patients, dual and multiple scattered coincidences can account for 15-20% of data, and this ratio can be greater when imaging an obese patient. Thus, a robust method that is capable of handling the higher order scattered coincidences is needed [46].

This work generalises the work by Sun et al. in that each pair of detected photons, instead of being assumed to experience only one Compton scatter event in one of two photons, is considered as a dual-scattered photon pair. It can be shown that attenuation correction methods based on LORs are no longer suitable for scatter based reconstruction algorithms and a new approach based on restricted attenuation coefficients, calculated by integrating the differential Klein-Nishina cross-section over a restricted energy range, is used.

Coincidences in this study were obtained by Monte Carlo simulation so that the entire history of each photon can be tracked. By combining or subtracting each group of true, random, single scattered and multiple scattered coincidences, the desired dataset can be purposely created, before carrying out the reconstruction. In this work, all data were recorded in list-mode format, and equation (1-29) was used for the reconstruction processes. Since this work aims to identify the benefit of using the photons scattered within the body, interactions inside the detectors are ignored. Detectors with an ideal energy resolution were initially used to compare different algorithms. Following this, the feasibility of using this approach for clinical applications was investigated by setting the energy resolution to more realistic values.

## 2.1 Activity Distribution Reconstruction

### 2.1.1 Reconstruction Theory using Dual-scattered Coincidences

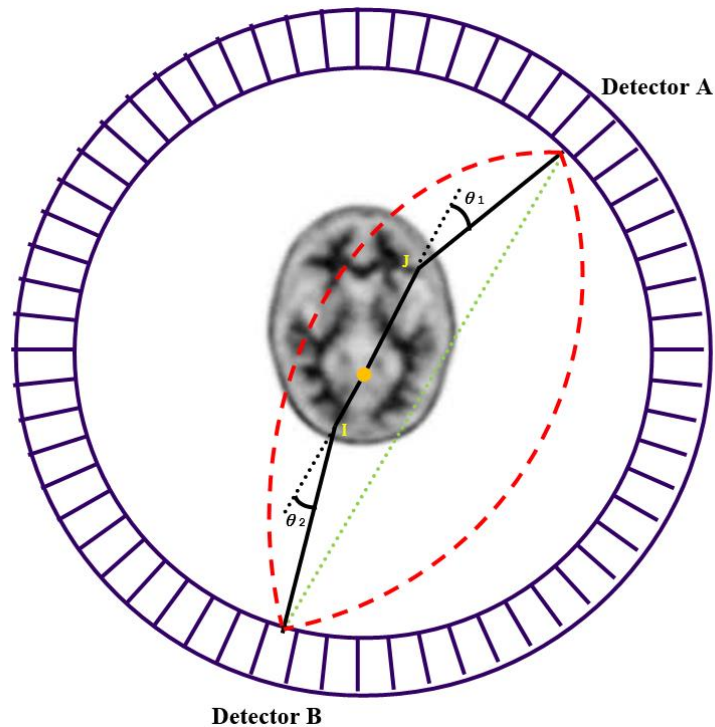


Figure 2-1. The diagram of a dual Compton scattering event in the patient. The two anti-parallel photons are generated at the annihilation position shown by the yellow dot. Both photons suffer a Compton scattering interaction, measured by detector A and B, respectively. This figure also shows two circular arcs (TCA) that, displayed as dashed red curves, encompass the possible annihilation positions.

Figure 2-1 is a schematic depicting a dual-scattered event in a patient. In this case, two 511 keV photons are emitted after a positron-electron annihilation at the yellow dot. These two photons individually undergo one Compton scattering event on dot *I* and *J*, and are then measured by detector *A* and *B*, respectively. If the energy resolution of the detector is

ideal and no other interactions happen inside the detectors, the energy of each photon can be accurately measured. By making use of the equation (1-9), the relationship between the recorded energy and scattering angle can be given by:

$$\begin{aligned}\cos \theta_1 &= 2 - \frac{E_\gamma}{E_1} \\ \cos \theta_2 &= 2 - \frac{E_\gamma}{E_2}\end{aligned}\tag{2-1}$$

where  $E_1$  and  $E_2$  represent the detected energies of two photons,  $\theta_1$  and  $\theta_2$  are scattering angles corresponding to each scattered photon, which show the direction change between the incident and the scattered photons.  $E_\gamma$  is the energy of the incident photon, which is equal to 511 keV for this circumstance.

As shown in Figure 2-1, the sum of each scattering angle ( $\theta = \theta_1 + \theta_2$ ) is then used to define two circular arcs (TCA) in 2D (red lines) or a surface obtained by rotating the 2D arc around its axis in 3D mode. These TCAs connect the two detectors and an area, which encompass the real annihilation position for this particular dual-scattered photon pair.

To determine the shape and the size of the TCA, the total scattering angle  $\theta$  is used. Figure 2-2 gives different TCAs for various  $\theta$ . By employing this approach, the summation for each coincidence is over the area confined by the TCA, instead of along the LOR as done in conventional PET imaging methods. When  $\theta$  is more than  $90^\circ$ , the area determined by the corresponding TCAs is wider than the PET system (for typical ring PET systems), and thus encompasses the whole patient. This oversized area does not contribute to identifying the position of the actual annihilation source, limiting the total scattering

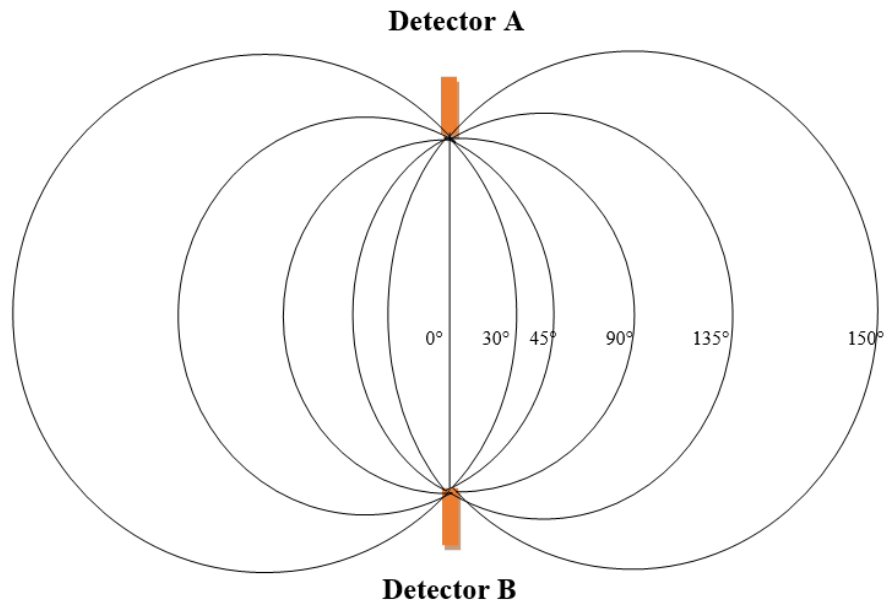


Figure 2-2. The TCAs sizes and shapes vs. the total scattering angles for the same detector pair. Each TCA pair consists of two symmetrically circular arcs where the inner to the outer arcs are corresponding to scattering angles of 0, 30°, 45°, 90°, 135° and 150°, respectively. If the scattering angle is smaller than 90°, the TCAs are made up of two minor arcs; If the scattering angle is 90° the TCAs are a circle; when the scattering angle is larger than 90° the TCAs are made up of two major arcs, and will be discarded in this work.

angle using this technique to 90°. If not explicitly specified, the following mathematical deductions are all based on this prerequisite.

Figure 2-3 demonstrates why the annihilation position can be constrained to the area defined by the TCAs. A pair of dual-scattered coincidences are detected by detectors A and B. By using the Compton equation, the scattering angle  $\theta_1$  and  $\theta_2$  for each photon can be determined based on their measured energies. The total scattering angle  $\theta$  is calculated

using the summation of each scattering angle, and is further used to determine the TCAs. In this figure, only one of the TCAs (red dotted curve) is shown as the other half is symmetric. One source point  $O$  (green dot) is set beyond the TCA. Since the source can emit photons in any directions, two cases are considered separately.

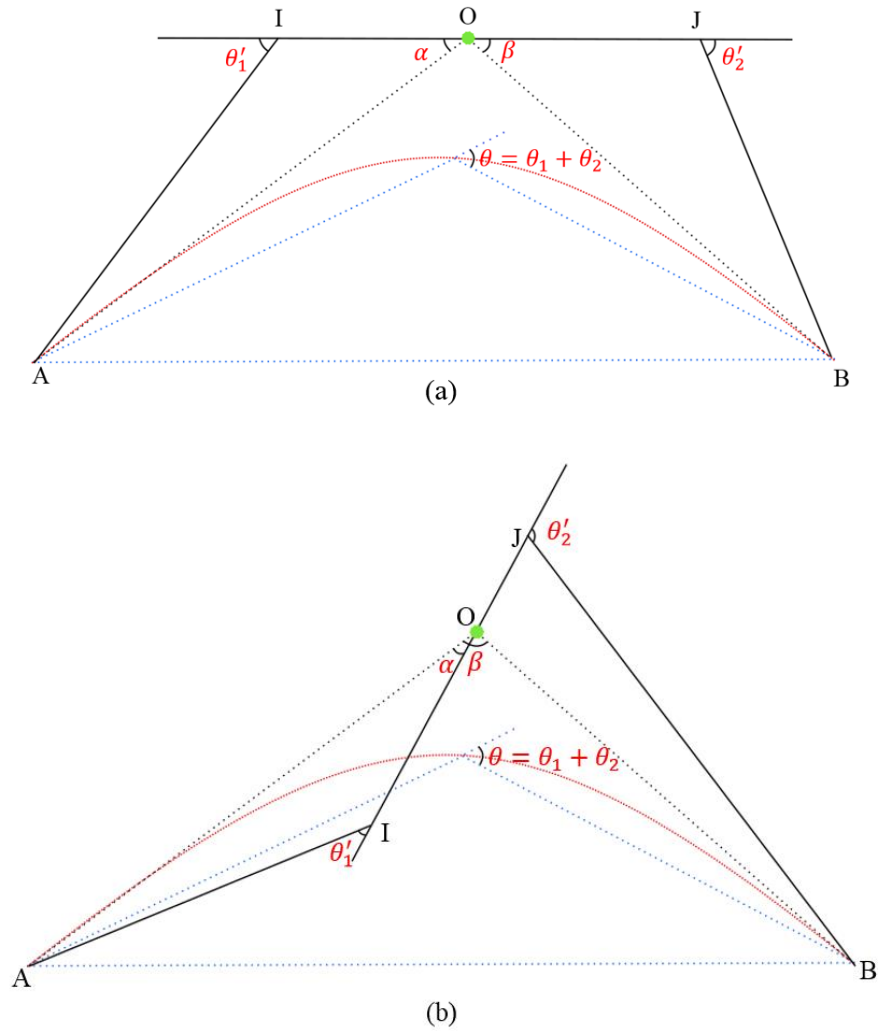


Figure 2-3. The schematic figures of confining the real annihilation position of a dual-scattered coincidence pair using TCAs. Two cases are illustrated where (a) represents the direction of initial emitted photons  $IJ$  does not lie in-between  $OA$  and  $OB$ , whereas, (b) shows the case of the direction of initial emitted photons lies in-between  $OA$  and  $OB$ .

The first case is illustrated in figure 2-3 (a) where the direction of the two emitted photons  $IJ$  does not lie in-between  $OA$  and  $OB$ . Two photons individually undergo a Compton scattering event before hitting the detector A and B with corresponding scatter angles  $\theta'_1$  and  $\theta'_2$ , respectively. Based on adequate observation, it can be shown that:

$$\theta'_1 > \alpha; \quad \theta'_2 > \beta \quad (2-2)$$

In addition, as the source point is outside the constrained area, the relationship between  $\alpha$ ,  $\beta$  and  $\theta$  can be given by:

$$\alpha + \beta > \theta \quad (2-3)$$

By combining equation (2-2) and (2-3), we can conclude that:

$$\theta'_1 + \theta'_2 > \theta = \theta_1 + \theta_2 \quad (2-4)$$

Equation (2-4) demonstrates that at source point  $O$ , if the direction of initial photons does not pass through triangle  $\Delta OAB$ , a dual-scattered coincidence pair cannot separately reach detectors A and B given the summation of scattering angle is equal to  $\theta$ .

Figure 2-3 (b) shows another case where the direction of initially emitted photons lies in-between  $OA$  and  $OB$ . It can be shown that:

$$\theta'_1 > \alpha; \quad \theta'_2 > 180^\circ - (\beta - \alpha) \quad (2-5)$$

Similarly, as the source point is outside the constrained area, the relationship between  $\beta$  and  $\theta$  can be given by:

$$180^\circ - \beta > \theta \quad (2-6)$$

Combining equations (2-5) and (2-6), the following expression can be obtained:

$$\theta'_1 + \theta'_2 > \theta + 2\alpha \quad (2-7)$$

Note that the direction of the initial photons intersects with triangle  $\Delta OAB$ , so it must have a condition that  $\alpha > 0$ . Therefore, it can be concluded that:

$$\theta'_1 + \theta'_2 > \theta + 2\alpha > \theta \quad (2-8)$$

Equation (2-8) indicates that at source point  $O$ , even if the initial photons direction passes through triangle  $\Delta OAB$ , a dual-scattered coincidence pair cannot separately reach detectors A and B either when the summation of scattering angle is equal to  $\theta$ .

Therefore, given the positions of two detectors and the energy loss of two photons, the position of the real annihilation source for this particular pair of dual-scattered photons can be strictly constrained to the area defined by the corresponding TCAs. This dual-scattered model is an extension work of both LOR and single-scattered model. In the limiting case where the scattering angle approaches zero, the dual-scattered coincidence approaches the true coincidences, since both photons can be regarded as being scattered at  $0^\circ$  (see figure 2-2). The single-scattered event can also be considered as a dual-scattered event where one photon is scattered at  $\theta$  while the other one is scattered at  $0^\circ$ . Thus, true and single-scattered coincidences can be taken as the subsets of dual-scattered coincidences.

### 2.1.2 Multiple Scattered Coincidences Reconstruction

In PET reconstruction, multiple scattered photons are difficult to deal with because the PET system can only provide limited information such as total energy loss and final detected positions. Details about the number of interactions and the energy loss of each interaction cannot be explicitly determined. In this section, the localization of source distribution using multiple scattered coincidences is attempted.

Compton equation (1-8) gives an expression in terms of the scattering angles and the photon energies. Through transformation, it can be written in another form:

$$\frac{1}{E'_\gamma} - \frac{1}{E_\gamma} = \frac{1}{m_e c^2} (1 - \cos \theta) \quad (2-9)$$

in which  $\theta$  is the scattering angle,  $E_\gamma$  and  $E'_\gamma$  represent the energies of the photon before and after the interaction, respectively.

The total energy loss is fixed, i.e.  $E_\gamma - E'_\gamma$ . If this photon loses its energy through  $N$  interactions, it is then considered as a multiple scattered photon. Assuming the energy of incident photon is  $E_0$ , the scattering angle and the remaining energy of this photon after  $N^{th}$  interaction are  $\theta_N$  and  $E_N$ , respectively. By using equation (2-9), a series of equations can be described as:

$$\frac{1}{E_1} - \frac{1}{E_0} = \frac{1}{m_e c^2} (1 - \cos \theta_1)$$
$$\frac{1}{E_2} - \frac{1}{E_1} = \frac{1}{m_e c^2} (1 - \cos \theta_2)$$

$$\frac{1}{E_3} - \frac{1}{E_2} = \frac{1}{m_e c^2} (1 - \cos \theta_3)$$

.

.

.

$$\frac{1}{E_N} - \frac{1}{E_{N-1}} = \frac{1}{m_e c^2} (1 - \cos \theta_N)$$
(2-10)

Summing these equations gives:

$$\frac{1}{E_N} - \frac{1}{E_0} = \frac{1}{m_e c^2} [N - (\cos \theta_1 + \cos \theta_2 + \dots + \cos \theta_N)]$$
(2-11)

If this photon loses its energy in one Compton scattering event, another expression can be obtained using equation (2-9):

$$\frac{1}{E_N} - \frac{1}{E_0} = \frac{1}{m_e c^2} [1 - \cos \theta_s]$$
(2-12)

where  $\theta_s$  is the scattering angle of this event and the energy loss remains the same as  $E_\gamma - E'_\gamma$ .

Comparing equation (2-11) and (2-12) and making several transformations gives equation (2-13) shown below:

$$\sum_{i=1}^N \cos \theta_i = N - 1 + \cos \theta_s$$
(2-13)

In the above equation, the number  $N$  and each individual scattering angle  $\theta_i$  cannot be measured by PET systems. Therefore, the sum of each individual scattering angle ( $\sum_{i=1}^N \theta_i$ ) is used to address the annihilation position.

**Conjecture.** Assume that the maximum value of  $\sum_{i=1}^N \theta_i$  can be achieved when each individual scattering angle is the same and is equal to  $(\arccos \frac{N-1+\cos \theta_s}{N})$ . This conjecture can be expressed as:

$$\sum_{i=1}^N \theta_i \quad \text{max} = N \cdot \arccos \frac{N-1+\cos \theta_s}{N} \quad (2-14)$$

Equation (2-14) can be proved using the following mathematical induction:

When  $N = 1$ , this conjecture is correct, since  $\theta_1 = \theta_s$ .

When  $N = 2$ ,

Let  $(N - 1 + \cos \theta_s) = A$ . Equation (2-13) can be written as:

$$\cos \theta_1 + \cos \theta_2 = A \quad (2-15)$$

Let  $\cos \theta_1 = x$  ( $0 < x < A$ ).  $\sum_{i=1}^N \theta_i$  can be expressed as a function  $\mathcal{F}_2(x)$ :

$$\sum_{i=1}^{N=2} \theta_i = \theta_1 + \theta_2 = \arccos(x) + \arccos(A - x) = \mathcal{F}_2(x) \quad (2-16)$$

The first derivative of  $\mathcal{F}_2(x)$  is:

$$\mathcal{F}_2(x)' = -\frac{1}{\sqrt{1-x^2}} + \frac{1}{\sqrt{1-(A-x)^2}} \quad (2-17)$$

$\theta_1 + \theta_2$  reaches the maximum value when  $\mathcal{F}_2(x)' = 0$ , which gives  $x = A/2$ . Therefore, the conjecture is proved when  $N = 2$ , and can be specifically written as:

$$\sum_{i=1}^2 \theta_i \underset{\max}{=} = 2 \cdot \arccos \frac{2-1+\cos \theta_s}{2} \quad (2-18)$$

When  $N = 3$ :

Let  $(N - 1 + \cos \theta_s) = A$ . Equation (2-13) can be written as:

$$\cos \theta_1 + \cos \theta_2 + \cos \theta_3 = A \quad (2-19)$$

Let  $\cos \theta_3 = x$  ( $0 < x < A$ ), then  $\cos \theta_1 + \cos \theta_2 = A - x$ . By using equation (2-18), it can be shown that  $\theta_1 + \theta_2$  reaches the maximum value when  $\theta_1 = \theta_2 = \arccos \frac{A-x}{2}$ .

Again,  $\sum_{i=1}^N \theta_i$  can be then expressed as a function  $\mathcal{F}_3(x)$ :

$$\sum_{i=1}^{N=3} \theta_i = \theta_1 + \theta_2 + \theta_3 = \arccos(x) + 2 \arccos\left(\frac{A-x}{2}\right) = \mathcal{F}_3(x) \quad (2-20)$$

The first derivative of  $\mathcal{F}_3(x)$  is:

$$\mathcal{F}_3(x)' = -\frac{1}{\sqrt{1-x^2}} + \frac{1}{\sqrt{1-\left(\frac{A-x}{2}\right)^2}} \quad (2-21)$$

Similarly,  $\theta_1 + \theta_2 + \theta_3$  reaches a maximum value when  $\mathcal{F}_3(x)' = 0$ , which gives  $x =$

$A/3$ . Therefore, the conjecture is proved when  $N = 3$ , and can be specifically written as:

$$\sum_{i=1}^3 \theta_i \quad \text{max} = 3 \cdot \arccos \frac{3 - 1 + \cos \theta_s}{3} \quad (2-22)$$

Repeat this process until  $N$ ,  $\sum_{i=1}^N \theta_i$  can be expressed as a function  $\mathcal{F}_N(x)$ :

$$\sum_{i=1}^N \theta_i = \arccos(x) + (N - 1) \arccos \left( \frac{A - x}{N - 1} \right) = \mathcal{F}_N(x) \quad (2-23)$$

The first derivative of  $\mathcal{F}_N(x)$  is:

$$\mathcal{F}_N(x)' = -\frac{1}{\sqrt{1-x^2}} + \frac{1}{\sqrt{1 - \left(\frac{A-x}{N-1}\right)^2}} \quad (2-24)$$

The maximum value of  $\sum_{i=1}^N \theta_i$  can be achieved when  $\mathcal{F}_N(x)' = 0$ , which gives  $x = A/N$ . Therefore, when each individual scattering angle is equal to  $(\arccos \frac{N-1+\cos \theta_s}{N})$ ,

$\sum_{i=1}^N \theta_{i_{max}}$  is obtained, i.e.  $\sum_{i=1}^N \theta_{i_{max}} = N \cdot \arccos \frac{N-1+\cos \theta_s}{N}$  (conjecture proved).

Figure 2-4 shows how equation (2-14) and each component ( $N$  and  $\arccos \frac{N-1+\cos \theta_s}{N}$ ) change while  $N$  increases.  $\theta_s$  can be calculated using the measured photon energies (for total scattering angles of less than  $90^\circ$  while employing this approach). Here,  $\theta_s$  is given a value of  $45^\circ$  as an example. It can be observed that the maximum value of  $\sum_{i=1}^N \theta_i$  increases with increasing  $N$ . This can be proved by calculating the first derivative of equation (2-14), which is positive for all  $N > 1$ .

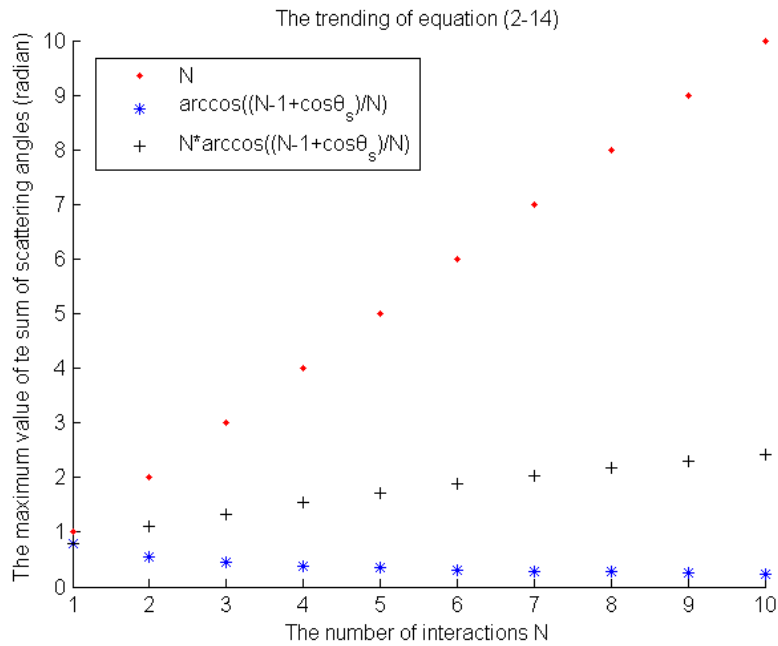


Figure 2-4. The trending graph of equation (2-14). Black “+” line shows the trending of this function. The blue and red dotted lines show the component this expression, respectively. The maximum value of the sum of each individual scattering angles increases with the increasing number of interactions, and can reach a value greater than  $\pi$ .

Thus, if one scattered photon is detected, its energy loss can be used to calculate  $\theta_s$ . However, since the number of interactions cannot be determined by the PET system, the sum of each individual scattering angle can be greater than  $\theta_s$ . In a particular case where the photon is scattered at the same scattering angle every time, the sum of scattering angle is maximum. The maximum value of the sum increases with increasing  $N$  and therefore can reach a value greater than  $\pi$ .

This deduction implies that there is no way to address the annihilation position for multiple scattered events as what has been done for true, single-scattered and dual-scattered

coincidences. In practice, every point inside the object has a probability of emitting a photon that can reach a specific detector if a number of multiple scattering events occurs.

However, the probability of undergoing many scattering interactions is relatively small. 80% measured scattered photons lose their energies in single scattered events [47]. Therefore, the dual-scattered model can represent most cases of multiple scattered events. The correlation between multiple and dual scattered photons enables activity to be estimated while applying the proposed dual-scattered model on multiple scattered events.

### 2.1.3 Generalised Dual-scattered MLEM Reconstruction Algorithm

The Generalised Dual-scattered MLEM (GDS-MLEM) reconstruction technique assumes that the probability of an annihilation occurring in a given pixel is the same for all pixels enclosed within the area constrained by the TCAs, due to the isotropic property of photon annihilation. Therefore, for a uniform activity distribution in a uniform medium (same electron density), all points within the TCAs area have the same annihilation probability, except for the points on the line of TCAs. In this algorithm,  $\langle P_{AB}(\theta_1, \theta_2) \rangle$  represents the mean number of coincidences where the two photons individually undergo a scattering event at point  $I$  and  $J$  (scattering angle  $\theta_1$  and  $\theta_2$ ) and are detected in  $A$  and  $B$  (see figure 2-1). With activity distribution of  $f(x)$  and electron density of  $\rho_e(x)$  over the object, it can be calculated that  $\langle P_{AB}(\theta_1, \theta_2) \rangle$  is proportional to:

$$\begin{aligned} \langle P_{AB}(\theta_1, \theta_2) \rangle \propto & \iint_{AB} \int_I^J f(x) dx \cdot \rho_e(I) \cdot \frac{d_e \sigma^{KN}}{d\theta_1} \cdot \rho_e(J) \\ & \cdot \frac{d_e \sigma^{KN}}{d\theta_1} \cdot Att_{AB,IJ} \, dl dJ \end{aligned} \quad (2-25)$$

in which  $Att_{AB,IJ} = e^{-(\int_A^I \mu_1 dl + \int_I^J \mu_0 dl + \int_J^B \mu_2 dl)}$  is the attenuation factor, where  $\mu_0$ ,  $\mu_1$ ,  $\mu_2$  are the linear attenuation coefficients for the 511 keV photon, first scattered photon and another scattered photon.  $\frac{d\sigma^{KN}}{d\theta_1}$  is the differential Compton scattering cross-section. In this approach, the electron density outside the object is assumed to be zero.

Considering the sparse number of coincidences contributing to  $\langle P_{AB}(\theta_1, \theta_2) \rangle$ , the GDS-MLEM reconstruction algorithm in a list-mode form (see equation (1-29)) can be derived as:

$$f_i^{k+1} = \frac{f_i^k}{\sum_{j=1}^N A_{ij}} \sum_{j=1}^N \frac{1}{\sum_{i'=1}^M A_{i'j} f_{i'}^k} A_{ij} \quad (2-26)$$

where  $f_i^{k+1}$  is the activity distribution of pixel  $i$  in the  $(k + 1)^{th}$  iteration.  $N$  and  $M$  represent the total number of detected coincidences and pixels in the image.  $A_{ij}$  is the element of system matrix which represents the probability of a coincidence annihilated at the  $i^{th}$  pixel being detected by the detector pair  $j^{th}$ , weighted by the Compton scattering cross-section. In other words,  $A_{ij}$  is proportional to the Compton cross-section if pixel  $i$  lies within the area defined by TCAs of the  $j^{th}$  detector pair, and is zero if outside the area. Therefore, the GDS-MLEM algorithm uses an area to localize the activity distribution, instead of constraining annihilation sources on a line defined by the traditional LOR-MLEM.

When applying the GDS-MLEM algorithm on activity reconstruction, the area defined by TCAs is an important component. In practice, the smaller the area, the more accurately the

image will be reconstructed. For most cases, the outline of the object can be used as a constraint. Figure 2-5 shows a smaller area using TCAs and the patient outline. In this case, the real annihilation source lies in the area limited by the blue dotted contour.

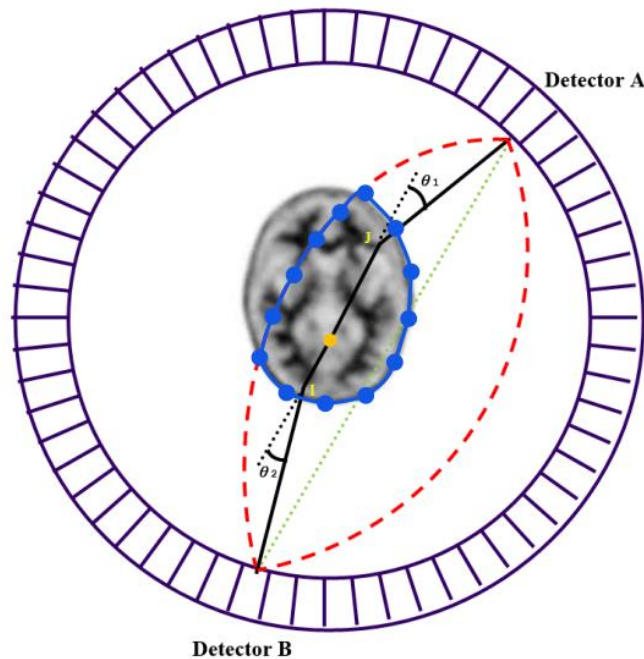


Figure 2-5. The smaller area using the outline of the imaging content. In this figure, the patient outline is used to narrow the area defined by TCAs where the space confined by the blue dotted line is the actual potential annihilation position for this particular coincidence.

## 2.2 Restricted Attenuation Correction

Figure 2-6 is the energy spectrum in which the number of photons with different energies was counted. An energy cut-off of 255 keV is used to exclude the scattered photons with scattering angles greater than  $90^\circ$ . The restricted energy threshold  $E_t$  is set to determine how many scattered coincidences are included into the reconstruction dataset, by

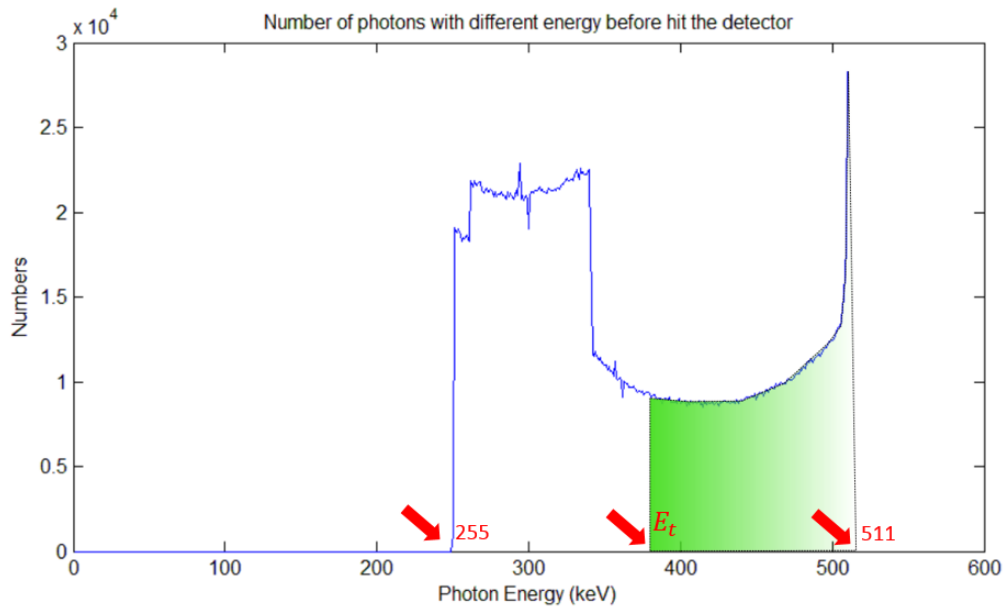


Figure 2-6. The number of photons with different energies measured by detectors. A 255 keV energy cut-off is implemented to ensure that the scattering angle of each photon is less than  $90^\circ$ .  $E_t$  is the restricted energy threshold which excludes the scattered photons below it. To avoid overcorrecting the scattered photons that have been recorded (green zone), a new attenuation correction model, which uses restricted Klein-Nishina cross-section, was established.

discarding photons with energies less than  $E_t$ . When correcting for attenuation, if the total Klein-Nishina cross-section is used without any modification, the attenuation correction will assume that all photons below 511 keV are absorbed, which results in the photons with energies between  $E_t$  and 511 keV being double-counted (green zone). This may lead to inaccurate attenuation correction and will degrade quantitative accuracy. Therefore, a restricted Klein-Nishina cross-section that only corrects for scattered photons that are not counted, i.e. those with energies below  $E_t$ , is needed.

## 2.2.1 The Ratio of the Restricted to the Total Klein-Nishina Cross-Section

By using equation (1-14), the integral of Compton cross-section can be derived as:

$$\begin{aligned}\sigma_e^{kN} &= \int_{E_1}^{E_2} \frac{d\sigma_e^{kN}}{dE} dE \\ &= \frac{\chi_0 \rho_e \pi r_0^2}{E'_0} \cdot \left[ C_1 \left( \frac{1}{\varepsilon_1} - \frac{1}{\varepsilon_2} \right) + C_2 \ln \left( \frac{\varepsilon_2}{\varepsilon_1} \right) + \varepsilon_2 \left( C_3 + \frac{\varepsilon_2}{2} \right) - \varepsilon_1 \left( C_3 + \frac{\varepsilon_1}{2} \right) \right]\end{aligned}\tag{2-27}$$

where  $E_0$  represents the initial photon energy,  $E'_0 = E_0/m_e c^2$ .  $\chi_0$ ,  $\rho_e$ ,  $r_0$  are radiation length, electron density and classical electron radius, respectively.  $E_1$  and  $E_2$  correspond to the minimum and maximum energy of the scattered photon. According to equation (1-8), it can be shown that  $E_1 = \frac{E_0}{1+2E_0/m_e c^2}$ . For the total cross-section,  $E_2 = E_0$ , whereas,  $E_2 = E_t$  for the restricted cross-section.  $\varepsilon_1$ ,  $\varepsilon_2$ ,  $C_1$ ,  $C_2$  and  $C_3$  are unitless, and can be individually expressed as:  $\varepsilon_1 = \frac{E_1}{E_0} = \frac{1}{1+2E'_0}$ ,  $\varepsilon_2 = \frac{E_2}{E_0}$ ,  $C_1 = (E'_0)^{-2}$ ,  $C_2 = 1 - \frac{2(1+E'_0)}{(E'_0)^2}$  and  $C_3 = \frac{1+2E'_0}{(E'_0)^2}$ .

Since the value of the total Compton cross-section is tabulated, the restricted Compton cross-section is not given by direct calculation. Instead, a parameter  $R_{KN}$  is used to account for the ratio of the restricted Compton cross-section to the total Compton cross-section.  $R_{KN}$  can be written as:

$$\begin{aligned}
R_{KN} &= \frac{\int_{E_1}^{E_t} \frac{d\sigma_e^{kN}}{dE} dE}{\int_{E_1}^{E_0} \frac{d\sigma_e^{kN}}{dE} dE} \\
&= \frac{\frac{\chi_0 \rho_e \pi r_0^2}{E_0'} \cdot [C_1 \left(\frac{1}{\varepsilon_1} - \frac{1}{\varepsilon_2'}\right) + C_2 \ln\left(\frac{\varepsilon_2'}{\varepsilon_1}\right) + \varepsilon_2' \left(C_3 + \frac{\varepsilon_2'}{2}\right) - \varepsilon_1 \left(C_3 + \frac{\varepsilon_1}{2}\right)]}{\frac{\chi_0 \rho_e \pi r_0^2}{E_0'} \cdot [C_1 \left(\frac{1}{\varepsilon_1} - \frac{1}{\varepsilon_2''}\right) + C_2 \ln\left(\frac{\varepsilon_2''}{\varepsilon_1}\right) + \varepsilon_2'' \left(C_3 + \frac{\varepsilon_2''}{2}\right) - \varepsilon_1 \left(C_3 + \frac{\varepsilon_1}{2}\right)]} \\
&= \frac{[C_1 \left(\frac{1}{\varepsilon_1} - \frac{1}{\varepsilon_2'}\right) + C_2 \ln\left(\frac{\varepsilon_2'}{\varepsilon_1}\right) + \varepsilon_2' \left(C_3 + \frac{\varepsilon_2'}{2}\right) - \varepsilon_1 \left(C_3 + \frac{\varepsilon_1}{2}\right)]}{[C_1 \left(\frac{1}{\varepsilon_1} - \frac{1}{\varepsilon_2}\right) + C_2 \ln\left(\frac{\varepsilon_2}{\varepsilon_1}\right) + \varepsilon_2 \left(C_3 + \frac{\varepsilon_2}{2}\right) - \varepsilon_1 \left(C_3 + \frac{\varepsilon_1}{2}\right)]}
\end{aligned} \tag{2-28}$$

In which  $\varepsilon_2' = \frac{E_t}{E_0}$ ,  $\varepsilon_2'' = \frac{E_0}{E_0} = 1$ . After adequate mathematical calculations, the above expression of  $R_{KN}$  can be simplified to:

$$R_{KN} = \frac{[(E_0')^{-2} \left(\alpha - \frac{1}{\beta}\right) + \eta \ln(\alpha\beta) + \beta \left(\gamma + \frac{\beta}{2}\right) - \varphi]}{[2(E_0')^{-1} + \eta \ln(\alpha) + \left(\gamma + \frac{1}{2}\right) - \varphi]} \tag{2-29}$$

where each parameter is listed in table 2-1.

parameter	$\alpha$	$\beta$	$\gamma$	$\eta$	$\varphi$
expression	$2E_0' + 1$	$\frac{E_t}{E_0}$	$\frac{\alpha}{(E_0')^2}$	$\left(1 - \frac{1}{(E_0')^2} - \gamma\right)$	$\frac{1}{\alpha} \left(\gamma + \frac{1}{2\alpha}\right)$

Table 2-1. The expression of each parameter in equation (2-29).

### 2.2.2 Calculation of the Total Klein-Nishina Cross-Section

With equation (2-29), the restricted Compton cross-section can be obtained using the multiplication between the ratio  $R_{KN}$  and the total Compton cross-section  $\sigma^{kN}$ .

However,  $\sigma^{kN}$  for scattered photons with energies less than 511 keV are usually used in GDS-MLEM reconstruction so that an approach to calculate the value of  $\sigma_e^{kN}$  for photons with various energies is required.

Sixty-nine different total Compton cross-sections per unit mass ( $\frac{\sigma^{kN}}{\rho}$ ) were obtained for photons with energies ranging from 170 keV to 510 keV, in steps of 5 keV, from the “National Institute of Standards and Technology (NIST) XCOM: Photon Cross Sections Database” (see Appendix).

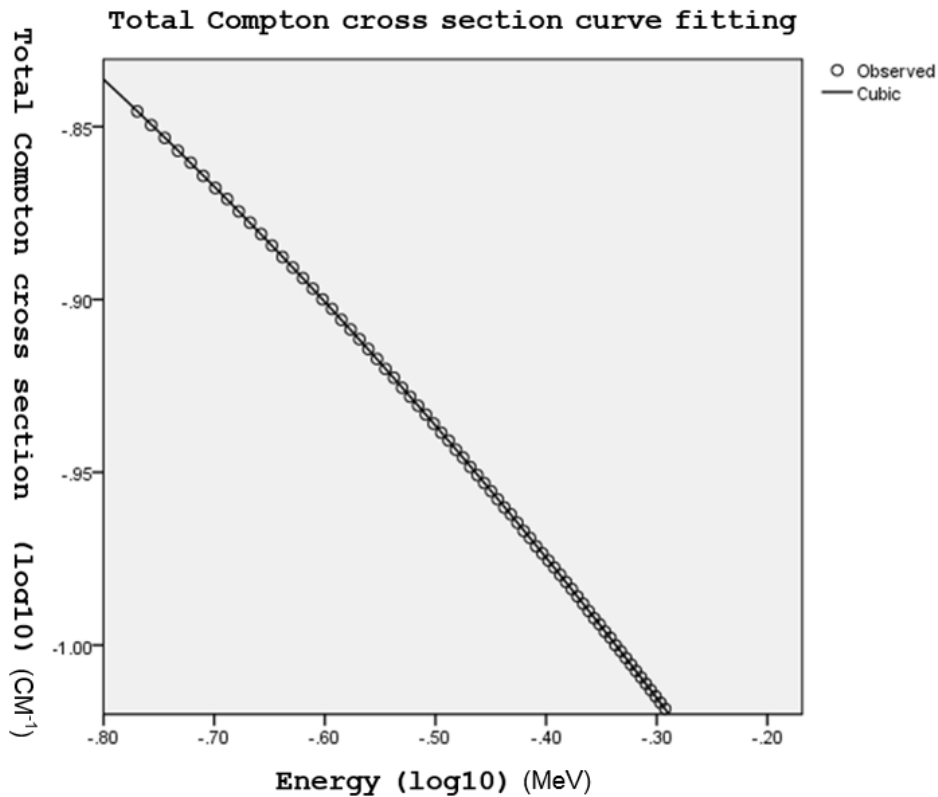


Figure 2-7. The curve fitting of the total Compton cross-section per unit mass. The cubic line is the fitting curve while the dots are observed data from XCOM.

To fit the curve, XCOM suggests that a log-log cubic fit approximates the total Compton cross-section per unit mass as a function of the energy. SPSS was used to estimate the curve, and the result of curve fitting can be found in figure 2-7. The corresponding ANOVA analysis is given in Appendix. Table 2-2 shows the coefficients.

Coefficients					
	Unstandardized Coefficients		Standardized Coefficients	t	Sig.
	B	Std. Error	Beta		
ENERGY_LOG10	-.490	.001	-1.337	-624.399	.000
ENERGY_LOG10 ** 2	-.120	.001	-.341	-159.060	.000
(Constant)	-1.152	.000		-5986.252	.000

Table 2-2. The coefficients of the curve of the total Compton cross-sections per unit mass. Note that the cubic term is excluded through calculation.

Therefore, the expression of the total Compton cross-section per unit mass can be derived as:

$$\log_{10} \frac{\sigma^{kN}}{\rho} = -1.152 - 0.490E_{log} - 0.120E_{log}^2 \quad (2-30)$$

where  $E_{log} = \log_{10} E$ . The total Compton cross-section is equal to the multiplication of the total Compton cross-section per unit mass and corresponding density of the material.

### 2.2.3 Model of Dual-Scattered Coincidences Trajectories

In previous sections, attenuation correction has been discussed. Equation (2-25) gives the expression of attenuation factor when using the GDS-MLEM algorithm in the form of

$Att_{AB,IJ} = e^{-(\int_A^I \mu_1 dl + \int_I^J \mu_0 dl + \int_J^B \mu_2 dl)}$ . However, a realistic PET system cannot determine the positions of scattering events, as shown by points  $I$  and  $J$  in figure 2-1. Therefore, a model to calculate the average length that this pair of dual-scattered coincidence passes through will be introduced in this section. Due to the limited information given by PET systems, some assumptions had to be made in the building of the model.

Figure 2-8 (a) shows a pair of dual-scattered photons measured by detectors  $A$  and  $B$ . The TCAs are plotted (red dotted line) based the sum of the scattering angles. A coefficient  $\alpha$  was used to define different triangles  $\Delta ASB$  inside the TCAs in which figure 2-8 (b) and (c) are one of them. Since the scattering angle  $\theta_1$  and  $\theta_2$  of each scattered photon was known, all possible trajectories of this pair of coincidence before being scattered must be in the same direction, which are described by red dot lines inside triangles. Every point on those trajectories can be the potential annihilation source (purple point) so that the total trajectory for this particular dual-scattered pair is described by  $\overline{ACDB}$ . If  $\theta_1 \geq \theta_2$ , potential trajectories are limited by the length of  $\overline{AS}$  as shown in figure 2-8 (b), whereas, figure 2-8 (c) shows the case of  $\theta_1 < \theta_2$ .

The distance ( $\overline{L}$ ) between detectors  $A$  and  $B$  can be read from the geometry of the PET system. By using “The Law of Sines”, the correlation between  $\overline{L}$ ,  $\overline{AS}$  and  $\overline{BS}$  can be obtained:

$$\frac{\overline{L}}{\sin \theta} = \frac{\overline{AS}}{\sin(\theta - \alpha)} = \frac{\overline{BS}}{\sin \alpha} \quad (2-31)$$

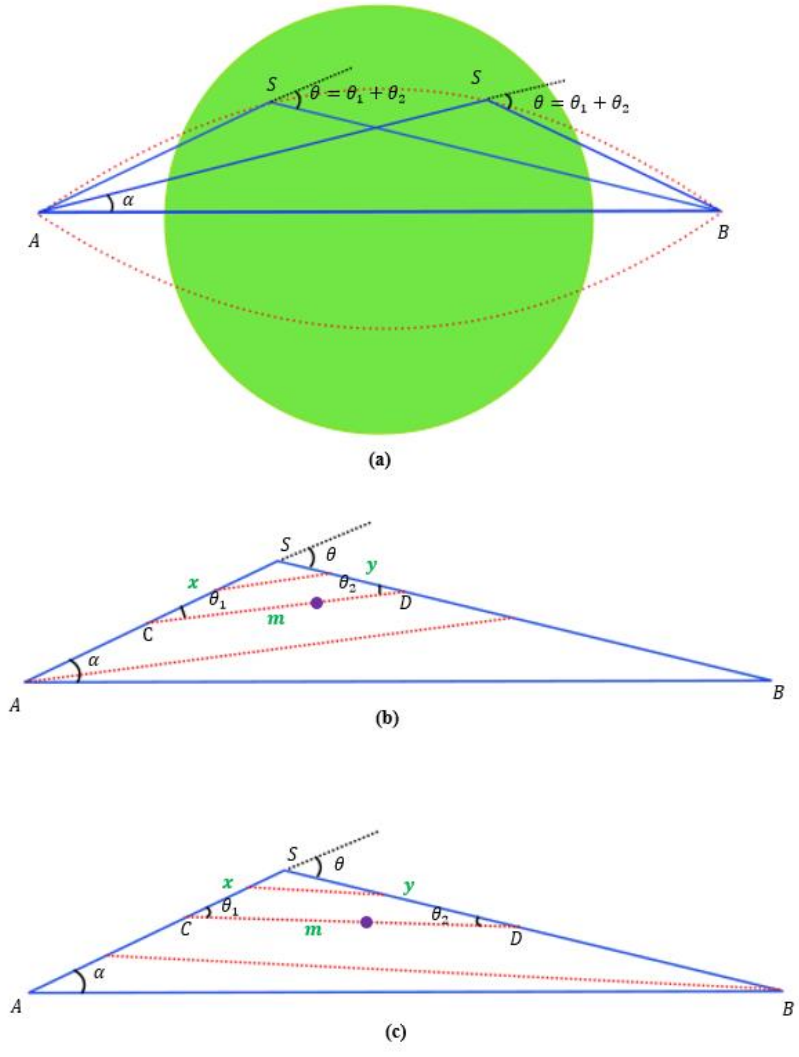


Figure 2-8. The schematic drawing of calculating the trajectory that a dual-scattered coincidence pair travels through. (a) Each triangle inside the TCAs is determined by  $\alpha$ . (b) and (c) show the trajectory  $\overline{ACDB}$  for a given triangle where (b) is the case of  $\theta_1 \geq \theta_2$  and (c) represents the situation of  $\theta_1 < \theta_2$ .

Let  $\overline{CD} = m$ ,  $\overline{SC} = x$ ,  $\overline{SD} = y$ . If coefficients  $\alpha$  and  $m$  are fixed, the trajectory  $\overline{ACDB}$  can be uniquely determined. Therefore, the attenuation along this particular trajectory  $\overline{ACDB}$  can be written as:

$$Att_{\alpha,m} = e^{-[\mu_1(\overline{AS}-x)+\mu_0(m)+\mu_2(\overline{BS}-y)]} \quad (2-32)$$

where  $\mu_0$  is the linear attenuation coefficient for a 511 keV photon,  $\mu_1$  and  $\mu_2$  are linear attenuation coefficients for scattered photons with the scattering angle being equal to  $\theta_1$  and  $\theta_2$ , respectively.

Similarly, while employing “The Law of Sines”, the correlation between  $m$ ,  $x$  and  $y$  is:

$$\frac{m}{\sin \theta} = \frac{x}{\sin \theta_2} = \frac{y}{\sin \theta_1} \quad (2-33)$$

Let  $f(\alpha, m) = \mu_1(\overline{AS} - x) + \mu_0(m) + \mu_2(\overline{BS} - y)$ . Combing equations (2-31) to (2-33), the attenuation is given by:

$$\begin{aligned} Att_{\alpha,m} &= \exp(-f(\alpha, m)) \\ &= \exp\left\{-\left[m \cdot \left(\mu_0 - \frac{\mu_1 \sin \theta_2 + \mu_2 \sin \theta_1}{\sin \theta}\right) + \frac{\mu_1 \overline{L} \sin(\theta - \alpha) + \mu_2 \overline{L} \sin \alpha}{\sin \theta}\right]\right\} \end{aligned} \quad (2-34)$$

Note that the range of  $m$  is different for cases of  $\theta_1 \geq \theta_2$  and  $\theta_1 < \theta_2$ .  $m \in (0, m_{limit})$  where the upper limit for the two cases is given by:

$$\begin{aligned} m_{limit} &= \frac{\overline{L} \sin(\theta - \alpha)}{\sin \theta_2} \quad \text{for } \theta_1 \geq \theta_2 \\ m_{limit} &= \frac{\overline{L} \sin \alpha}{\sin \theta_1} \quad \text{for } \theta_1 < \theta_2 \end{aligned} \quad (2-35)$$

The only two variables in equation (2-34) are  $\alpha$  and  $m$ . To achieve an average calculation,

the first weighting function  $w_1(m)$  will be introduced.  $w_1(m)$  is able to calculate  $\overline{f(\alpha)}$ , which is the averaged result accounting for all possible trajectories inside the triangle defined by the coefficient  $\alpha$ . As previously discussed, every point on  $\overline{CD}$  is a potential annihilation position for a fixed pair of  $(\alpha, m)$ . Thus, the definition of the first weighting function is  $w_1(m) = m$ , which gives more weight for  $\overline{CD}$  with a longer length. So the calculation of  $\overline{f(\alpha)}$  can be given by:

$$\begin{aligned}\overline{f(\alpha)} &= \frac{\int_0^{m_{limit}} f(\alpha, m) \cdot w_1(m) dm}{\int_0^{m_{limit}} w_1(m) dm} \\ &= \frac{2}{3} m_{limit} \left( \mu_0 - \frac{\mu_1 \sin \theta_2 + \mu_2 \sin \theta_1}{\sin \theta} \right) + \frac{\mu_1 \bar{L} \sin(\theta - \alpha) + \mu_2 \bar{L} \sin \alpha}{\sin \theta}\end{aligned}\tag{2-36}$$

To obtain the final average attenuation factor  $\bar{f}$ , another weighting function  $w_2(\alpha)$  will be introduced. It calculates the area of each triangle, which indicates the probability of the annihilation process occurring within the triangle. In other words, if a triangle, given by coefficient  $\alpha$ , has a greater area, it should be given more weight since inside the triangle there is higher probability of a positron-electron annihilation event. Equation (2-37) gives the expression of  $w_2(\alpha)$ :

$$w_2(\alpha) = \frac{1}{2} \cdot \bar{L} \cdot H = \frac{1}{2} \cdot \bar{L} \cdot \frac{\bar{L} \sin(\theta - \alpha) \sin \alpha}{\sin \theta}\tag{2-37}$$

The range of  $\alpha$  is  $\alpha \in (0, \theta)$  so the final average attenuation  $\bar{f}$  can be derived as:

$$\bar{f} = \frac{\int_0^\theta \overline{f(\alpha)} \cdot w_2(\alpha) d\alpha}{\int_0^\theta w_2(\alpha) d\alpha} = \frac{\bar{L}}{B} \cdot \left[ \frac{A \cdot C}{\sin \theta_1} + \frac{A \cdot D}{\sin \theta_2} + \frac{(\mu_1 + \mu_2) \cdot E}{\sin \theta} \right] \quad (2-38)$$

in which  $A$ ,  $B$ ,  $C$ ,  $D$ , and  $E$  are symbols listed in table 2-3.

Symbols	Expressions
<b>A</b>	$A = \frac{2}{3} \left( \mu_0 - \frac{\mu_1 \sin \theta_2 + \mu_2 \sin \theta_1}{\sin \theta} \right)$
<b>B</b>	$B = \frac{1}{2} (\sin \theta - \theta \cos \theta)$
<b>C</b>	$C = \frac{1}{3} \left[ \sin^3 \theta_1 \sin \theta - 4 \sin^4 \frac{\theta_1}{2} (\cos \theta_1 + 2) \cos \theta \right]$
<b>D</b>	$D = \frac{1}{12} [3 \cos(\theta_1 - 2\theta) - \cos(3\theta_1 - 2\theta) + 6 \cos \theta_1 - 8 \cos \theta]$
<b>E</b>	$E = \frac{4}{3} \sin^4 \frac{\theta}{2}$

Table 2-3. The expression of each symbol in equation (2-38).

Since the linear attenuation coefficient can be substituted by the Compton cross-section (see equation (1-22) in section 1.1.2.4),  $\mu_1$  and  $\mu_2$  in equation (2-38) can be obtained using equation (2-29) and (2-30). Thus, the attenuation correction for a particular pair of dual-scattered photons defined by fixed parameters  $(\bar{L}, \theta_1, \theta_2)$  can be calculated. Figure 2-9 is the flow chart of how the GDS-MLEM algorithm works. It starts with a

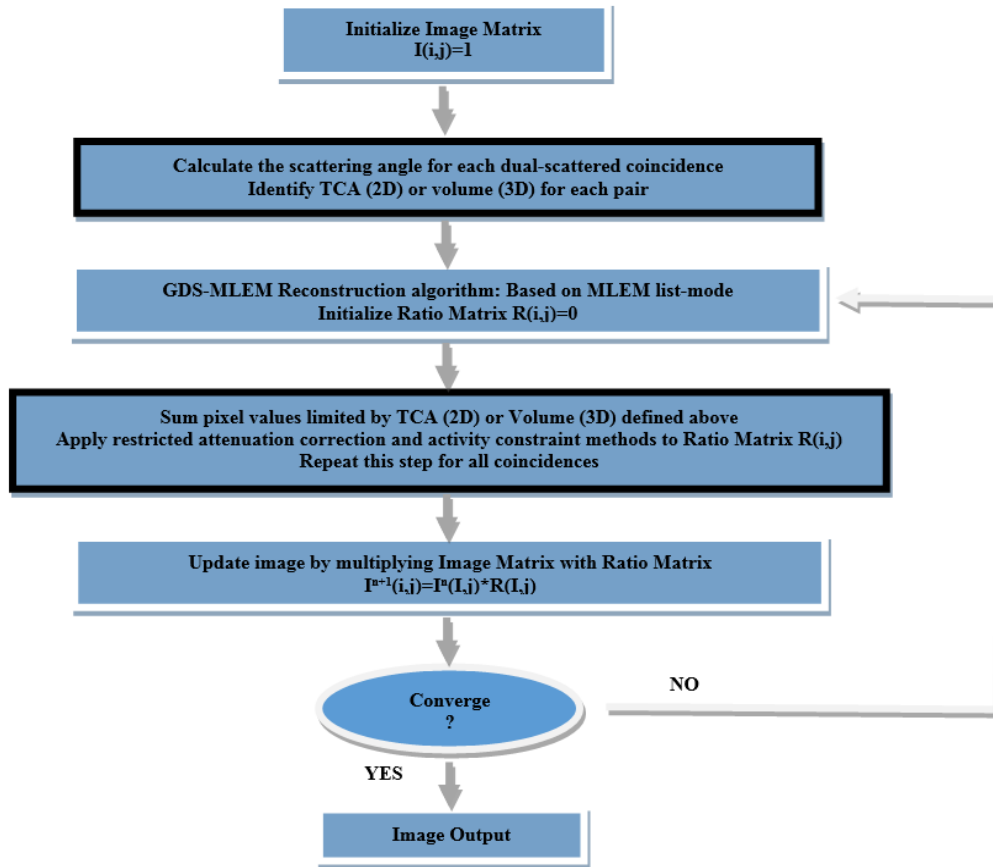


Figure 2-9. The flow chart of implementing the GDS-MLEM algorithm.

uniformly distributed image  $I(i, j) = 1$  and is followed by calculating the ratio matrix  $R(i, j)$  for each coincidence. The image is updated by multiplying the ratio matrix with the image matrix until reaching convergence or a fixed number of iterations.

## 2.3 Simulations using the GATE platform

The feasibility of employing the GDS-MLEM algorithm to reconstruct the activity distribution using higher order scattered coincidences was evaluated qualitatively and quantitatively with simulated data and phantoms. This section provides details on the

simulations performed using Geant4 Application for Emission Tomography (GATE) and subsequent evaluation procedures.

### **2.3.1 Data and PET System Simulations with GATE**

To investigate the possibility of using higher order scattered coincidences to reconstruct the 2D PET activity, data were generated with the MC code GATE and saved in a .dat format. A MATLAB code was used to extract essential information for reconstruction. Since this study is a proof-of-concept, an ideal energy resolution of 0.1% full width at half maximum (FWHM) at 511 keV was used. The energy window was set to 255-512 keV, in which scattered photons with scattering angle greater than  $90^\circ$  were excluded. Note that the true, single scattered, dual scattered and multiple scattered coincidences were selected and differentiated from random events. The effect of positron range was removed by setting the radioactive material to emit back-to-back 511 keV gamma rays directly.

The PET system was modeled after a Siemens microPET Focus 220 scanner. It consists of 4 rings of 42 detectors per ring, with 260 mm diameter and 76 mm axial length. The detector modules have crystal arrays of  $12 \times 12$  LSO ( $1.5 \times 1.5 \times 10$ -mm deep). This configuration provides a transaxial FOV of 242 mm and an axial FOV of 76 mm.

### **2.3.2 Phantom Design in GATE**

To analyze the behavior of the proposed algorithm, a simplified Deluxe Jaszczak phantom [48, 49] was designed. As shown in Figure 2-10, this cylindrical water phantom had a radius of 75 mm and contained four hot disks (with radii of 6 mm, 6 mm, 10 mm and 14 mm) and two cold disks (with radii of 8 mm and 18 mm). The hot-to-background ratio was set to 4, 6, 8 and 10, respectively.

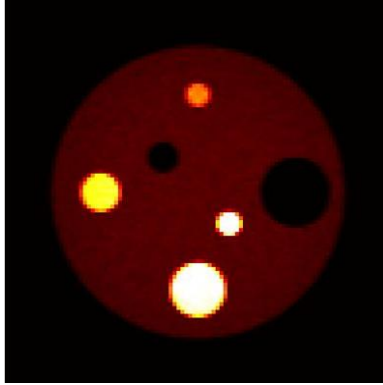


Figure 2-10. A simplified Deluxe Jaszczak water-filled phantom. The four yellow circles were hot disks with radii of 6 mm, 6 mm, 10 mm and 14 mm, respectively. The two black circles were cold disks with radii of 8 mm and 18 mm. The hot-to-background ratio was set to 4, 6, 8 and 10, respectively.

## 2.4 Statistical Analysis for different Reconstructions

In this work, all images were reconstructed within a  $99 \times 99$  image matrix, with each pixel of  $2 \times 2 \text{ mm}^2$  size. The noise was quantified using the relative standard deviation (RSD) of a 16 mm radius circular region of interest (ROI) positioned in the center of the phantom. The contrast recovery coefficient (CRC) was calculated using the ratio of the mean value of the disk to its local background activity. The biggest hot disk was used to evaluate the CRC for the hot region where the mean value of its activity was calculated using an inside circular ROI with a radius of 13 mm. An annular ROI with a 29 mm outer radius and a 15 mm inner radius was used to obtain the mean activity value of the local background. Therefore, the contrast recovery coefficient for hot regions ( $CRC_{hot}$ ) was defined as:

$$CRC_{hot} = \frac{\frac{H}{B} - 1}{S - 1} \quad (2-39)$$

where  $H$  is the average activity value within the circular ROI in the biggest hot disk while  $B$  is the mean activity value in the annulus ROI around the disk.  $S$  is the default value of the hot-to-background ratio for this hot disk.

Similarly, the biggest cold disk was used to evaluate the CRC for the cold region. The average value of the activity of this disk was calculated using an inside circular ROI with a radius of 17 mm. An annular ROI with a 37 mm outer radius and a 19 mm inner radius was used to obtain the mean activity value of the local background. Therefore, the contrast recovery coefficient for cold regions ( $CRC_{cold}$ ) can be derived as:

$$CRC_{cold} = 1 - \frac{C}{B} \quad (2-40)$$

in which  $C$  represents the average activity value of the ROI in the cold disk.

To evaluate the performance of the GDS-MLEM algorithm, traditional LOR-MLEM method and the single-scatter based generalized-scattered MLEM (GS-MLEM) algorithm [50] were also used to reconstruct images using the same data. Table 2-4 shows the applicable data for each algorithm.

## 2.4.1 Activity Distribution Reconstruction using Multiple Scattered Coincidences

In section 2.1.2, it has been shown that multiple scattered coincidences cannot be strictly

limited to an area. However, different algorithms are still useful to address the potential annihilation source with a small fraction of error. Therefore, the feasibility of activity reconstruction using multiple scattered coincidences was tested for three different algorithms where the criterion lay in the detection of hot disks in the phantom. To achieve this comparison, 500,000 multiple scattered coincidences were selected from the GATE simulation under an ideal energy resolution assumption. Attenuation corrections were not applied in this case.

Coincidence Type	LOR-MLEM	GS-MLEM	GDS-MLEM
True	✓	✓	✓
Single scattered		✓	✓
Dual scattered			✓
Multiple scattered			

Table 2-4. Applicable types of data of different algorithms.

## 2.4.2 Reconstruction of Activity Distribution without Attenuation

### Correction

Since the feasibility of using multiple scattered events have been addressed in the last section, a more realistic dataset consisting of true, single scattered and higher order scattered coincidences was used to compare the performance among different algorithms.

With a scatter fraction of 40% and an ideal energy resolution, 100,000 mixed coincidences were selected from the GATE simulation. Images were reconstructed without attenuation correction and the constraint of the phantom outline and were evaluated using CRC and RSD.

### **2.4.3 Activity Distribution Reconstruction using Restricted Attenuation**

#### **Correction**

The proposed restricted attenuation correction and phantom outline constraint were added into the reconstruction of activity. A reference image, which was generated using the LOR-MLEM algorithm and a typical attenuation correction, was reconstructed to assess the benefit of this approach. By using the same data that has a 40% scatter fraction with an ideal energy resolution, another image was obtained employing the GDS-MLEM algorithm and the restricted attenuation correction model. The evaluation was also made on the comparison of CRC and RSD.

### **2.4.4 Reconstruction of Activity Distribution with Non-Ideal Energy**

#### **Resolution**

In the previous reconstructions, all simulations were performed with an ideal energy resolution of 0.1% at 511 keV. However, the energy resolution of the detector is still above 5% nowadays. Some advanced detectors achieve an energy resolution of 12% while for clinical PET system, this figure is around 20% [51-53]. Therefore, these three non-ideal energy resolutions were considered in this section.

The simulated data were blurred based on the value of the energy resolution. If the energy

resolution of detector ( $RS_{511}$ ) is pre-determined, the energy resolution for photons with an energy  $E$  (in units of keV) can be given by:

$$RS_E = RS_{511} \cdot \sqrt{0.511/E} \quad (2-41)$$

The energy distribution of photons follows the Gaussian distribution if photons are measured by a detector with a non-ideal energy resolution. Thus, the relationship between the energy resolution  $RS_E$  and the FWHM of a Gaussian distribution with a photopeak at  $E$  is:

$$RS_E = \frac{FWHM}{E} \quad (2-42)$$

The standard deviation ( $\sigma$ ) and FWHM for a Gaussian distribution is given by:

$$FWHM = 2\sqrt{2 \ln 2} \cdot \sigma \quad (2-43)$$

Combine equation from (2-41) to (2-43), the energy of photon after blurring ( $E'$ ) obeys a Gaussian distribution and can be written as:

$$E' \sim N(\mu, \sigma^2) \quad (2-44)$$

in which  $\mu = E$  and  $\sigma = \frac{RS_{511} \cdot \sqrt{0.511E}}{2\sqrt{2 \ln 2}}$ . In MATLAB, the simulated data can be blurred depending on pre-set  $RS_{511}$  before reconstructing activity distribution. Images were then reconstructed upon different algorithms using blurred data and were further evaluated with CRC and RSD.

## **3. Result**

In this chapter, the proposed GDS-MLEM reconstruction algorithm and the restricted attenuation correction model will be assessed. Images were generated using simulated data where three different reconstruction algorithms including LOR-MLEM, GS-MLEM and GDS-MLEM were simultaneously used. To compare the strengths and weakness of each algorithm, conditions such as pure multiple coincidences, random-free coincidences with an ideal energy resolution and data simulated under different non-ideal energy resolutions, were used.

### **3.1 Reconstruction of Activity using Only Multiple Scattered Coincidences**

As indicated in table 2-4, each algorithm has its scope of application, and there is none specifically designed for handling multiple scattered coincidences. To evaluate the feasibility of using these higher order scattered coincidences, different algorithms were initially tested on data consisting of only multiple scattered coincidences.

The LOR-MLEM algorithm is the standard reconstruction method for clinical use. It assumes that each detected coincidence is a true event, and locates the annihilation position along the line connected by two detectors. The GS-MLEM approach is designed for employing single scattered photons. It is based on the assumption that each measured coincidence consists of a true photon and a scattered photon undergoing only one Compton scattering event where the scattering event occurs on the TCAs defined by the scattering angle.

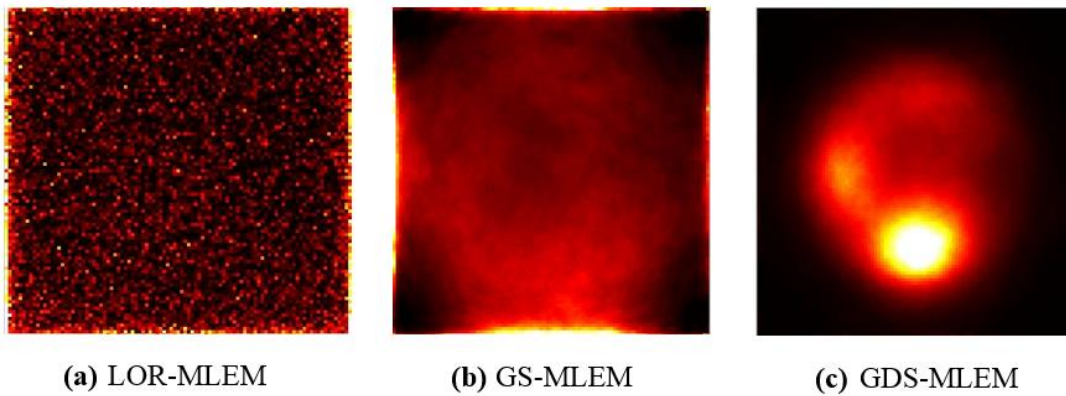


Figure 3-1. Activity reconstructions of the water-filled cylinder phantom using multiple scattered coincidences only. The three different algorithms, from left to right, were traditional LOR-MLEM, single-based GS-MLEM and the proposed GDS-MLEM algorithm, respectively.

Figure 3-1 shows the images reconstructed using three algorithms when 500,000 multiple scattered coincidences were used under the circumstance of 0.1% energy resolution. Without attenuation corrections applied, all images were reconstructed in a  $99 \times 99$  image matrix using the list-mode format data. The LOR-MLEM algorithm was incapable of detecting hot regions and the resulting image, displayed in figure 3-1 (a), contained only noise. Figure 3-1 (b) was generated using the GS-MLEM approach, and the image had less noise and produced a blurry outline of the phantom, but was still incapable of identifying the hot regions. Compared with the simulated phantom (figure 2-10), images reconstructed with the proposed GDS-MLEM algorithm (figure 3-1 (c)) were able to identify the two largest hot regions on the bottom and left of the phantom. Moreover, there was an area of cold region that was also roughly perceived.

Because the history of each coincidence was available from the simulation output, the

annihilation position of each multiple scattered coincidence was known. This allowed us to identify how many annihilation positions were successfully identified. If a real source position lay on the line or in the area specified by the corresponding algorithm, it was counted as a valid reconstruction. Table 3-1 lists the rate of valid reconstruction of each algorithm, which indicates that the GDS-MLEM algorithm located 98.2% annihilation positions; whereas, the success rate of localization using the GS-MLEM method was 69.8%. In contrast, only 14.7% source positions were determined correctly when the traditional LOR-MLEM algorithm was implemented.

<b>Reconstruction method</b>	<b>Valid reconstruction rate</b>
LOR-MLEM	14.7%
GS-MLEM	69.8%
GDS-MLEM	98.2%

Table 3-1. Statistical results for valid reconstruction rate of each algorithm.

It is important to note that images shown in figure 3-1 were only based on multiple scattered coincidences, and thus should not be expected to have the same quality level as images reconstructed with true coincidences. These images, instead of for quantitative and qualitative analysis, were merely used for investigating the potential of the proposed algorithm being applied on multiple scattered coincidences.

### **3.2 Images Reconstructed without Attenuation Correction**

In this section, a more realistic dataset consisting of true, single scattered and multiple

scattered coincidences, was simulated. Under the condition of ideal energy resolution, 100,000 coincidences were selected in an energy window between 255 keV to 512 keV. The scatter fraction was 40%, in which 35% of them were multiple scattered events. These numbers were obtained by checking the histories of all simulated data, and thus represented the actual proportion of different types of coincidences in this particular simulation.

The first row of Figure 3-2 displays the images reconstructed using different algorithms without attenuation corrections and outline constraints of the phantom. The second row exhibits the image profiles passing through the central point of the images in vertical and

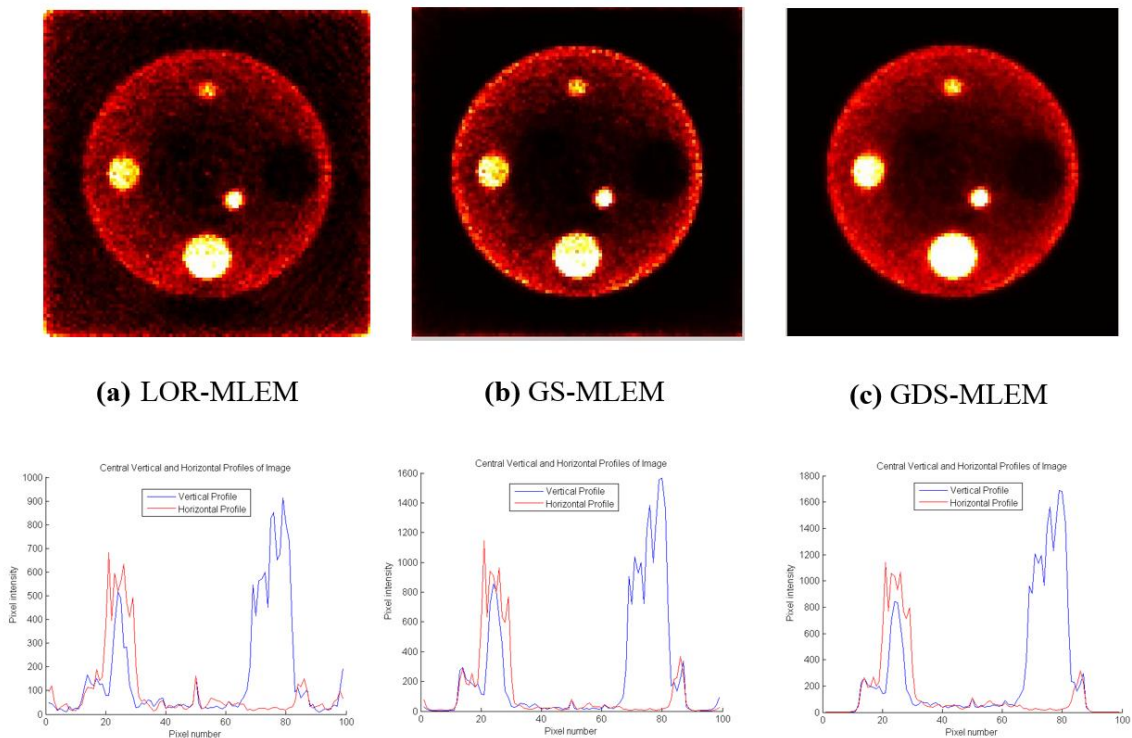


Figure 3-2. Reconstructions of activity distributions using different algorithms without attenuation corrections and the outline of the phantom. The first row shows the reconstructed images and the second row gives the corresponding image profiles in vertical and horizontal directions along the lines going cross the center of the images.

horizontal directions. Figure 3-2 (a) was reconstructed using the typical LOR-MLEM algorithm. An attenuation problem was observed in this image as the central area was darker (which was supposed to have the same activity level) than the edge of the phantom. Also, there was some noise detected outside the phantom. The GS-MLEM algorithm was employed to generate Figure 3-2 (b). In contrast, the issue of attenuation still existed, but the image had less noise outside the phantom. Some bright hot spots could be observed at the edge of the phantom. This inequality between the middle and the edge of the phantom was also perceived in the image profile where two peaks appeared on both sides. Figure 3-2 (c) was obtained with the proposed GDS-MLEM algorithm. Compared with the previous two images, it achieved the smoothest activity distribution and the least noise. The quantitative analysis of each image will be discussed below.

Figure 3-3 shows the CRC vs. RSD curves of each algorithm in hot and cold regions. For each reconstruction algorithm, the image was updated 100 times through an iteration procedure so that the criteria for determining the best quality image must be clarified. In this work, the coordinate (1,0) (green dot in figure 3-3) represents the ideal image quality, which achieves a perfect hot-background (or cold-background) ratio, and also reproduces the activity distribution without noise. Therefore, the distance between the green dot and each point on the curve was used to evaluate the image quality after every iteration. The red, blue and black dots were corresponding to the best image quality achieved using LOR-MLEM, GS-MLEM, and GDS-MLEM algorithms, respectively. Images in figure 3-2 were selected based on these points in figure 3-3 (a).



When the points for the cold region were evaluated, the curve of the GDS-MLEM algorithm had a 1.6%-7.2% greater CRC than the curve calculated using the GS-MLEM method and was 4.3%-14.6% greater than the curve obtained by LOR-MLEM. The noise at evaluation points was 12.9%-35.4% less than the figure counted using GS-MLEM and decreased by 23.7%-45.1% compared with that achieved with the LOR-MLEM.

### **3.3 Images Reconstructed with Restricted Attenuation Correction**

Three parameters are needed to calculate the restricted attenuation correction; this includes the total Compton cross-section, the ratio of the restricted Compton cross-section to the total Compton cross-section, and the length of the trajectory that a pair of dual-scattered coincidence travels. Each component has been discussed in section 2.2, and the calculation results are given below.

#### **3.3.1 Estimation of Total Compton Cross-Section**

The density of water ( $1 \text{ g/cm}^3$ ) was used to calculate the total Compton cross-section. Figure 3-4 shows the estimated and table-checked values of the total Compton cross-section, where the blue line was drawn using equation (2-30) while the red dots were located based on the data from XCOM. Energies ranging from 171 keV to 511 keV, with a gap of 5 keV, were chosen. Although the proposed equation was not precise enough to predict the value of the Compton cross-section for the entire energy range, it showed good agreement, with an average estimation error of 0.12%, at energies from 170 keV to 512 keV. The appendix lists this data.

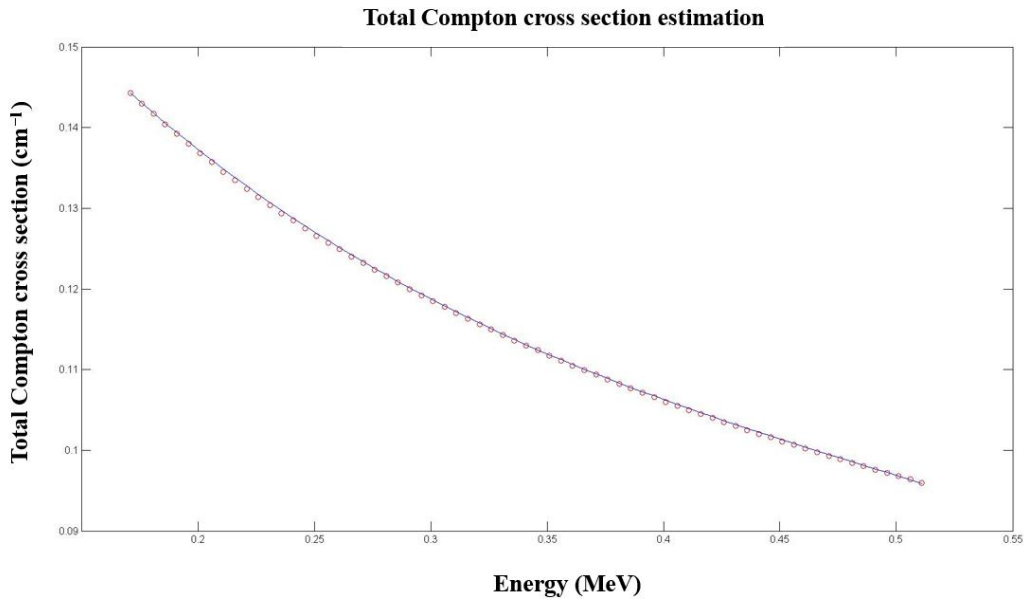


Figure 3-4. Total Compton cross-section prediction. The line was calculated using equation (2-30) and the dots were obtained from XCOM database.

### 3.3.2 Ratio of the Restricted Compton Cross-Section to the Total

#### Compton Cross-Section

Equation (2-29) provides the expression of the ratio between the restricted Compton cross-section and the total Compton cross-section. Figure 3-5 depicts several lines where the shape of each line varied based on different initial photon energies. From left to right, when the initial energy of the photon decreased from 4.09 MeV to 0.0511 MeV, the ratio of the minimum photon energy (after one back-scattering event) to the initial photon energy increased. For example, equation (1-10) shows that this ratio is equal to  $\frac{1}{3}$  for photons with an initial energy of 511 keV, where this number corresponded to the intersection point between the X axis and the black line. As the ratio approached 1, the restricted energy

threshold increased, which resulted in the exclusion of additional scattered coincidences from the reconstruction. Therefore, the ratio approached 1 as well, reverting back to the total Compton cross-section for the calculation of attenuation correction.

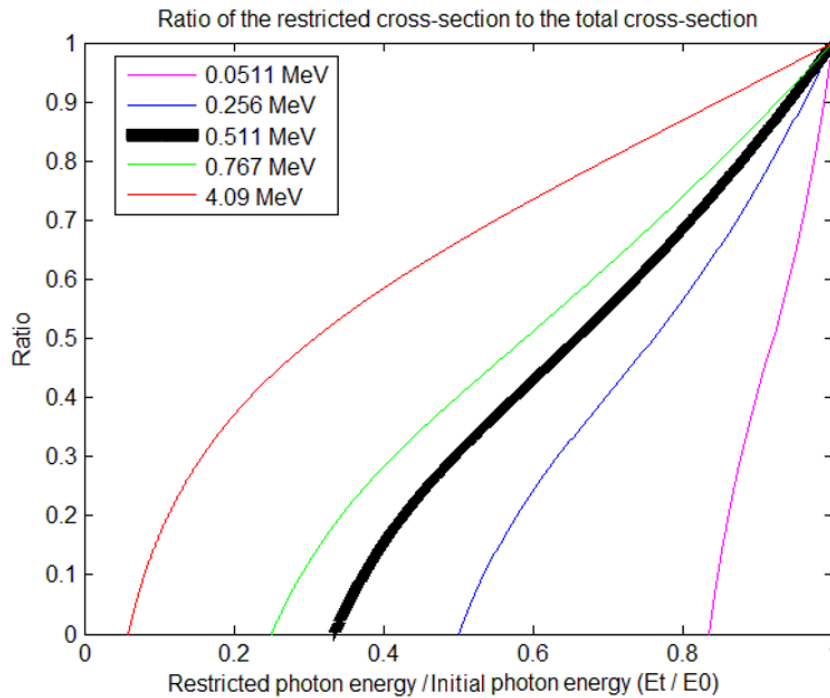


Figure 3-5. The ratio of the restricted cross-section to the total cross-section depended on the initial photon energy ( $E_0$ ) and restricted photon energy ( $E_t$ ). It shows how the ratio changed with  $E_0$  varying from 4.09 MeV (left) to 0.0511 MeV (right).

### 3.3.3 Calculation of Restricted Attenuation Correction

Traditionally, the attenuation correction for the LOR-MLEM algorithm uses the multiplication of the detector's distance ( $\bar{L}$ ) and the linear attenuation coefficient of 511 keV photons ( $\mu_0$ ). Equation (2-38) indicates the calculation of restricted attenuation

correction for the GDS-MLEM algorithm. Figure 3-6 shows the ratio of the restricted attenuation correction to the traditional attenuation correction, where the traditional attenuation correction was assumed to be  $\mu_0 \bar{L} = 1$ . Consider the limit of the sum of the scattering angles is  $\frac{\pi}{2}$ , each scattering angle was given a threshold of  $\frac{\pi}{4}$  in this figure. For the use of this approach, however, one of two scattering angles can be greater than  $\frac{\pi}{4}$ , as long as the sum of them is less than  $\frac{\pi}{2}$ . It can be shown that the ratio was equal to 1 when both photons experienced no Compton scattering events. As the sum of the scattering angle

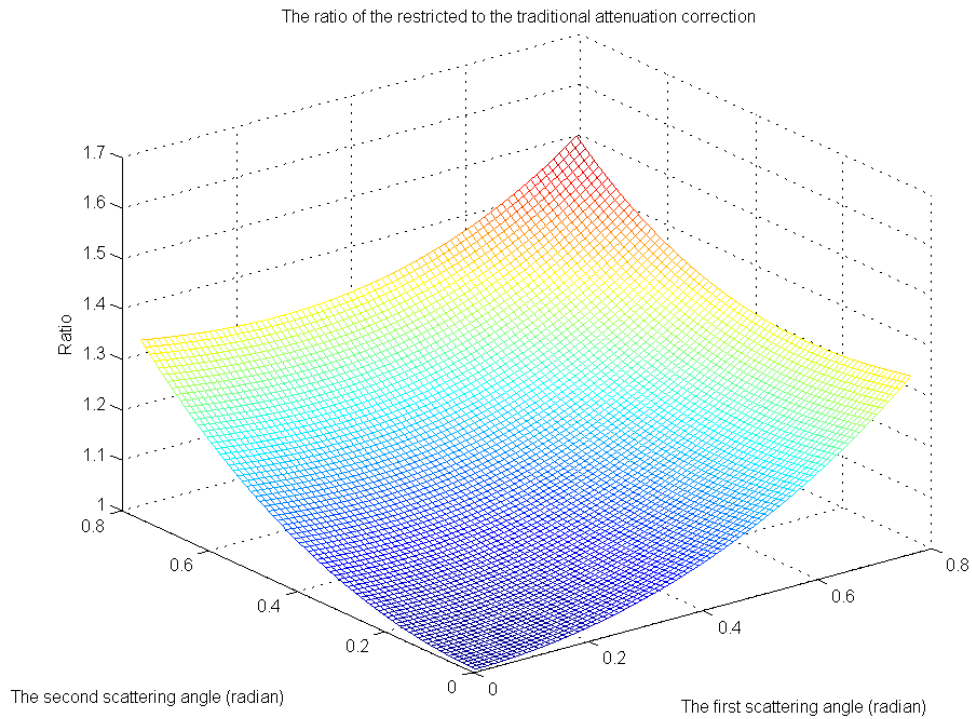


Figure 3-6. The ratio of the restricted attenuation correction to the traditional attenuation correction where the traditional attenuation correction was assumed to be 1. Each scattering angle was given a range of  $(0, \frac{\pi}{4})$ , which limited the total scattering within  $(0, \frac{\pi}{2})$ .

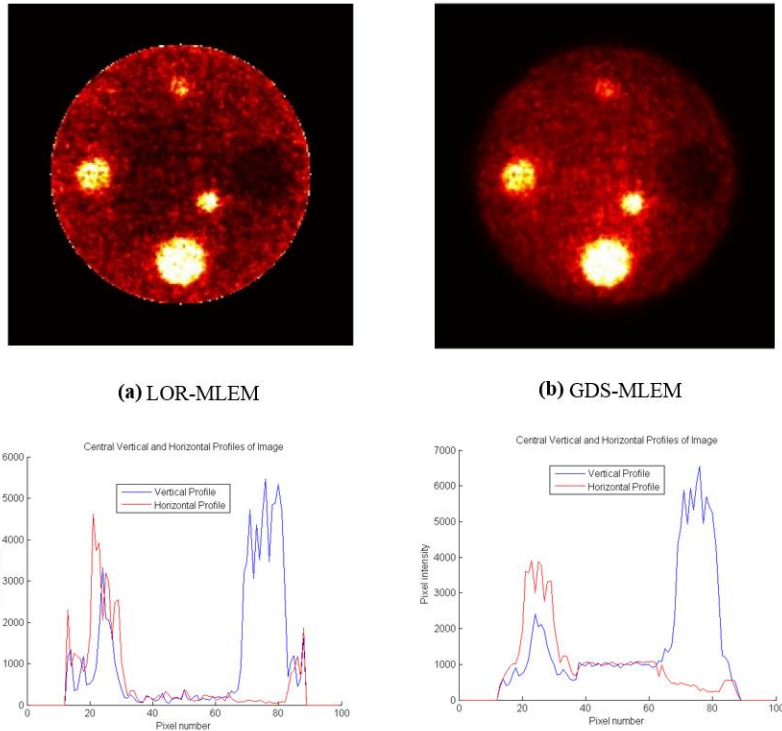


Figure 3-7. Reconstructions of activity distributions using two algorithms with the constraints of phantom's outline. Typical attenuation correction and restricted attenuation correction were separately implemented on LOR-MLEM and GDS-MLEM algorithms. The first row shows the reconstructed images and the second row gives the corresponding image profiles in vertical and horizontal directions along the lines going across the center of the images.

increased, this ratio increased as well.

The images shown in Figure 3-7 were created using different attenuation corrections. Both images were reconstructed using 100,000 coincidences with a scatter fraction of 40%. The outline of the phantom was used to further confine the activity distribution. Figure 3-7 (a) was reconstructed by the LOR-MLEM algorithm with a typical energy window of 350-650 keV, whereas, figure 3-7 (b) was generated using the GDS-MLEM method with a restricted energy threshold of 255 keV. Traditional and restricted attenuation corrections were

applied to two reconstructions, respectively. The second row exhibits the image profiles in vertical and horizontal directions along the lines passing through the center of the images.

In figure 3-7 (a), there are a few bright spots visible at the edge of the phantom, which correspond to the relatively high peaks, displayed on the two sides of the image profile. Compared with the activity of the background at edges, a small darker area was observed in the middle. In addition, it can be shown from the image profile that the activity level in the middle area was close to that of the biggest cold region, which made it difficult to distinguish them. The activity of the background in figure 3-7 (b), by contrast, was distributed more equally. Less noise was observed, and the activity difference in the profile allowed the distinction between the background and the largest cold region. The restricted attenuation correction also partially eliminated the peaks on the two sides in the image profile.

Figure 3-8 shows the CRC vs. RSD curves in hot and cold regions using LOR-MLEM and GDS-MLEM algorithms, respectively. For each reconstruction algorithm, 100 iterations were applied to update images. The red and black dots were corresponding to the best image quality achieved, where the images in figure 3-7 were selected based on the points in figure 3-8 (a). The CRC-RSD curves for images reconstructed using the GDS-MLEM algorithm, whether in the hot or cold region, were always above those generated by the LOR-MLEM algorithm. For a given noise level, by contrast, the GDS-MLEM algorithm achieved a better image with greater CRC in both hot and cold regions. Statistically, the evaluation points on the CRC curve of GDS-MLEM for the hot region were 8.3%-24.4% greater than the CRC curve obtained using the LOR-MLEM algorithm. When the points



The noise increased by 14.2%-33.7%.

### **3.4 Images Reconstructed with Non-Ideal Energy Resolution**

To evaluate the performance of the proposed approach with non-ideal energy resolution, simulations were performed in the same manner as in section 3.3, except that the energy resolution was non-ideal. According to section 2.4.4, data simulated with an ideal energy resolution were blurred, to give an energy resolution of 5%, 12%, and 20%. This represented respectively, the energy resolution of future detectors, recently reported detectors and detectors that have been used in the clinical PET system. Figure 3-9 gives the results of the reconstructions. Compared with the reconstructions with the ideal energy resolution, the non-ideal energy resolution reconstruction had more artifacts, which was expected. Each line shows the images generated using different algorithms with the same energy resolution. From top to bottom, less noise within the phantom and reduced artifacts around the edge were observed. The effect of energy resolution could be demonstrated in each row. For example, the third row demonstrates how the poor energy resolution degraded the image quality while using the GDS-MLEM algorithm. The largest hot region was reconstructed as a circle containing less than 5% energy resolution; although more artifacts were demonstrated with worsening of the energy resolution. When the energy resolution was 20%, the largest hot region was reconstructed with many artifacts around the edge and was no longer shown as a circle. In addition, numerous artifacts around the outline of the phantom and more noise were found in this figure.

Figure 3-10 shows the CRC-RSD curves for hot and cold regions using different algorithms with various non-ideal energy resolutions. The quality of images became worse compared

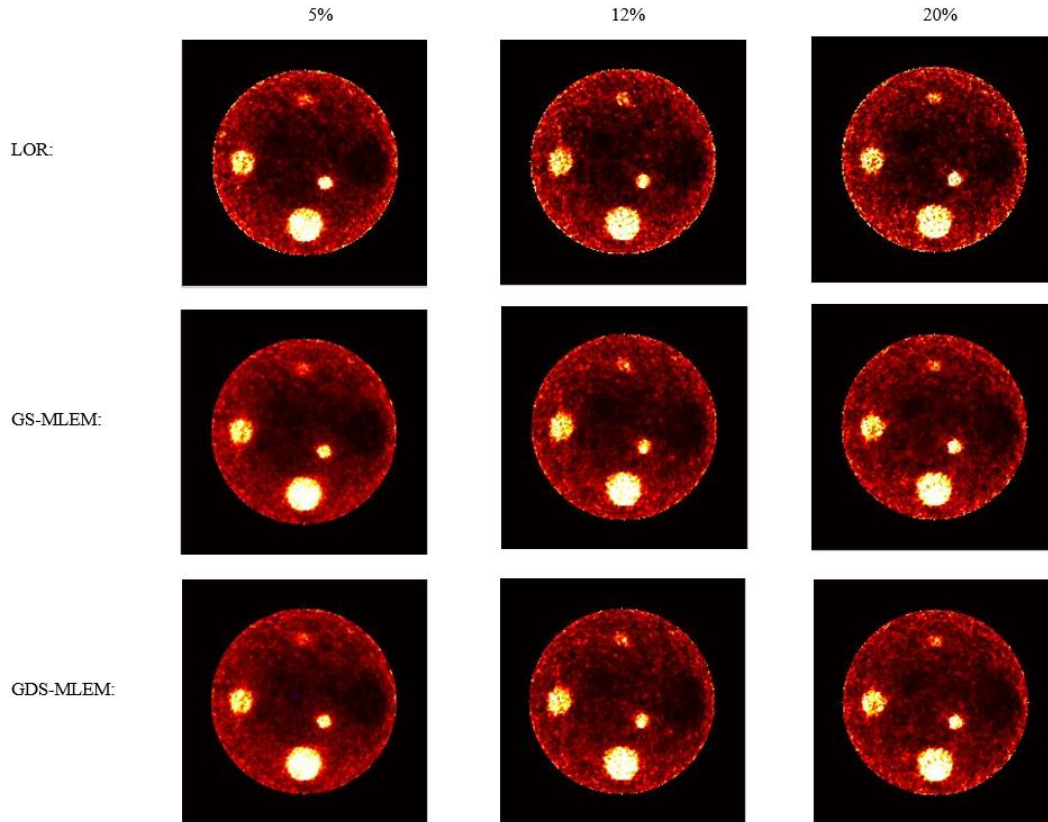


Figure 3-9. Reconstructions of activity distributions using non-ideal energy resolutions. LOR-MLEM, GS-MLEM and GDS-MLEM algorithms were tested simultaneously under the different energy resolutions of 5%, 12% and 20%.

with figure 3-8, which was obtained with an ideal energy resolution. Generally, The CRC curves for both hot and cold regions decreased as the energy resolution became poorer no matter the algorithm used. When the energy resolution varied from 5% to 20%, the RSD reduced when employing GDS-MLEM and GS-MLEM algorithms, but the RSD of LOR-MLEM fluctuated around 2.6-2.8%.

When the energy resolution was equal to 5%, the GS-MLEM method had the highest CRC for both hot and cold regions, followed by the GDS-MLEM and the LOR-MLEM

### Hot Region

### Cold Region

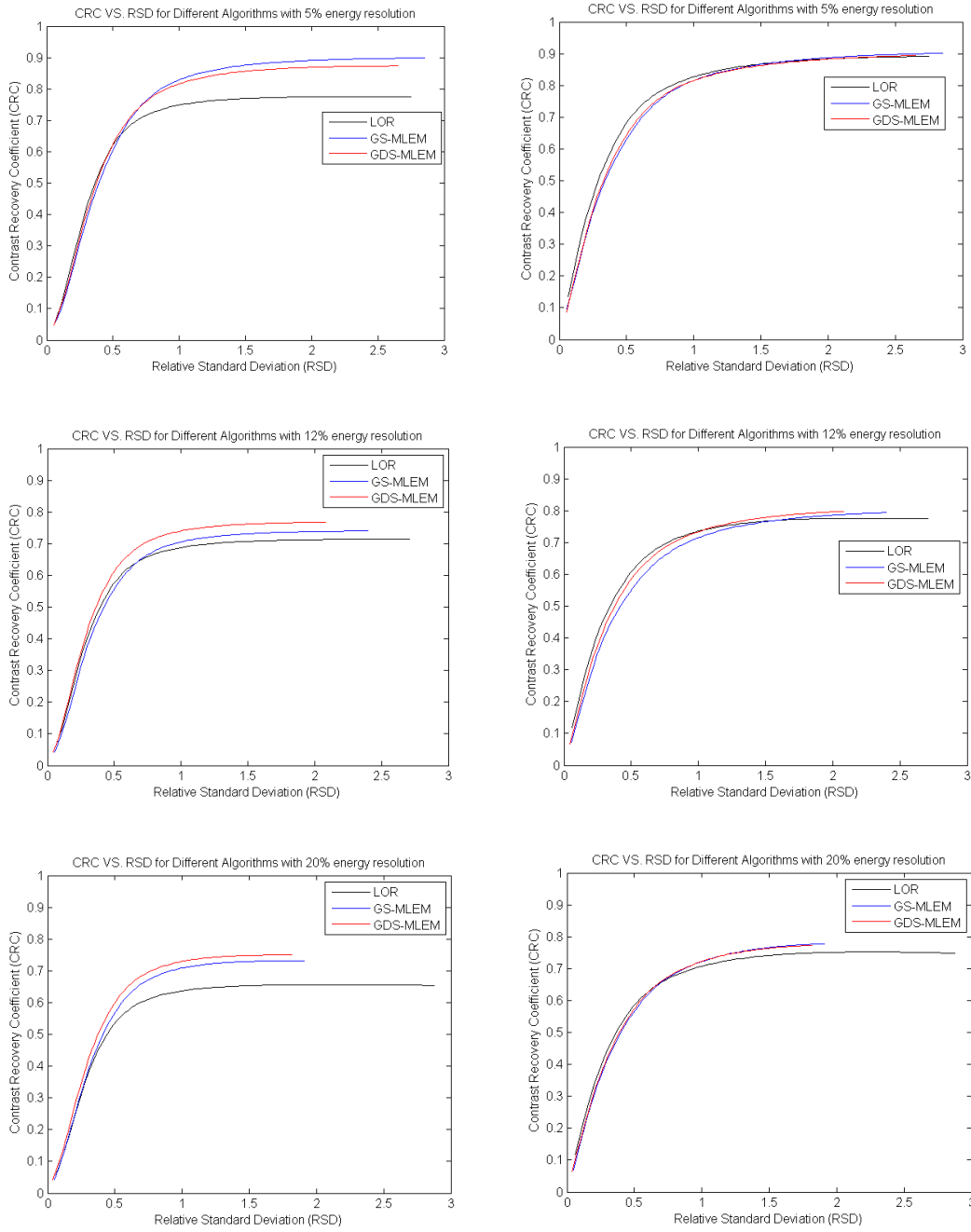


Figure 3-10. The CRC-RSD curves for hot and cold regions using different algorithms with non-ideal energy resolutions.

algorithms. However, the noise of the reconstruction using the GS-MLEM approach was

greatest; whereas the GDS-MLEM method achieved the smallest noise. Statistically, the evaluation points on the CRC curve of GS-MLEM for the hot region was 2.4%-6.5% larger than the images generated using the GDS-MLEM algorithm and was 6.7%-19.2% higher than the corresponding curve obtained by the LOR-MLEM algorithm. When the points for the cold region were evaluated, the curve of the GS-MLEM algorithm had a 0.7%-4.7% greater CRC than the curve calculated using the GDS-MLEM method and was 1.3%-6.6% greater than the curve obtained by the LOR-MLEM approach. The noise at the evaluation points was 2.9%-5.3% higher than the figure counted by the LOR-MLEM method and increased by 4.7%-9.1% compared with that obtained by the GS-MLEM algorithm.

When the energy resolution was set to 12%, images that were generated by GDS-MLEM achieved the greatest CRC in the hot region. The CRC curve using GDS-MLEM in the cold region intersected with the curve of GS-MLEM in the middle of the figure, and provided the greatest value afterward. For the hot region, specifically, the points on the CRC curve of GDS-MLEM were 3.7%-7.4% greater than the images generated using the GS-MLEM algorithm and were 6.7%-14.2% higher than the corresponding curve obtained by the LOR-MLEM algorithm. Regarding the points for the cold region, the curve of the GDS-MLEM algorithm was 4.3%-8.6% greater than the curve calculated using the LOR-MLEM method. The noise at the evaluation points of GDS-MLEM was 4.0%-8.6% less than the figure depicted using GS-MLEM and decreased by 7.7%-15.1% compared with that obtained by the LOR-MLEM method.

The last row shows the CRC-RSD curves while using detectors with 20% energy resolution. The GDS-MLEM algorithm reconstructed the images with the highest CRC for the hot

region, which was 2.0%-4.9% greater than images obtained using GS-MLEM, and 8.1%-21.6% higher than the corresponding CRC generated by the LOR-MLEM algorithm. For the cold region, the CRC curve of GDS-MLEM was close to the one obtained by GS-MLEM with 0.3%-1.5% difference and was greater than the curve of LOR-MLEM by 1.7%-4.1%. The noise at the evaluation points of GDS-MLEM was 1.9%-4.2% less than the points calculated using the GS-MLEM and decreased by 13.9%-51.6% compared with those obtained by the LOR-MLEM algorithm.

## 4. Discussion and conclusion

The GS-MLEM reconstruction algorithm was first developed by our group for 2D non-TOF PET systems based on the assumption that each detected coincidence was a single scattered pair. However, the remaining higher ordered scattered coincidences are neither properly processed using the GS-MLEM algorithm nor extracted from the realistic PET data. The existence of higher order scattered events decreases the image quality, and most importantly, limits the development of the GS-MLEM reconstruction algorithm for clinical use.

In this work, this algorithm was extended to a new GDS-MLEM algorithm that is capable of handling higher order scattered photons. The GDS-MLEM algorithm considered each detected photon pair as a dual-scattered coincidence, in which an annihilation area was defined by the spatial information from the location of the photon detections and the energies of the photons. To identify a more realistic area, the outline of the object was used to confine the annihilation area such that all pixels inside this area were assumed to have the same probability for the positron-electron annihilation event. When dealing with scattered photons, the LOR-MLEM algorithm and the GS-MLEM approach ignore possible annihilation positions due to an inaccurately confined line or area. By contrast, the proposed GDS-MLEM algorithm defines an area which more accurately defines the actual annihilation positions. Even though the annihilation positions of multiple scattered coincidences cannot be strictly determined, the proposed GDS-MLEM has the greatest confidence in locating them. Both LOR-MLEM and GS-MLEM algorithms can be considered as the special cases of GDS-MLEM for reconstruction under the circumstance

of an ideal energy resolution. An attenuation correction method which calculated the attenuation coefficients by restricting the energy range over which the differential Klein-Nishina cross-section was integrated, was proposed. This approach avoids overcorrecting for scattered coincidences by accounting only for scattered photons that were not included in the reconstruction.

In section 3.1, three different reconstruction algorithms were used to test the feasibility of using multiple scattered coincidences in the reconstruction. The results from figure 3-1 have shown that the multiple scattered photons produce only noise in the image generated by the LOR-MLEM algorithm. When the GS-MLEM method was applied, it was difficult to distinguish the hot and cold regions inside the phantom. However, when the GDS-MLEM reconstruction algorithm was implemented, the information of activity distribution could be extracted from multiple scattered events. As discussed in section 2.1.2, there is no way to define an area (smaller than the object) that can completely confine the possible annihilation positions for multiple scattered events. However, table 3-1 has shown that only a small fraction of real annihilation events was inaccurately determined using the GDS-MLEM reconstruction algorithm since small angle scattering with small energy losses are highly probable for photons at energies around 511 keV. Therefore, by including multiple scattered coincidences in the dataset, the quality of the diagnostic image and imaging content can be improved, while reducing the patient dose and radiopharmaceutical cost.

In section 3.2, more realistic PET data consisting of true, single scattered and higher order scattered events were evaluated. As expected, the scattered coincidences could not be accurately handled using LOR-MLEM, and therefore resulted in blurring in figure 3-2 (a).

The reconstruction algorithms of GS-MLEM and GDS-MLEM both showed the ability to process scattered photons, while the latter was able to achieve a better image quality. Images reconstructed using GDS-MLEM had the highest contrast for both hot and cold regions and achieved the lowest noise. These results indicate that the inclusion of scattered coincidences into the GDS-MLEM reconstruction is beneficial to the PET scans under conditions of ideal energy resolution. It improves the image quality by increasing the contrast and reducing the noise and also eliminates the side effects induced by inaccurate scatter corrections. Turning scattered photons from contributing noise to useful data increases the system's sensitivity and lowers the data requirement for an equivalent image quality, all the while reducing the noise, scan time, injected dose and radiation burden. This work may directly benefit the patient by reducing artifacts, providing a more accurate diagnosis, and thereby expanding the role and value of PET.

A restricted attenuation correction model and the outline of the object were implemented on the GDS-MLEM algorithm in section 3.3. Compared with the image in figure 3-2 (c), the improvement of the image quality in figure 3-7 (b) was obtained by taking advantage of the outline of the phantom to confine the possible annihilation positions into a smaller area. In addition, the difference between figure 3-7 (a) and (b) was caused by the effectiveness of GDS-MLEM in handling the scattered coincidence and the restricted attenuation correction, which avoided double counting of the detected scattered coincidences. The revised attenuation correction is based on the choice of the restricted energy threshold, which provides the operator with the flexibility to dynamically select an energy window for the scattered photons. Reducing the restricted energy threshold increases the number of large angle scattered photons, thus decreasing the image noise and

reducing contrast due to blurring. This energy threshold is also used as the upper threshold for the integration of the differential cross-section, ensuring that attenuation corrections are only applied to photons that are scattered into energy below this limit. Therefore, an optimum PET image for a particular patient can be obtained depending on the energy distribution of the scattered photons that are selected.

The computational time of GDS-MLEM is now 2-3 times longer than the use of the conventional LOR-MLEM algorithm since each pair of coincidences needs to be assigned an area, instead of a line, for constraining the potential annihilation positions. In addition, the energy resolution of detectors is of significance when using the GDS-MLEM algorithm. The detected energies of photons are used to define the TCAs, which describe the possible locus of annihilation events, and hence the image quality is sensitive to the energy resolution.

In section 3.4, images were reconstructed under conditions of non-ideal energy resolution to evaluate the performance of different algorithms. It was evident from figure 3-9 that the quality of images degraded as the energy resolution becomes worse since the TCAs defined by the energy information had less confidence to confine the real annihilation position. The attenuation corrections were also influenced by the poor energy resolution because the trajectories calculated using equation (2-38) for each pair of photos may deviate from the actual lengths. Figure 3.10 demonstrates that the GDS-MLEM algorithm was the optimal choice for the reconstruction of activity distribution in comparison with the GS-MLEM and the LOR-MLEM reconstruction algorithms when the energy resolution was 12% and 20%. This result is important clinically, as the current clinical PET systems are equipped

with detectors having an energy resolution of approximately 20%. Additionally, some new detectors capable of achieving an energy resolution of about 12% were reported recently. Moreover, this work will be important clinically when dealing with obese patients, since there will be a greater fraction of multiple scattered coincidences and a need for increased attenuation corrections due to the larger patient size.

In conclusion, the proposed GDS-MLEM reconstruction algorithm is independent of the number of Compton scattering interactions and less sensitive to the high energy resolution. The corresponding restricted attenuation correction method manages to correct for unused scattered photons. Future work will focus on exploring the unequal probability of annihilation position distribution within the area defined by the TCAs. Specific correlations will be evaluated between the simulated phantoms and the human-shaped phantoms. A normalization algorithm will also be added to the restricted Klein-Nishina attenuation correction model, accounting for the variance of electron density among different organs.

## Appendix

The Cross-sections per unit mass of different interactions. These data were obtained from NIST XCOM: Photon Cross Sections Database.”

Photon Energy	Photoelectric Absorption	Compton. Scattering	Total Coherent
MeV	cm <sup>2</sup> /g	cm <sup>2</sup> /g	cm <sup>2</sup> /g
0.170	0.00049	0.14220	0.14270
0.175	0.00044	0.14100	0.14140
0.180	0.00040	0.13980	0.14020
0.18500	0.00037	0.13870	0.13900
0.190	0.00034	0.13750	0.13790
0.195	0.00031	0.13640	0.13670
0.200	0.00029	0.13530	0.13560
0.205	0.00027	0.13430	0.13460
0.210	0.00025	0.13330	0.13350
0.215	0.00023	0.13230	0.13250
0.220	0.00021	0.13130	0.13150
0.225	0.00020	0.13030	0.13050
0.230	0.00019	0.12940	0.12950
0.235	0.00017	0.12840	0.12860
0.240	0.00016	0.12750	0.12770
0.245	0.00015	0.12660	0.12680
0.250	0.00014	0.12580	0.12590
0.255	0.00013	0.12490	0.12510
0.260	0.00013	0.12410	0.12420
0.265	0.00012	0.12330	0.12340
0.270	0.00011	0.12250	0.12260
0.275	0.00011	0.12170	0.12180
0.280	0.00010	0.12090	0.12100
0.285	0.00010	0.12010	0.12020
0.290	0.00009	0.11940	0.11950
0.295	0.00009	0.11870	0.11870
0.300	0.00008	0.11790	0.11800
0.305	0.00008	0.11720	0.11730
0.310	0.00007	0.11650	0.11660

0.315	0.00007	0.11580	0.11590
0.320	0.00007	0.11520	0.11520
0.325	0.00006	0.11450	0.11460
0.330	0.00006	0.11390	0.11390
0.335	0.00006	0.11320	0.11330
0.340	0.00006	0.11260	0.11260
0.345	0.00005	0.11200	0.11200
0.350	0.00005	0.11140	0.11140
0.355	0.00005	0.11080	0.11080
0.360	0.00005	0.11020	0.11020
0.365	0.00005	0.10960	0.10960
0.370	0.00004	0.10900	0.10910
0.375	0.00004	0.10840	0.10850
0.380	0.00004	0.10790	0.10790
0.385	0.00004	0.10730	0.10740
0.390	0.00004	0.10680	0.10680
0.395	0.00004	0.10630	0.10630
0.400	0.00003	0.10580	0.10580
0.405	0.00003	0.10520	0.10530
0.410	0.00003	0.10470	0.10480
0.415	0.00003	0.10420	0.10430
0.420	0.00003	0.10370	0.10380
0.425	0.00003	0.10320	0.10330
0.430	0.00003	0.10280	0.10280
0.435	0.00003	0.10230	0.10230
0.440	0.00003	0.10180	0.10180
0.445	0.00003	0.10140	0.10140
0.450	0.00003	0.10090	0.10090
0.455	0.00002	0.10040	0.10050
0.460	0.00002	0.10000	0.10000
0.465	0.00002	0.09956	0.09959
0.470	0.00002	0.09913	0.09915
0.475	0.00002	0.09870	0.09872
0.480	0.00002	0.09828	0.09830
0.485	0.00002	0.09786	0.09788
0.490	0.00002	0.09744	0.09746
0.495	0.00002	0.09703	0.09705
0.500	0.00002	0.09663	0.09665
0.505	0.00002	0.09623	0.09624
0.510	0.00002	0.09583	0.09585

ANOVA analysis of equation (2-30).

ANOVA					
	Sum of Squares	df	Mean Square	F	Sig.
Regression	.171	2	.086	7410351.225	.000
Residual	.000	66	.000		
Total	.171	68			

The comparison between the calculated Compton scattering cross-sections per unit mass and the data acquired from XCOM.

Photon Energy	Compton scattering Coefficient (XCOM)	Compton scattering Coefficient (calculated)
MeV	cm <sup>2</sup> /g	cm <sup>2</sup> /g
<b>0.171</b>	0.1424	0.14231
<b>0.176</b>	0.1412	0.141055
<b>0.181</b>	0.14	0.139834
<b>0.186</b>	0.1388	0.138645
<b>0.191</b>	0.1376	0.137488
<b>0.196</b>	0.1365	0.13636
<b>0.201</b>	0.1354	0.13526
<b>0.206</b>	0.1343	0.134187
<b>0.211</b>	0.1333	0.133141
<b>0.216</b>	0.1323	0.132118
<b>0.221</b>	0.1313	0.13112
<b>0.226</b>	0.1303	0.130144
<b>0.231</b>	0.1294	0.129191

<b>0.236</b>	0.1284	0.128258
<b>0.241</b>	0.1275	0.127345
<b>0.246</b>	0.1266	0.126452
<b>0.251</b>	0.1257	0.125578
<b>0.256</b>	0.1249	0.124721
<b>0.261</b>	0.124	0.123882
<b>0.266</b>	0.1232	0.12306
<b>0.271</b>	0.1224	0.122254
<b>0.276</b>	0.1216	0.121463
<b>0.281</b>	0.1208	0.120688
<b>0.286</b>	0.1201	0.119927
<b>0.291</b>	0.1193	0.11918
<b>0.296</b>	0.1186	0.118447
<b>0.301</b>	0.1179	0.117727
<b>0.306</b>	0.1172	0.11702
<b>0.311</b>	0.1165	0.116325
<b>0.316</b>	0.1158	0.115642
<b>0.321</b>	0.1151	0.114971
<b>0.326</b>	0.1144	0.114311
<b>0.331</b>	0.1138	0.113662
<b>0.336</b>	0.1131	0.113024
<b>0.341</b>	0.1125	0.112396
<b>0.346</b>	0.1119	0.111779
<b>0.351</b>	0.1113	0.111171
<b>0.356</b>	0.1107	0.110572
<b>0.361</b>	0.1101	0.109983
<b>0.366</b>	0.1095	0.109403
<b>0.371</b>	0.1089	0.108831
<b>0.376</b>	0.1084	0.108268
<b>0.381</b>	0.1078	0.107714
<b>0.386</b>	0.1073	0.107167
<b>0.391</b>	0.1067	0.106629
<b>0.396</b>	0.1062	0.106098
<b>0.401</b>	0.1057	0.105575
<b>0.406</b>	0.1052	0.105059
<b>0.411</b>	0.1047	0.10455
<b>0.416</b>	0.1042	0.104048
<b>0.421</b>	0.1037	0.103553
<b>0.426</b>	0.1032	0.103064
<b>0.431</b>	0.1027	0.102583
<b>0.436</b>	0.1022	0.102107

<b>0.441</b>	0.1018	0.101638
<b>0.446</b>	0.1013	0.101174
<b>0.451</b>	0.1008	0.100717
<b>0.456</b>	0.1004	0.100265
<b>0.461</b>	0.09994	0.099819
<b>0.466</b>	0.0995	0.099379
<b>0.471</b>	0.09906	0.098944
<b>0.476</b>	0.09864	0.098514
<b>0.481</b>	0.09821	0.09809
<b>0.486</b>	0.09779	0.097671
<b>0.491</b>	0.09738	0.097256
<b>0.496</b>	0.09697	0.096847
<b>0.501</b>	0.09657	0.096442
<b>0.506</b>	0.09616	0.096042
<b>0.511</b>	0.09577	0.095647

## Reference

1. Gambhir S, Czernin J, Schwimmer J, Silverman DHS, Coleman RE, Phelps ME. "A Tabulated Summary of the FDG PET Literature." *J Nucl Med*;42(S1):1S-93S, 2001.
2. Wrenn, Frank R., Myron L. Good, and Philip Handler. "The Use of Positron-Emitting Radioisotopes for the Localization of Brain Tumors." *Science* 113.2940: 525-27, 1951.
3. Sweet, W H. "The Uses of Nuclear Disintegration in the Diagnosis and Treatment of Brain Tumor." *The New England Journal of Medicine* 245.23: 875-8, 1951.
4. Da G. L. Brownell and W. H. Sweet, "Localization of Brain Tumours With Positron Emitters." *Nucleonics* 11:40, 1953.
5. Plotnik, Mclaughlin, Chan, Redmayne-Titley, and Schwartz. "The Role of Nucleoside/nucleotide Transport and Metabolism in the Uptake and Retention of 3'-fluoro-3'-deoxythymidine in Human B-lymphoblast Cells." *Nuclear Medicine and Biology* 38.7: 979-86, 2011.
6. Grierson, John R, Jeffery L Schwartz, Mark Muzi, Robert Jordan, and Kenneth A Krohn. "Metabolism of 3'-deoxy-3'-F-18fluorothymidine in Proliferating A549 Cells: Validations for Positron Emission Tomography." *Nuclear Medicine and Biology* 31.7: 829-37, 2004.
7. Hudson, H. Malcolm, and Larkin, Richard S. "Accelerated Image Reconstruction Using Ordered Subsets of Projection Data." *IEEE Transactions on Medical Imaging* 13.4: 601, 1994.
8. Christian, Paul, and Waterstram-Rich, Kristen M. "Nuclear Medicine and PET/CT: Technology and Techniques." 7th ed. St. Louis, *Mo.: Elsevier/Mosby*, 2012.

9. D. L. Bailey, et al., eds., "Positron emission tomography: basic sciences." *Springer*, 2005.
10. Attix, Frank H. "Introduction to Radiological Physics and Radiation Dosimetry." *New York: Wiley-VCH*, 2004.
11. Roy, R. R., and Reed, Robert D. "Interactions of Photons and Leptons with Matter." *New York: Academic*, 1968.
12. Evans, R. D. "The Atomic Nucleus." *Physics Today* 9: 33, 1956.
13. Klein O. and Nishina Y., "Über die Streuung von Strahlung durch freie Elektronen nach der neuen relativistischen Quantendynamik von Dirac." in *Z. Phys.*, vol. 52, no. 11-12, pp. 853-869, 1929.
14. Weinberg, S., "The Quantum Theory of Fields, Volume 1." Cambridge, *UK: Cambridge University Press*, 1995.
15. H. Zaidi and M.-L. Montandon, "Scatter compensation techniques in PET." *PET Clin.*, vol. 2, pp. 219-234, 2007.
16. W. Franz, *Z. Physik* 95,652 (1935); 98, 314, 1936.
17. A. T. Nelms and L. Oppenheim, *J. Res. Natl. Bur. Std.* 55, 536, 1955.
18. J. S. Levinger, *Phys. Rev.* 87, 656, 1952.
19. Cherry, Simon R., Sorenson, James A., Phelps, Micheal E. *Physics in Nuclear Medicine*. 3 rd ed., Philadelphia: Saunders, 2003.
20. Jadvar, H., and Parker, J.A. Clinical PET and PET/CT. Dordrecht: *Springer*, 2006.
21. Zaidi, H. and Hasegawa, B., "Determination of the Attenuation Map in Emission Tomography." in *J. Nucl. Med.*, vol. 44, pp. 291-315, 2003.
22. Hooper PK, Meikle SR, Eberl S, Fulham MJ. "Validation of post injection

transmission measurements for attenuation correction in neurologic FDG PET studies.”

*J Nucl Med*, 37:128–136, 1996.

23. A. Konik, M. T. Madsen and J. J. Sunderland, “GATE simulations of human and small animal PET for determination of scatter fraction as a function of object size.” *IEEE Trans. Nucl. Sci.*, vol. 57, 2010.
24. B. Guérin and G. El Fakhri, “Novel scatter compensation of list-mode PET data using spatial and energy dependent corrections.” *IEEE Trans. Med. Imag.*, vol. 30, 2011.
25. M. E. Phelps, S. R. Cherry, and M. Dahlbom, “PET: physics, instrumentation, and scanners.” *Springer*, 2006
26. Salmon, E., Bernard Ir, C., Hustinx, R. “Pitfalls and Limitations of PET/CT in Brain Imaging.” *Seminars in Nuclear Medicine*, 45 (6), pp. 541-551, 2015
27. Miwa, K., Umeda, T., Murata, T., Wagatsuma, K., Miyaji, N., Terauchi, T., Koizumi, M., Sasaki, M. “Evaluation of scatter limitation correction: A new method of correcting photopenic artifacts caused by patient motion during whole-body PET/CT imaging.” *Nuclear Medicine Communications*, 37 (2), pp. 147-154, 2016
28. B. Bendriem, R. Trebossen, V. Frouin and A. Syrota, “A PET scatter correction using simultaneous acquisitions with low and high lower energy thresholds.” *IEEE Nuclear Science Symposium and Medical Imaging Conference, San Francisco, CA*, pp. 1779-1783, 1993.
29. H. Zaidi, M.-L. Montandon, and S. Meikle, “Strategies for attenuation compensation in neurological PET studies.” *NeuroImage*, vol. 34, pp. 518-541, 2007.
30. K. S. Kim and J. C. Ye, “Fully 3D iterative scatter-corrected OSEM for HRRT PET using a GPU.” *Phys. Med. Biol.*, vol. 56, pp. 4991-5009, 2011.

31. D. L. Bailey, "Quantitative procedures in 3D PET." *The Theory and Practice of 3D PET*, pp. 55-109, 1998.
32. H. Zaidi and K. F. Koral, "Scatter modelling and compensation in emission tomography." *European Journal of Nuclear Medicine and Molecular Imaging*, vol. 31, pp. 761-782, 2004.
33. S. Grootoonk, T. J. Spinks, D. Sashin, N. M. Spyrou and T. Jones, "Correction for scatter in 3D brain PET using a dual energy window method." *Phys. Med. Bio.*, vol. 41, pp. 2757-2774, 1996.
34. H. Zaidi, "Scatter modelling and correction strategies in fully 3-D PET." *Nucl.Med. Commun.*, vol. 22, pp. 1181-1184, 2001.
35. L.-E. Adam, J. S. Karp and R. Freifelder, "Scatter correction using a dual energy window technique for 3D PET with NaI(Tl) detectors." *IEEE Nuclear Science Symposium & Medical Imaging Conference*, pp. 2011-2018, 1998.
36. O. Barret, T. A. Carpenter, J. C. Clark, R. E. Ansorge and T. D. Fryer, "Monte Carlo simulation and scatter correction of the GE Advance PET scanner with SimSET and Geant4." *Phys. Med. Bio.*, vol. 50, pp. 4823-4840, 2005.
37. S. Basu, H. Zaidi, S. Holm and A. Alavi, "Quantitative techniques in PET-CT imaging." *Current Medical Imaging Reviews*, vol. 7, pp. 216-233, 2011.
38. D. L. Bailey and S. R. Meikle, "A convolution-subtraction scatter correction method for 3D PET." *Phys. Med. Bio.*, vol. 39, pp. 411-424, 1994.
39. F. J. Beekman, C. Kamphuis and E. C. Frey, "Scatter compensation methods in 3D iterative SPECT reconstruction: A simulation study." *Phys. Med. Biol.*, vol. 42, pp. 1619-1632, 1997.

40. M. Tamal, A. J. Reader, P. J. Markiewicz, P. J. Julyan, and D. L. Hastings, "Noise properties of four strategies for incorporation of scatter and attenuation information in PET reconstruction using the EM-ML algorithm." *IEEE Trans. Nucl. Sci.*, vol. 53, pp. 2778-2786, 2006.
41. J. Qi, R. M. Leahy, C. Hsu, T. H. Farquhar, and S. R. Cherry, "Fully 3D Bayesian image reconstruction for the ECAT EXACT HR+." *IEEE Trans. Nucl. Sci.*, vol. 45, pp. 1096 – 1103, 1998.
42. J. E. Bowsher, V. E. Johnson, T. G. Turkington, R. J. Jaszczak, C. E. Floyd, Jr., and R. Edward Coleman, "Bayesian reconstruction and use of anatomical a priori information for emission tomography." *IEEE Trans. Med. Imag.*, vol. 15, pp. 673-686, 1996.
43. H. Zaidi, "Relevance of accurate Monte Carlo modeling in nuclear medical imaging." *Med. Phys.*, vol. 26, pp. 574-608, 1999.
44. H. Sun and S. Pistorius, "Evaluation of the feasibility and quantitative accuracy of a Generalized Scatter 2D PET reconstruction method." *ISRN Biomedical Imaging*, 2013.
45. M. Conti, I. Hong, and C. Michel, "Reconstruction of scattered and unscattered PET coincidences using TOF and energy information." *Phys. Med. Biol.*, vol. 57, pp. N307-317, 2012.
46. Ting Y, Pei C, Juan G, et al. "Investigation of scatter from out of the field of view and multiple scatter in PET using Monte Carlo simulations." *Chinese Physics C*, 35(12): 1166, 2011.
47. J. M. Ollinger, "Model-based scatter correction for fully 3D PET." *Phys. Med. Biol.*,

- vol. 41, pp.153-176, 1996.
48. R. J. Jaszczak, K. L. Greer, C. E. Floyd, Jr., C. C. Harris and R. E. Coleman, "Improved SPECT quantification using compensation for scattered photons." *The Journal of Nuclear Medicine*, vol. 25, pp. 893-900, 1984.
  49. Jaszczak Phantoms, May 06, 2011; Available at [http://www.spect.com/pub/Flanged\\_Jaszczak\\_Phantoms.pdf](http://www.spect.com/pub/Flanged_Jaszczak_Phantoms.pdf)
  50. Hongyan Sun, and Pistorius. "Improvements in Image Quality When Using Patient Outline Constraints with a Generalized Scatter PET Reconstruction Algorithm." *Nuclear Science Symposium and Medical Imaging Conference (NSS/MIC)*, 2012 IEEE: 3083-089, 2012.
  51. Chien-Min Kao, Dong Yun, Qingguo Xie, and Chin-Tu Chen. "An Investigation of the Potential Benefits in Trading Energy Resolution for Timing Resolution in Time-of-Flight Positron Emission Tomography." *Nuclear Science Symposium Conference Record*, 2006 IEEE: 2564-569, 2006.
  52. Kyba, C.C.M., J. Glodo, E.V.D. Van Loef, J.S. Karp, and K.S. Shah. "Energy and Timing Response of Six Prototype Scintillators for TOF-PET." *Nuclear Science, IEEE Transactions on* 55.3: 1404-408, 2008.
  53. Krishnamoorthy, Srilalan, Benjamin Legeyt, Matthew E. Werner, Madhuri Kaul, F. M. Newcomer, Joel S. Karp, and Suleman Surti. "Design and Performance of a High Spatial Resolution, Time-of-Flight PET Detector." *Nuclear Science, IEEE Transactions on* 61.3: 1092-098, 2014.